



37th Annual VFS Student Design Competition
Leonardo's Aerial Screw:
500 Years Later

Sponsored by



UNIVERSITY OF
MARYLAND

Alfred Gessow Rotorcraft Center
Department of Aerospace Engineering
University of Maryland
College Park, MD 20742 U.S.A.



Alfred Gessow Rotorcraft Center
Department of Aerospace Engineering
University of Maryland
College Park, MD 20742 U.S.A.

James Sutherland

Graduate Student (Team Leader)
Jsuther2@umd.edu

Robert Brown

Graduate Student (NSWCCD)
rbrown36@umd.edu

Ehiremen Ebebele

Graduate Student
eebebele@umd.edu

Emily Fisler

Graduate Student
efisler@umd.edu

Katie Krohmaly

Graduate Student
katiek@umd.edu

Jehnae Linkins

Graduate Student
linkinsj@umd.edu

Koushik Marepally

Graduate Student
koushikm@umd.edu

Austin Prete

Graduate Student
aprete1@umd.edu

Ilya Semenov

Graduate Student
isemenov@umd.edu

Dr. Vengalatorre Nagaraj

Faculty Advisor
vnagaraj@umd.edu

Dr. Inderjit Chopra

Faculty Advisor
chopra@umd.edu

Dr. Anubhav Datta

Faculty Advisor
datta@umd.edu



Alfred Gessow Rotorcraft Center
Department of Aerospace Engineering
University of Maryland
College Park, MD 20742 U.S.A.

To Vertical Flight Society:

The members of the University of Maryland Graduate Student Design Team hereby grant VFS full permission to distribute the enclosed Executive Summary and Final Proposal for the 37th Annual Design Competition as they see fit.

The UMD Graduate Design Team

ACKNOWLEDGEMENTS

The design team wishes to acknowledge the following people for their invaluable discussion, guidance, and support throughout the course of this project.

University of Maryland Faculty

Dr. Inderjit Chopra – Distinguished University Professor and Alfred Gessow Professor, Director of Alfred Gessow Rotorcraft Center (AGRC), Department of Aerospace Engineering, University of Maryland, College Park

Dr. Vengalattore T. Nagaraj – Research Scientist, Department of Aerospace Engineering, University of Maryland, College Park

Dr. Anubhav Datta – Associate Professor, Department of Aerospace Engineering, University of Maryland, College Park

Dr. James Baeder – Professor, Department of Aerospace Engineering, University of Maryland, College Park

Alfred Gessow Rotorcraft Center Graduate Students

Yong Su Jung

Seyhan Gul

Cheng Chi

Frederick Tsai

Abhishek Shastry

Contents

Acknowledgements	4
List of Figures	v
List of Tables	ix
1 Introduction	1
2 Parametric Aerial Screw Testing	3
2.1 Experimental Setup	3
2.2 Rotors Tested	4
2.3 Parametric Study Results	5
2.3.1 Effect of Pitch and Radius	7
2.3.2 Effect of Lip	7
2.3.3 Effect of Number of Turns	7
2.3.4 Effect of Taper	11
2.4 Summary	11
3 Computational Aerodynamics of Aerial Screw	12
3.1 Design Variables and Test Matrix	12
3.2 Validation with the Experiments	13
3.3 The da Vinci Code: Thrusting Mechanism of Aerial Screw	14
3.4 The Geometry of <i>Elicó</i>	15
3.4.1 Performance Variation with Tip Speed	17
3.4.2 Performance Variation with Size	18
3.5 Summary	18
4 Configuration Selection	19
4.1 Voice of the Customer	19
4.1.1 Selection Criteria	19
4.1.2 Analytical Hierarchy Process	20
4.2 Potential Configurations	21
4.2.1 Vehicle Control Solutions	21

4.2.2	Anti-Torque Solutions	22
4.3	Configuration Selection	23
5	Preliminary Vehicle Sizing	24
5.1	Mission Profile	24
5.2	Design Constraints	25
5.3	Methodology	26
5.4	Trade Studies	27
5.4.1	Propulsion System	28
5.4.2	Number of Aerial Screws	28
5.5	Summary of Aircraft Specifications	29
6	Vehicle Geometry	31
7	Rotor Structural Design	34
7.1	Rotor Skin	35
7.1.1	Skin Material	35
7.1.2	Structure Interference Considerations	35
7.1.3	Skin Attachment	36
7.2	Spars	39
7.2.1	Number of Spars	39
7.2.2	Spar Loads	39
7.2.3	Spar Sizing	40
7.2.4	Spar Material	42
7.2.5	Spar Finite Element Analysis	42
7.3	Rotor Shaft	43
7.3.1	Shaft Loads	43
7.3.2	Shaft Sizing	43
7.3.3	Shaft Material	44
7.4	Vibration Absorber	44
7.5	Attachments	48
7.5.1	Spar Mounting Assembly	48
7.5.2	Support Helix	48
7.5.3	Shaft Mounting Assembly	48
7.5.4	Attachment Materials	49
7.6	Aerial Screw Fabrication	50
7.7	Rotor Weight Breakdown	51
8	Airframe Design	51
8.1	Nacelle and Drivetrain Structure	52
8.1.1	Connection to Rotor	52
8.1.2	Drivetrain Housing	53
8.1.3	Landing Legs	57
8.1.4	Nacelle Skin	58

8.1.5	Connection to Arms	59
8.2	Arms Structures Design	60
8.2.1	Truss Configuration Selection	60
8.2.1.1	Rotor support arms sizing	62
8.2.2	Finite Element Analysis (FEA) of Rotor Support Arms	64
8.2.3	Manufacturing Process	66
8.3	Central Structure	66
9	Propulsion and Transmission	66
9.1	Battery Selection	67
9.2	Electric Motor Trade Study	68
9.3	Motor Controller Selection	68
9.4	Detailed Powertrain Analysis	69
9.4.1	Battery Placement Consideration	71
9.4.2	Propulsion Power Schematic	72
9.5	Gearbox and Shaft Connections	72
9.5.1	Gear Stages	72
9.5.2	Flex Coupling and Rotor Coupling	75
10	Avionics	75
10.1	Overview	75
10.2	Nacelle Avionics	76
10.2.1	Selection of <i>Elenco's</i> Microcontrollers	77
10.3	Pilot Interface Avionics	78
10.4	Main Flight Computer	79
10.4.1	Selection of <i>Elenco's</i> Main Flight Computer	80
10.5	Computer Vision	81
11	Weight Analysis	82
12	Flight Mechanics	83
12.1	Control System Design	83
12.2	Maneuverability & Pilot Workload	84
13	Pilot Accommodations and Interface	85
13.1	Multi-Function Display	86
13.2	<i>Elenco</i> Flight Experience	87
14	Interactional Aerodynamics and Acoustics	88
14.1	Interaction Between the Rotors	88
14.2	Ground Effect	90
14.3	Acoustics	90
15	Cost	91

16 Performance and Capabilities	92
16.1 Drag Estimation	92
16.2 Effect of Center of Gravity on Rotor Speed	92
16.3 Performance at Various Altitudes	93
16.4 Autorotation	94
16.5 Performance Limits	94
16.5.1 Maximum Range	94
16.5.2 Maximum Payload in Hover	95
16.5.3 Turbo-Electric Option for Greater Range	95
16.6 Potential Applications for <i>Eluco</i>	97
17 Summary	98

List of Figures

1.1	A reproduction of Manuscript B Folio 83v	1
1.2	<i>Elico</i> in cruise over Vinci, Italy	1
2.1	Aerial screw hover stand	3
2.2	3D printed rotors used for experimental tests	4
2.3	Depiction of various aerial screw parameters	5
2.4	Effect of aerial screw pitch ratio on thrust	6
2.5	Effect of aerial screw pitch ratio on power	6
2.6	Effect of aerial screw pitch ratio on FM	6
2.7	Effect of aerial screw lip on thrust	8
2.8	Effect of aerial screw lip on torque and current	8
2.9	Effect of aerial screw lip on FM	8
2.10	Effect of aerial screw turns on thrust	9
2.11	Effect of aerial screw turns on torque and current	9
2.12	Effect of aerial screw turns on FM	9
2.13	Effect of aerial screw taper (top radius:bottom radius) on thrust	10
2.14	Effect of aerial screw taper on torque and current	10
2.15	Effect of aerial screw taper on FM	10
2.16	Power loading and disk loading of all rotor tests	12
3.1	Four views of screw for case 1 (Low Pitch)	13
3.2	Four views of screw for case 2 (High Pitch)	13
3.3	Four views of screw for case 3 (Hedral)	14
3.4	Four views of screw for case 4 (Tapered)	14
3.5	Case 1 aerial screw in hover with da Vinci vortex	14
3.6	Validation with experiments	14
3.7	Vorticity isosurfaces of the <i>Elico</i> 's rotor	16
3.8	Azimuthal variation of pressure	16
3.9	Radial variation of pressure	17
3.10	PL vs DL for various hover vehicles and <i>Elico</i> rotors	18
4.1	Relative weighting of design criterion from the AHP	20
4.2	Conceptual design concepts for vehicle control solutions.	21
4.3	Conceptual design concepts for anti-torque solutions	22

List of Figures

5.1	Mission specified by the RFP	24
5.2	Process for preliminary sizing; iteration steps are within the dotted lines	25
5.3	Gross takeoff weight, maximum rotor radius, and total hover power required vs disk loading for varying powerplant systems on an aerial screw quadcopter	28
5.4	Gross takeoff weight, maximum rotor radius, and total hover power required vs disk loading for varying number of rotors	29
5.5	Weights, maximum rotor radius, and total hover power required vs disk loading for an all-electric quadcopter design	30
6.1	Design evolution of <i>Eluco's</i> aerial screw	32
6.2	Overview of <i>Eluco</i>	33
7.1	Overview of <i>Eluco's</i> rotor structure	34
7.2	Image of the spar-skin interference	36
7.3	Embedded features in the skin	37
7.4	The leading edge wrap with labeled tension bearing locations	38
7.5	The plastic insert mounted to the structure	38
7.6	Backside view of the insert in isolation	38
7.7	Weight of all spars increases with increasing number of spars	39
7.8	Lift and drag distributions over each spar	41
7.9	The relationship of spar thickness ratio to root radius with the design point shown	41
7.10	Designed spar taper distributions	42
7.11	FEA result for a spar	43
7.12	Shaft weight and wall thickness with varying outer radius and material	44
7.13	Diagram of the forces and deflection relating to 1/rev vibration of the aerial screw	45
7.14	The vibration absorber assembly	46
7.15	FEA study for vibration absorber attachments	47
7.16	1/rev rotor moment and arm twist deflection amplitude vs RPM	47
7.17	Summary of rotor attachment components	49
7.18	Factor of safety plots of the spar mounting parts	50
7.19	FEA results on the lift collar and corresponding mounting holes on the shaft	50
8.1	Rotor, nacelle and arm connections	52
8.2	Nacelle assembly with and without cover	53
8.3	Connections holding rotor shaft	54
8.4	Gearbox shroud as positioned and connected in nacelle structure	54
8.5	Nacelle structure as a single welded part	55
8.6	Access to inner components of nacelle structure	56
8.7	Array of landing leg attachments to nacelle structure	56
8.8	Individual landing leg attached to nacelle structure	57
8.9	Connection point of nacelle shroud to nacelle structure and access cutout for assembly and airflow management	58
8.10	Connection to arms	58
8.11	Arm to nacelle attachment	59

8.12	Finite element analysis of titanium pins	60
8.13	Components of the cellular truss	61
8.14	8-node double grid truss cross-section	61
8.15	The triangular cellular-truss cross-section	62
8.16	A cellular truss bay	63
8.17	Fully assembled tri-cellular truss	63
8.18	Axial stress distribution on arms from rotor thrust	65
8.19	Arms to central structure attachment	66
9.1	Commercial battery types and their power densities	67
9.2	MaxAmps reference battery specification	67
9.3	Efficiency plots for the EMRAX 188 and 208 brushless DC motors	69
9.4	<i>Elicó's</i> final power train components	71
9.5	Battery placement options	71
9.6	<i>Elicó's</i> power schematic (only one nacelle shown for clarity)	72
9.7	Gearbox with planetary gear reduction stages	73
9.8	Flex coupling used to correct potential misalignments in shaft and rotor coupling used to connect flex coupling to rotor shaft	75
10.1	<i>Elicó's</i> avionics development areas and hub and spoke overview	76
10.2	Nacelle module placement and connection scheme	77
10.3	Texas Instruments Hercules and list of specifications	78
10.4	Pilot interface module placement and connection scheme	79
10.5	Main flight computer module placement and connection scheme	80
10.6	NVIDIA AGX Xavier and list of specifications	81
10.7	Example of an AprilTag	81
11.1	<i>Elicó's</i> empty weight and payload z_{CG} locations	83
12.1	Rotation directions of <i>Elicó's</i> motors	83
12.2	Control system block diagram	84
12.3	Mission specified by the RFP, with flight path (A \rightarrow B \rightarrow C \rightarrow D)	84
12.4	Path of <i>Elicó</i>	85
12.5	X and Z Position of <i>Elicó</i> vs time elapsed	85
13.1	Pilot cockpit arrangement	86
13.2	Multi-function tablet display for initial start up	87
13.3	Multi-function tablet display for in flight vehicle information	87
13.4	Pilot and <i>Elicó</i>	88
14.1	CFD model for investigating the interaction between the rotors of <i>Elicó</i>	89
14.2	Streamlines of the flow around the rotors	89
14.3	Sound pressure level split up at $6R$ from the vehicle	90
16.1	Effect of forward CG shift on front and back rotor speeds and power outputs	93

List of Figures

16.2	Effect of backwards CG shift on front and back rotor speeds and power outputs	93
16.3	Rate of climb at various pressure altitudes	94
16.4	Effect of decreasing payload and increasing battery weight on maximum range	95
16.5	Honeywell's HTS900 turbogenerator	96
16.6	<i>Eligo</i> landed in the gardens at the <i>Museo Nazionale Scienza e Tecnologia Leonardo da Vinci</i> in Milan, Italy	98

List of Tables

1.1	Overview of <i>Elicó's</i> Key Features	2
2.1	Test Matrix	5
3.1	Specifications of four different aerial screw geometries analyzed with CFD	13
3.2	Performance estimates of the aerial screws	15
3.3	Performance of <i>Elicó's</i> rotor at different tip speeds	18
3.4	Performance of <i>Elicó's</i> rotors of different sizes	18
4.1	AHP Weights	20
4.2	Pugh Decision Matrix: Vehicle Control	23
4.3	Pugh Decision Matrix: Rotor Configuration	24
5.1	Summary of aircraft specifications	30
6.1	Aerial screw detailed dimensions	32
7.1	Validation of calculated with CFD aerodynamic loads (10 ft radius case)	40
7.2	1/rev Loads at the Base of the Shaft in the Rotating Frame	43
7.3	Weight breakdown of a rotor	51
8.1	Carbon Fiber-Epoxy Material properties	62
8.2	Tri-cellular truss properties	64
8.3	FEA Results	65
8.4	Arms weight breakdown	65
9.1	Market review of available electric motors	68
9.2	EMRAX motor controller trade study	69
9.3	Effect of battery voltage on powertrain mass. The total mass m_{tot} is the sum of the battery, motor, and motor controller masses for the entire vehicle	70
9.4	Gear Geometry and Information	75
10.1	Modules used to monitor the nacelle's performance.	77
10.2	Pilot interface modules.	79
10.3	Modules for the main flight computer	80
11.1	Weight breakdown and CG analysis for components of <i>Elicó</i>	82

List of Tables

14.1	Performance estimates of the aerial screw with interactional aerodynamic models	90
15.1	Cost breakdown for <i>Elicó</i>	91
16.1	Power required for <i>Elicó</i> to hover out of ground effect in College Park, MD and in Denver, CO	93
16.2	Honeywell HTS900 turbogenerator specifications	96

***Elico* RFP Requirements and Compliance**

RFP Requirement	Solution	Chapter
The vehicle shall rely on one or more aerial screws for lift and thrust.	<i>Elico</i> utilizes 4 rotors for lift, thrust, and control	5, 3
The rotor must use a single blade with solidity equal or greater than one with a continuous surface.	The single blade on the rotor sweeps a continuous surface through one revolution.	2, 3, 8
The vehicle must carry a pilot or passenger of at least 60 kg.	<i>Elico</i> is designed to lift a 60 kg human load. Additional payload can be traded off for reduced endurance.	5, 16
The vehicle must take-off and land vertically, holding position for 5 seconds without drifting.	The avionics and flight controls installed on <i>Elico</i> allow for stable flight throughout the required mission.	10, 12
The vehicle must fly forward for at least one minute, covering at least 20 m of distance.	<i>Elico</i> is equipped with batteries that enable hover for up to 3 minutes.	5, 9
The vehicle must operate at least 1 m above the ground.	All rotor analysis is performed out of ground-effect, assuming no extra benefit from ground proximity.	3

Documentation Requirements and Compliance

Documentation Requirement	Chapter
Configuration Trade-Off Analysis	4
Selected Concept Sizing and Description	5
Overall Geometry and Aesthetics	6
Aerodynamics	2, 3
Structures and Materials	8
Power and Energy	9
Rotor	2, 3, 8
Controls and Piloting	12
Concept Validation	2, 3
Capability, Performance, and Requirement Compliance	16
Additional Graduate Team Sections:	
Weights Assessment	11
Rotor and Airframe Loads	8
Structural Analysis	8
Maneuverability and Workload	12
Control System Concept	12
Accommodation, Accessibility, and Human Factors	13
Demonstrator Manufacturing and Feasibility	8

In order to avoid duplication of written sections, the specified report structure has been slightly modified.

1 Introduction

Leonardo da Vinci (1452-1519) was the epitome of a “Renaissance Man”. Over the course of his life and travels, Leonardo made a major impact in the realms of painting, sculpting, drawing, anatomy, architecture, mathematics, and engineering. The range of his abilities and interests is best observed in his detailed notes, which give insight into his genius mind [1] [2]. In 1489, on Manuscript B Folio 83v, Leonardo sketched what is commonly considered the first concept of a manned flying vehicle, a precursor to the modern day helicopter [3]. The sketch, reproduced in Figure 1.1, is commonly referred to as an “aerial screw” and shows a cloth screw mounted above a platform. The shaft has poles protruding from the sides suggesting the vehicle be powered by four men rotating the screw. In addition to the drawing, Leonardo comments, “if this instrument made with a screw be well made – that is to say, made of linen of which the pores are stopped up with starch and be turned swiftly, [it] will make its spiral in the air and it will rise high” [4]. There is an additional note to the size of the rotor radius an astounding 8 *braccia* (18.3 ft, 5.6 m). Leonardo da Vinci knew a greater surface area would be required for an Archimedes water-screw to be flown in air. The concept was centuries ahead of its time and beyond the limits of contemporary technological capabilities.

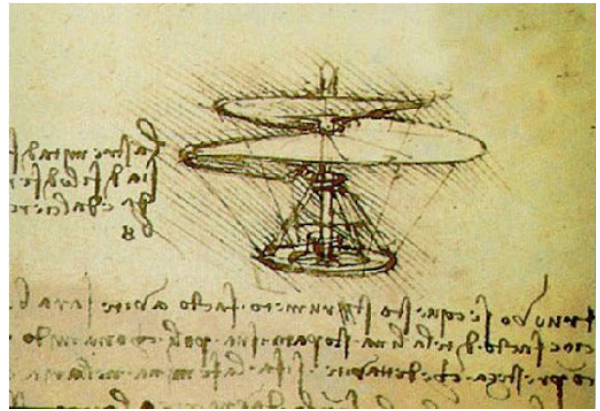


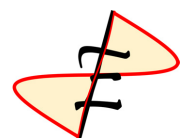
FIGURE 1.1: A reproduction of Manuscript B Folio 83v

The helicopter began as a children’s toy in China; Leonardo da Vinci was the first to document the idea of manned vertical flight. It took another 300 years for the first small-scale flying models to be developed by engineers such as Sir George Cayley, thanks to more precise fabrication techniques. Still, however, the helicopter was limited by the power available to the machine. A manned vehicle only became possible after the development of the internal combustion engine. Moving into the 20th century, as lighter materials became available and a better understanding of rotor dynamics developed, helicopter technology matured into the modern machines we know today [5]. As the scientific community further understood vertical flight, Leonardo’s aerial screw concept was cast aside for individual, high aspect-ratio, low solidity blades. But, in this modern age, the question still remains: can a manned vehicle be flown using an aerial screw?



FIGURE 1.2: *Elico* in cruise over Vinci, Italy

In response to this question and to the *2020 VFS Student Design Competition* Request for Proposal (RFP) sponsored by *Leonardo Helicopters*, the University of Maryland Graduate Student Design Team proudly presents *Elico*, as proof that, with modern technology, the ideas of Leonardo da Vinci can be built to fly. *Elico* is a quadrotor vehicle designed to demonstrate the abilities of an aerial screw for vertical flight. The name *Elico* is derived from the Italian translation of “helicoid,” the geometrical shape of the aerial screw. *Elico* is the etymological root – the foundation – of helicopter, propeller, and screw in the Italian language. The design of *Elico* brings a piece of history to life and, through autonomous flight, a paradigm shift towards the

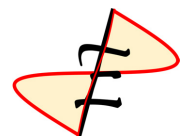


development of a revolutionary aerial vehicle.

The design first started with careful studies of the aerial screw using experimental tests of scale models and high-fidelity computational fluid dynamics (CFD) simulations – developed inhouse at the University of Maryland. Without a fundamental understanding of the operation of an aerial screw rotor, the design task would not have been possible. The design philosophy focused on optimizing the aerial screw for aerodynamic and structural efficiency while minimizing changes to the original aerial screw. The quadrotor configuration allows for simplified flight control without additional, unproven technologies. Informed by experimental and computational results, a physical understanding of the aerial screw lift mechanism was developed. The all-electric design provides efficient power to the rotors at the end of each arm with low noise. The structurally efficient support arms, nacelle, and rotors are each modular in design to allow for systematic upgrades to the vehicle as the concept matures. This report outlines the methodology utilized in arriving at the final *Elicor* design and highlights the features of the vehicle that make it a transformative technological development. An overview of these features is given in Table 1.1

TABLE 1.1: Overview of *Elicor*'s Key Features

Features	Summary
Tapered Aerial Screw Rotor	The rotor is developed from a physical understanding of the unique geometry. The tapered surface provides efficient lift through an attached vortex. The large 1/rev aerodynamic moments are completely balanced in the structure.
Quadrotor Configuration	Four independent rotors allow for precise control of the vehicle to perform any simple maneuver.
Modular Components	The rotor support arms, nacelle, and rotors can each be independently removed for repairs or replacement. As an experimental vehicle, <i>Elicor</i> is designed to adapt to new missions, systematic upgrades and component modifications.
Electric Drive	The lithium ion batteries and electric motors provide safe and efficient power to the rotor and allow for rapid RPM control.
Assured Autonomy	Designed for both piloted and autonomous capability, <i>Elicor</i> enables anyone to fly in an aerial screw vehicle.
Ultralight Structure	The rotor support arms utilize a cellular truss structure to minimize weight without sacrificing structural integrity.
High-Visibility Cockpit	Seated below the structure and large rotors, the pilot has an expanded range of vision, limited only by the nacelle fairings.



2 Parametric Aerial Screw Testing

Despite being a 500 year old concept, there has been a scarcity of aerial screw data and analysis; therefore, an early focus of this design was an in-depth study of its operation. Due to the novel working principle of Leonardo da Vinci's aerial screw, conventional rotor analysis tools such as momentum theory, blade element momentum theory, and flap-lag-pitch dynamics could not be used directly. Parameters that can be used to characterize an aerial screw such as pitch, diameter, taper, or turns are not applicable to rotor characterization and no literature exists on the effect these parameters have on aerial screw performance. Furthermore, even fundamental analysis concepts such as airfoils are not applicable.

This forced the development of new analysis tools and the use of computational fluid dynamics (CFD) to predict the performance of full size aerial screws. 417 experimental performance data points were collected in order to validate the accuracy of these novel tools. These data were acquired for small scale aerial screws in hover conditions on a custom test stand at the University of Maryland.

The central rotor shaft is directly attached to an electric brushless direct current (BLDC) motor at the bottom and passes through a roller bearing at the top. The motor to shaft mounting part is a machined tight tolerance aluminum piece designed for accurate shaft to rotation axis alignment. The top roller bearing is integrated into the cage structure to support against vibratory loads. A 6 degree of freedom load cell (ATI Mini45) reads the axial and torsional forces, a Hall effect sensor collects RPM, and additional sensors collect current and voltage. This data is collected by a data acquisition system (DAQ) and imported into LabVIEW.

2.1 Experimental Setup

The aerial screw hover stand consists of a cage structure and shaft mounted rotors as seen in Figure 2.1. It was designed to collect data and provide structural support to the aerial screws due to the presence of large vibratory loads.

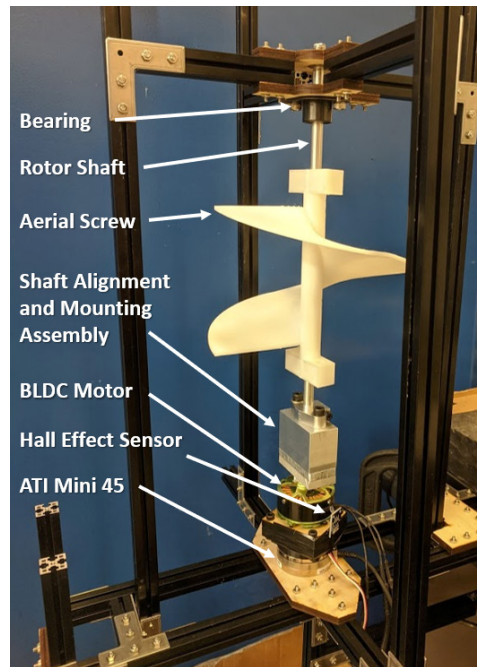


FIGURE 2.1: Aerial screw hover stand

A significant challenge of aerial screw testing was the strong vibrations exerted because of unbalanced aerodynamic and centrifugal forces. These vibrations added significant noise to the data and obscured precise measurements throughout these studies. It is conjectured this vibration might be the reason why aerial screws have not been widely pursued in large scales. Canceling these vibrations was a key task in rotor structural design and is discussed in Section 7.4.

2.2 Rotors Tested

The motivation for experimental testing was to prove the feasibility of using an aerial screw and to determine the effect of various relevant parameters depicted in Figure 2.3 and described below:

- Radius: The maximum radius viewed from above.
- Pitch: The height of the airscrew per turn.
- Number of Turns: Number of revolutions of the helicoid surface.
- Taper: The ratio of the top radius to the bottom radius.
- Lip: A small winglet like surface oriented down from the rotor tip.
- Anhedral Angle: The angle of the radial direction of the aerial screw surface with respect to horizontal.



FIGURE 2.2: 3D printed rotors used for experimental tests

As shown in Figure 2.2, rotors with various properties were all 3D printed using Makerbot printers out of polylactide (PLA) with a blade thickness of 2 mm and a shaft radius of 8 mm. These properties are listed in Table 2.1 with notable differences emphasized. It should be noted that due to structural issues no aerial screws with anhedral were tested, however this parameter is investigated computationally in Chapter 3.

TABLE 2.1: Test Matrix

Rotor	pitch/radius	taper	lip	turns
1	0.656	1:1	no	1
2	0.492	1:1	no	1
3	1.312	1:1	no	1
4	1.312	1:1	up	1
5	1.312	1:1	down	1
6	0.656	1:1	no	2
7	0.656	2:1	no	1
8	0.656	1:2	no	1
9	0.656	2:1	no	2
10	0.656	1:2	no	2

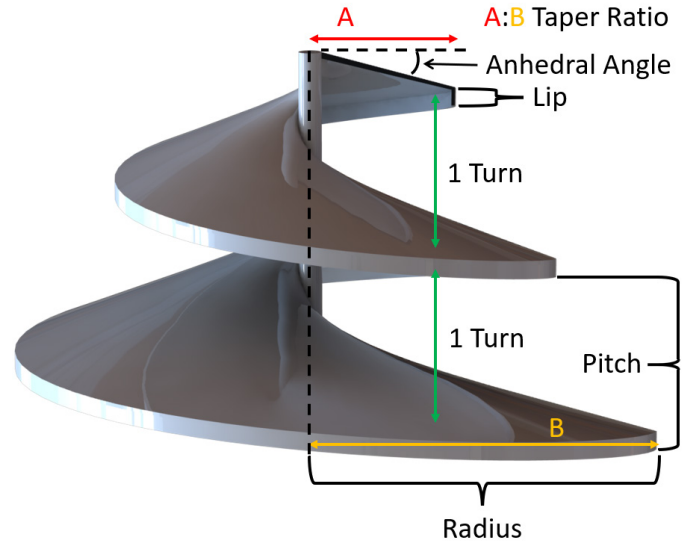


FIGURE 2.3: Depiction of various aerial screw parameters

2.3 Parametric Study Results

Some results in this section are non-dimensionalized, the definitions and abbreviations are listed:

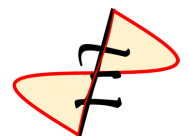
- Coefficient of thrust (C_T): $\frac{T}{\rho A (\Omega R_{max})^2}$
- Coefficient of power (C_P): $\frac{P}{\rho A (\Omega R_{max})^3}$
- Figure of Merit (FM): $\frac{C_T^{3/2}}{\sqrt{2} C_P}$
- Disc Loading (DL): $\frac{T}{A}$

Where T is thrust in Newtons, P is power in Watts, ρ is the air density in kg/m^3 , R_{max} is the maximum radius in meters, A is the disc area using the maximum radius, and Ω is the rotational speed in rad/s.

The FM is a measure of efficiency based on conventional helicopter rotors. This is used along with disc loading to compare efficiency and performance of aerial screws to conventional rotors.

Electrical power is defined as $P = IV$ and mechanical power is $P = \Omega Q$ where I is current, V is voltage, and Q is torque. Due to the vibration induced noise in torque measurements both electrical and mechanical power are analyzed in this section. The electrical power is an upper limit of the mechanical power of the rotor due to efficiency loss across the electronic speed controller (ESC) and motor. This efficiency varies with RPM and level of vibration.

A baseline result was recorded with no rotor mounted on the shaft. This is plotted in dimensional results to demonstrate the level of noise and make clear when data points are significant.



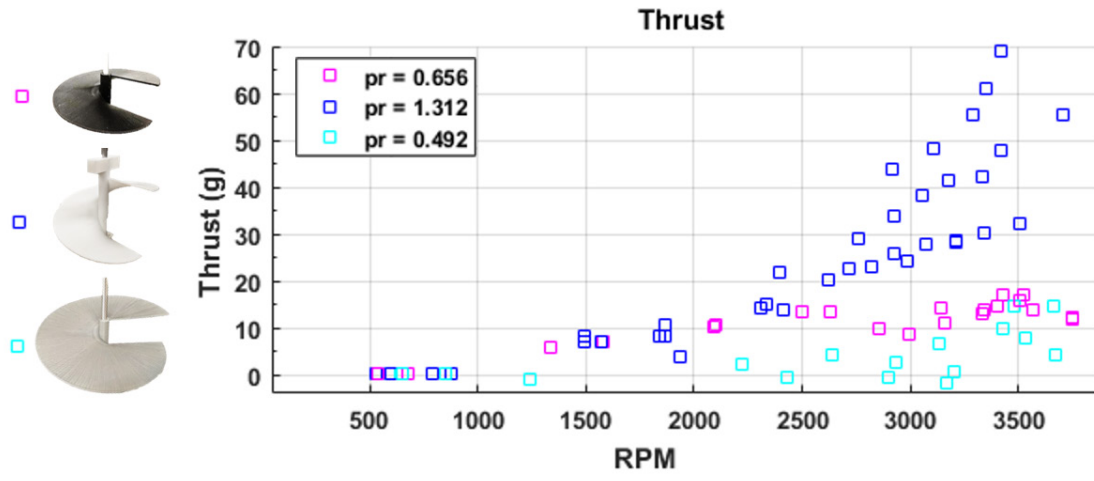


FIGURE 2.4: Effect of aerial screw pitch ratio on thrust

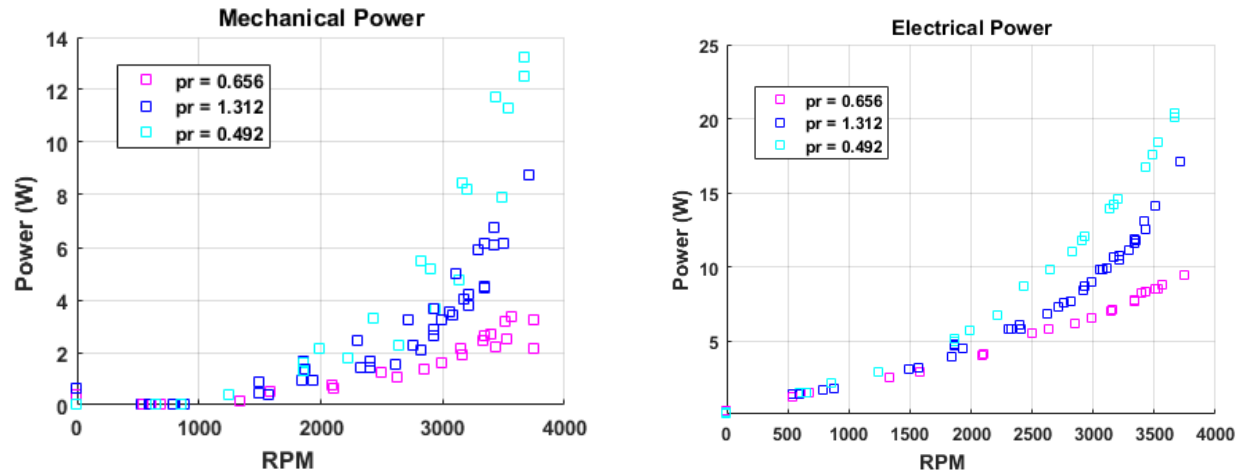


FIGURE 2.5: Effect of aerial screw pitch ratio on power

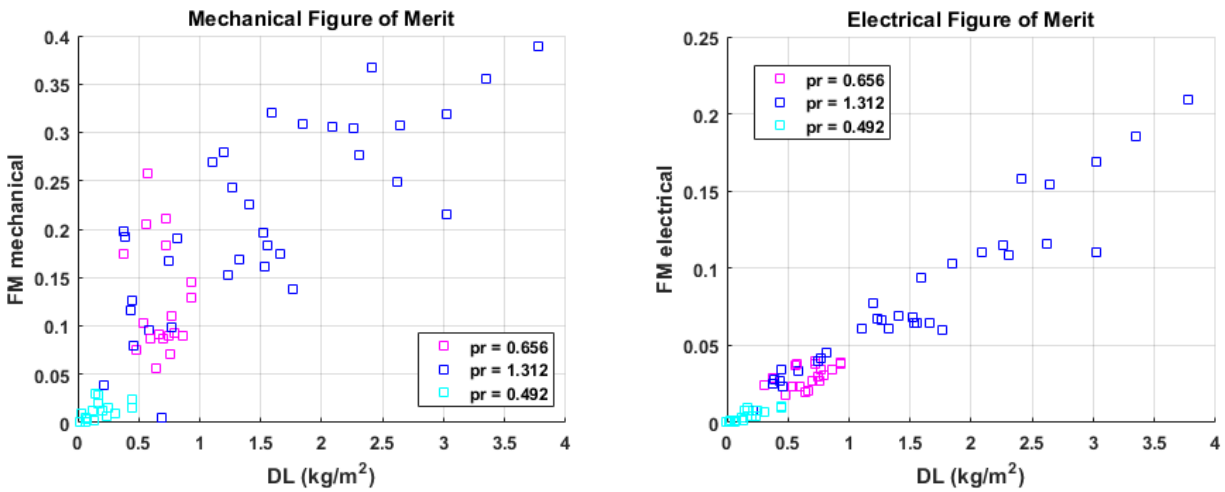
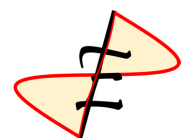


FIGURE 2.6: Effect of aerial screw pitch ratio on FM



2.3.1 Effect of Pitch and Radius

The effects of fundamental properties pitch and radius were investigated first by studying various pitch to radius ratios $pr = p/R_{max}$ where p is the pitch. The rotors (1,2 and 3 in Figure 2.2) tested have 1 turn, a 1:1 taper ratio, and no lip. Rotor 1 has a pitch of 50 mm (3.94 in) and a radius of 76 mm (3 in) resulting in a pr of 0.656, rotor 2 has the same pitch but a radius of 102 mm (4 in) resulting in a pr of 0.492. Rotor 3 has a pitch of 100 mm (3.94 in) and a radius of 76 mm (3 in) resulting in a pr of 1.312.

These results show that an aerial screw can produce significant thrust and has sufficient efficiency to enable use in a full scale vehicle. Increasing the pitch to radius ratio results in increased thrust and a higher figure of merit (Figures 2.4 and 2.6) indicating that a larger pitch to radius ratio should be used in the design. As mentioned earlier, the electrical FM is the lower limit and is conservatively considered to be the real value.

This result informed the CFD studies and provided data to validate against. It is important to note that increasing the pitch ratio does not always decrease the dimensional power requirement of the rotor as seen in Figure 2.5, showing that there is an upper limit to the efficiency gained from increasing the pitch to radius ratio.

2.3.2 Effect of Lip

The effect of a lip was investigated next. It was hypothesized that a down facing lip would prevent air from escaping radially outward from the rotor, but this was proven incorrect. All rotors tested (3,4 and 5 in Figure 2.2) have 1 turn, a pitch of 100 mm (3.94 in), a radius of 76 mm (3 in), and a 1:1 taper ratio.

A downward facing lip showed reduced thrust and an upward facing lip showed negligible impact on thrust in Figure 2.7.

Flow visualization conducted during this trial revealed that air was being ingested radially inward during operation of the no lip and up facing lip aerial screws, and that this flow was disrupted by the down facing lip. These results support the findings of the CFD studies detailed in Chapter 3.

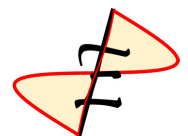
Figure 2.8 indicates that the presence of a lip in either direction increased the power requirement of the rotor. Figure 2.9 shows that the presence of a lip in either direction also reduced the FM of the aerial screw. Therefore, a lip is not a useful design feature at all, and was discarded.

2.3.3 Effect of Number of Turns

The effect of increasing the number of turns was investigated next, a parameter well out of scope of traditional rotor analysis. Novel findings on the effect of turns on aerial screw performance are shown in this Section and later in Section 2.3.4. Both rotors tested (1 and 6 in Figure 2.2) have a pitch of 50 mm (3.94 in), a radius of 76 mm (3 in), a 1:1 taper ratio, and no lip.

As shown in Figure 2.10, increasing the number of turns causes a decrease in thrust. Figure 2.11 shows that increasing the number of turns increased the power and Figure 2.12 shows that increasing the number of turns decreased the FM.

These results demonstrate that increasing the number of turns is not beneficial to the performance of an non-tapered aerial screw, however the effect of the number of turns on a tapered aerial screw is investigated in section 2.3.4 where the results support a contradictory conclusion. Therefore, the effect of the number of turns on aerial screw performance is dependent on the taper.



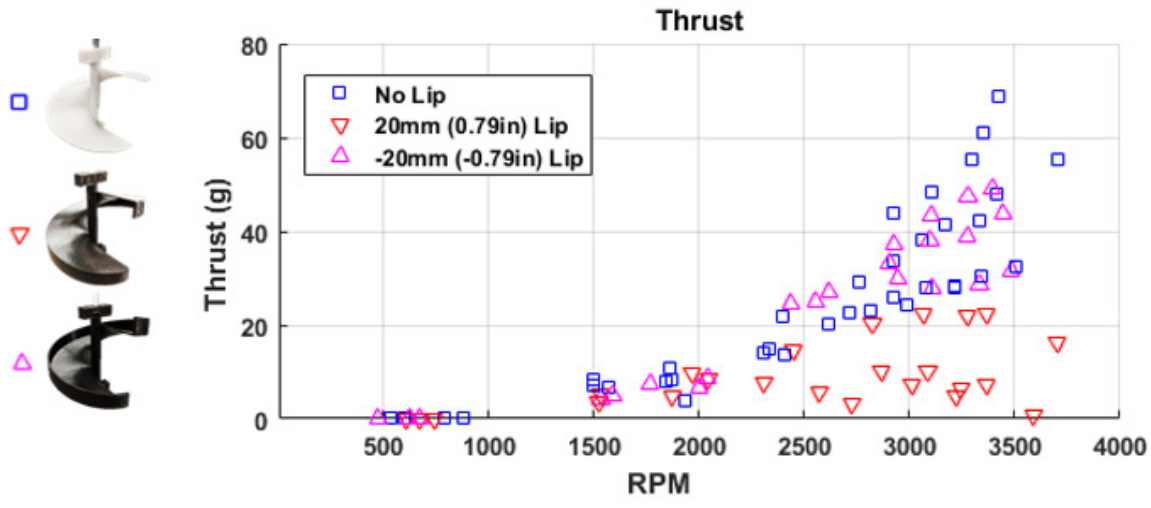


FIGURE 2.7: Effect of aerial screw lip on thrust

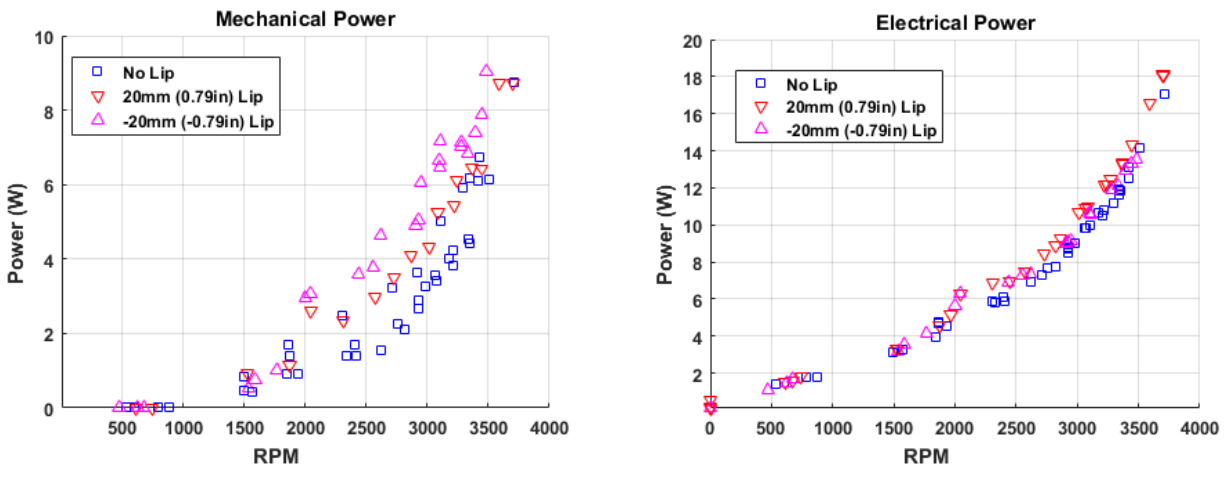


FIGURE 2.8: Effect of aerial screw lip on torque and current

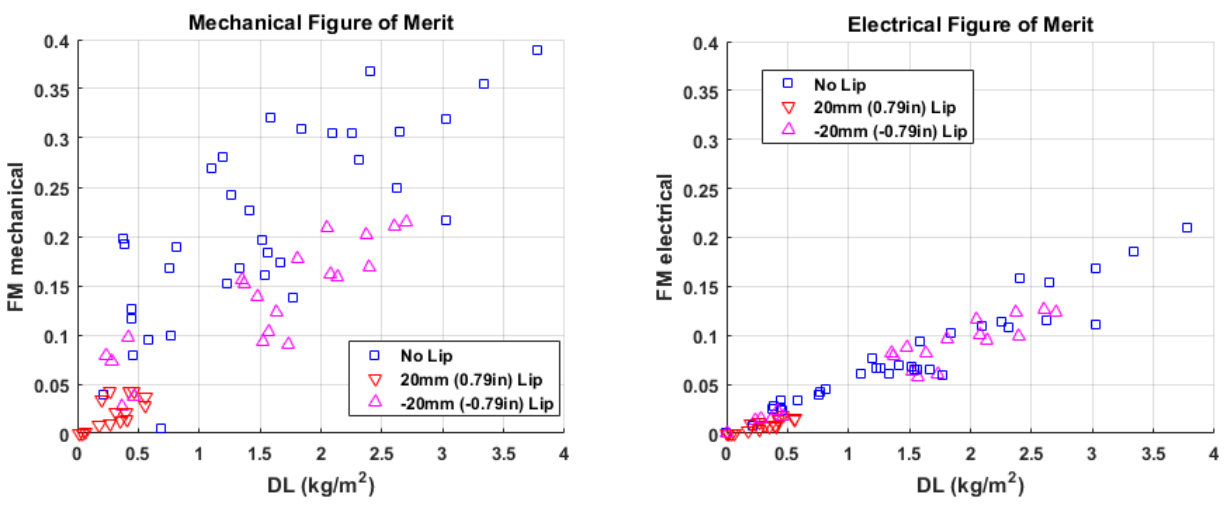
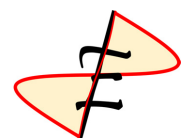


FIGURE 2.9: Effect of aerial screw lip on FM



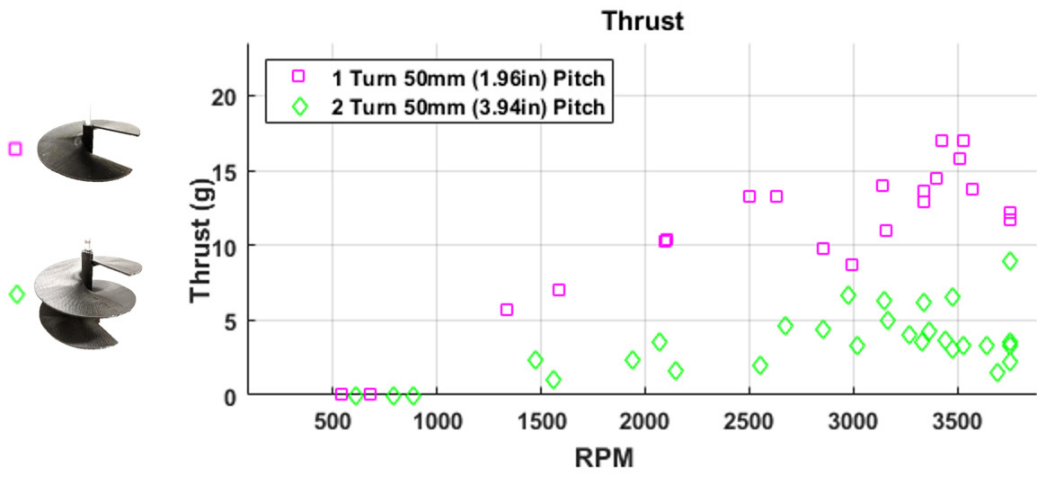


FIGURE 2.10: Effect of aerial screw turns on thrust

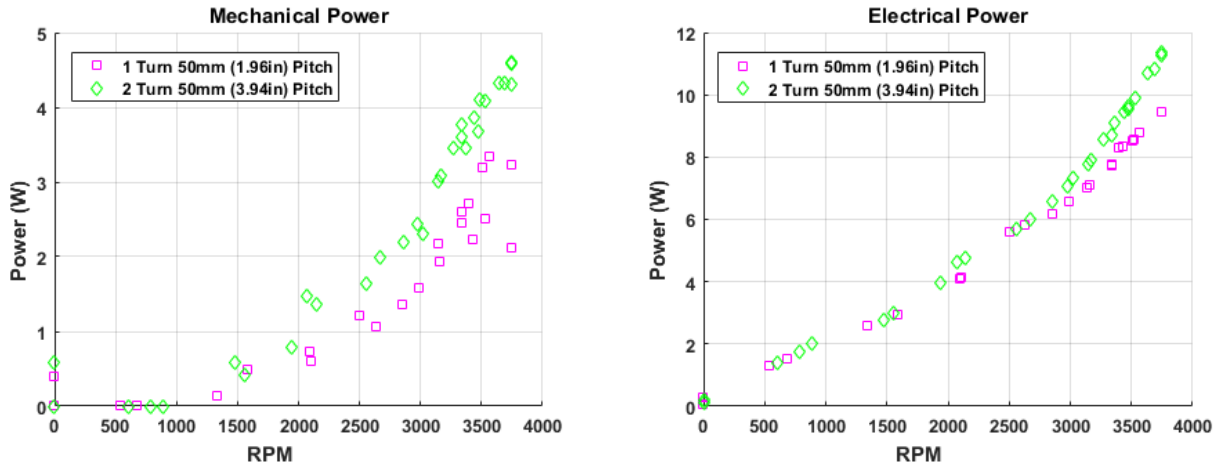


FIGURE 2.11: Effect of aerial screw turns on torque and current

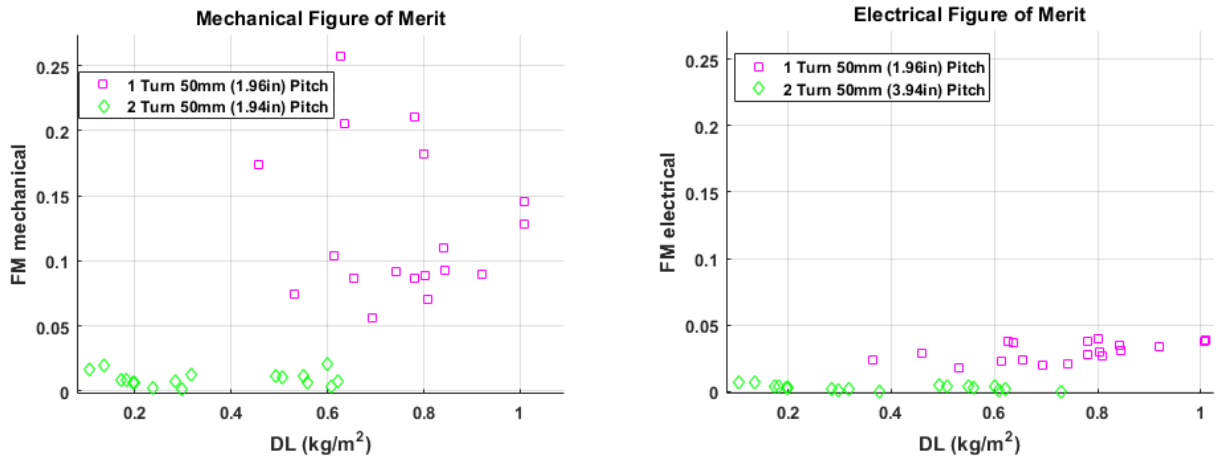
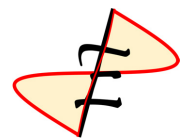


FIGURE 2.12: Effect of aerial screw turns on FM



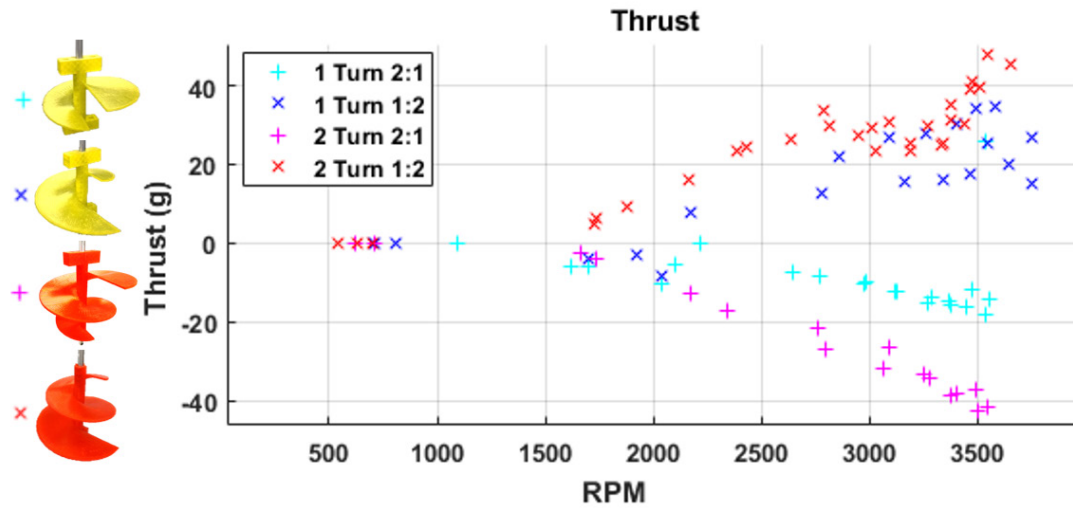


FIGURE 2.13: Effect of aerial screw taper (top radius:bottom radius) on thrust

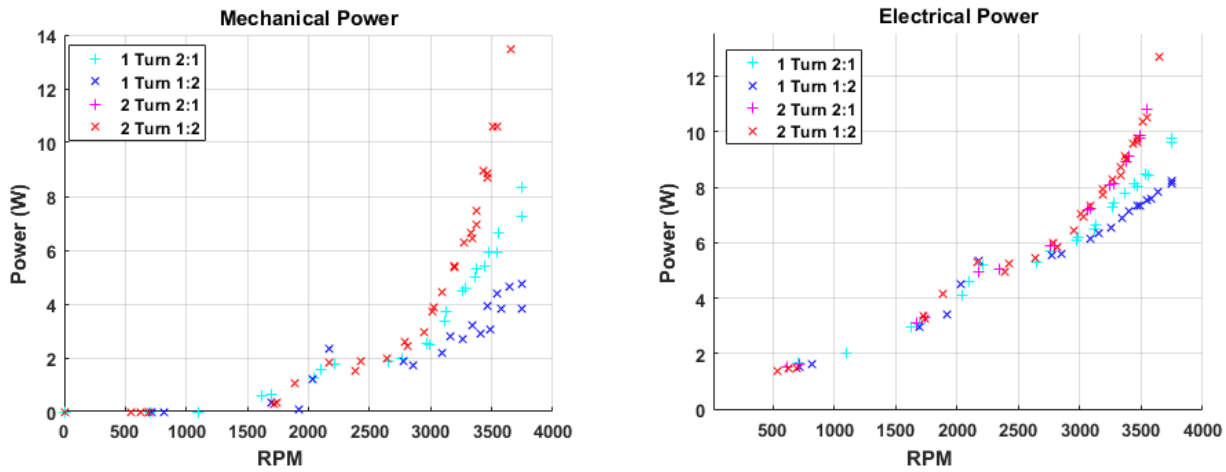


FIGURE 2.14: Effect of aerial screw taper on torque and current

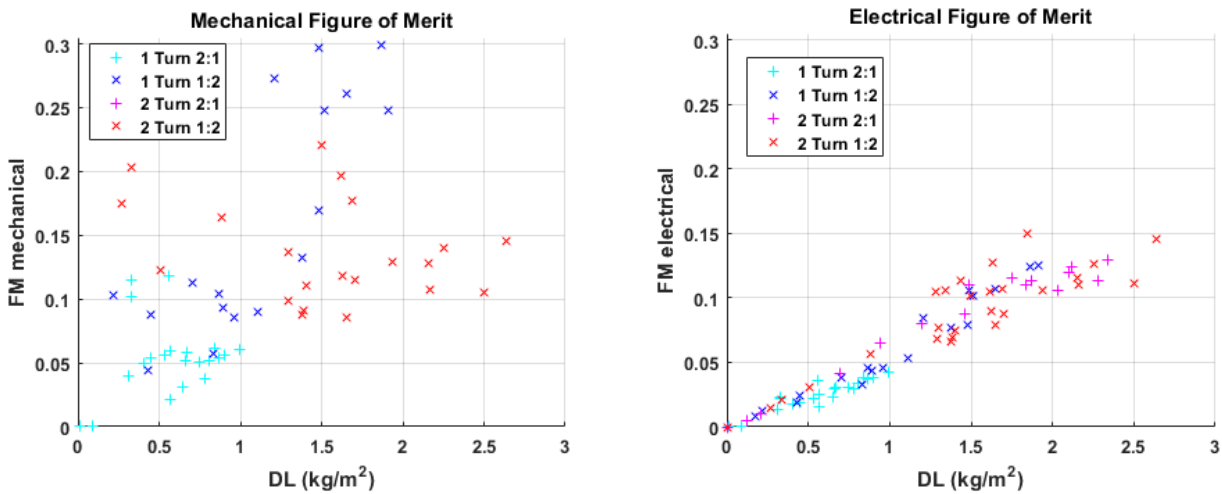
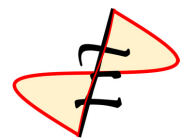


FIGURE 2.15: Effect of aerial screw taper on FM



2.3.4 Effect of Taper

Finally, the effect of varying the taper of the aerial screw was investigated. Taper is defined as the ratio of the top radius to the bottom. It was found that taper can drastically impact the performance of an aerial screw. All rotors tested (7,8,9 and 10 in Figure 2.2) have a pitch of 50 mm (3.94 in), a radius of 76 mm (3 in), and no lip.

The results in Figure 2.13 indicate that a 1:2 taper increased the thrust over a non-tapered rotor (rotor 1 in Figure 2.2, thrust plotted in Figure 2.10). Additionally the 2:1 taper case displayed a magnitude of the thrust that is comparable to the non-tapered aerial screw, but in the opposite direction.

Furthermore, in Section 2.3.3 increasing the number of turns decreased the thrust, however with 1:2 or 2:1 taper the 2 turn aerial screws showed a larger magnitude of thrust than the 1 turn tapered aerial screws; shown in Figure 2.13.

The thrust reversal of the 2:1 tapered cases was a novel and unexpected result, indicating an atypical mechanism of lift for an aerial screw.

Figure 2.14 indicates that the two turn tapered rotors have a larger power requirement than single turn tapered rotors. This is consistent with the impact of number of turns on power in a 1:1 taper case shown in Section 2.3.3, Figure 2.11. It should be noted that there is an inconsistency in the torque measurements for the two turn 2:1 tapered rotor. Based on the current readings, its torque is similar to the two turn 1:2 taper case and larger than both single turn cases.

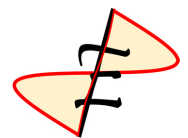
Finally, Figure 2.14 indicates that a single turn 2:1 taper aerial screw requires more power than a single turn 1:2 taper aerial screw.

To summarize, a 1:2 taper increases the thrust and FM over a non-tapered case and increasing the number of turns with taper present further increases the thrust. For these reasons a tapered case was investigated using CFD. The benefits in performance and the aesthetic similarity to Leonardo Da Vinci's original drawing made taper a key design feature of the aerial screw.

2.4 Summary

Figure 2.16 shows a comparison of each of the 417 data points collected during experimental testing which revealed key trends and informed the priorities of CFD studies. Because no substantial prior work has been reported on aerial screw rotors, all of these results are novel. The conclusions are as follows:

- Increasing radius does not guarantee more thrust, the performance is more dependent on the pitch:radius ratio (Section 2.3.1).
- An aerial screw rotor can produce useful thrust but has a high power requirement and large vibrations relative to conventional rotors (Sections 2.3.1 and 2.3.4).
- Adding a tip lip does not increase the performance (Section 2.3.2).
- Increasing the number of turns can be either detrimental or beneficial depending on the taper of the aerial screw (Sections 2.3.3 and 2.3.4).
- Adding taper has drastic effects on the performance of the aerial screw, for positive thrust a smaller top radius is beneficial (Section 2.3.4).



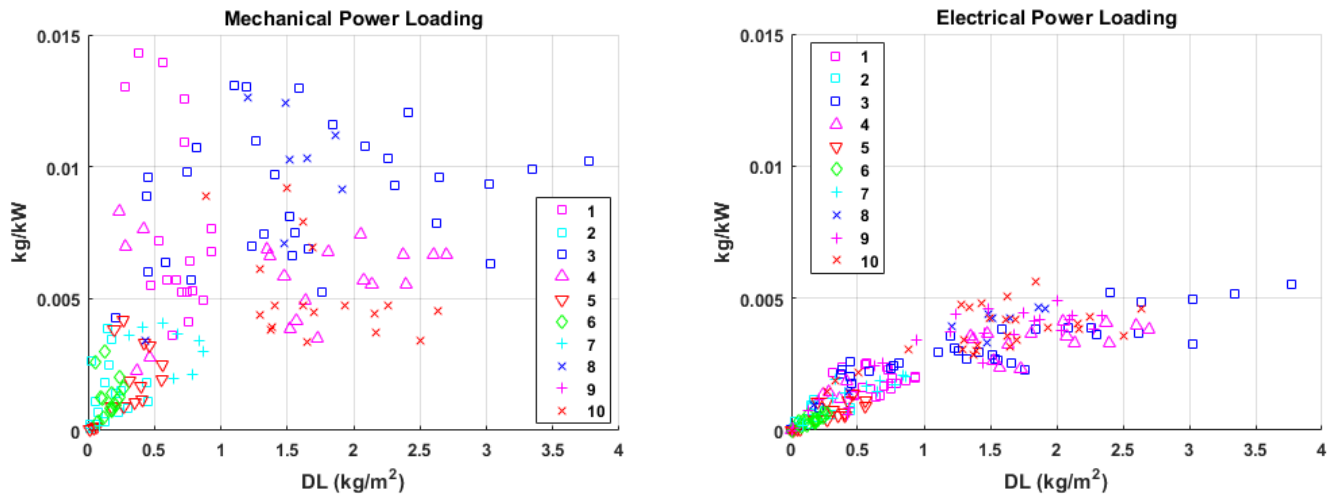


FIGURE 2.16: Power loading and disk loading of all rotor tests

This experimental study proves the existence of lift and feasibility of using a single bladed aerial screw as the lifting and propulsion component of a vehicle. Historically this lift has been missed due to the structural vibrations associated with the single blade aerial screw. Much like flapping wing concepts, the structural design is critical to stabilizing the aerial screw and harnessing the lift.

Additionally, this study demonstrates the impact of some key parameters on aerial screw performance and concludes that a pitch to radius ratio of 1.30 and a taper ratio 1:2 are rotor design targets that increase performance considerably.

Furthermore, it is expected to achieve a FM at full scale equal to or larger than the values shown at this model scale due to the larger Reynold's number, as long as the structure can be stabilized against the vibrations.

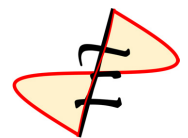
While the presence of lift is proven experimentally, its mechanism is not determined. This mechanism is investigated in Chapter 3.

3 Computational Aerodynamics of Aerial Screw

To arrive at a fundamental understanding of the aerodynamic mechanisms and scaling of the aerial screw, Computational Fluid Dynamics (CFD) was used to test various aerial screw geometries. The test matrix was developed based on the experimental testing results for various aerial screw designs. The University of Maryland's in-house CFD solver HAMSTR [6] was modified to accommodate the geometry of the rotor and arrive at the flow field surrounding it. The solver uses Hamiltonian paths and Strand grids solution methodology on overset grids, and is validated extensively on a variety of model-scale to full-scale rotors and aircraft such as the UH-60A, MD-900/SMART and X2TD.

3.1 Design Variables and Test Matrix

The effects of pitch, taper and annhedral angle on the aerodynamic behavior screw were examined by simulating four different aerial screw geometries. Figure 2.3 shows how each of these variables define an aerial screw geometry. The variation of these design parameters for the tested geometries can be found in Table 3.1 as well as the resulting surface area for each geometry. While the radius remains the



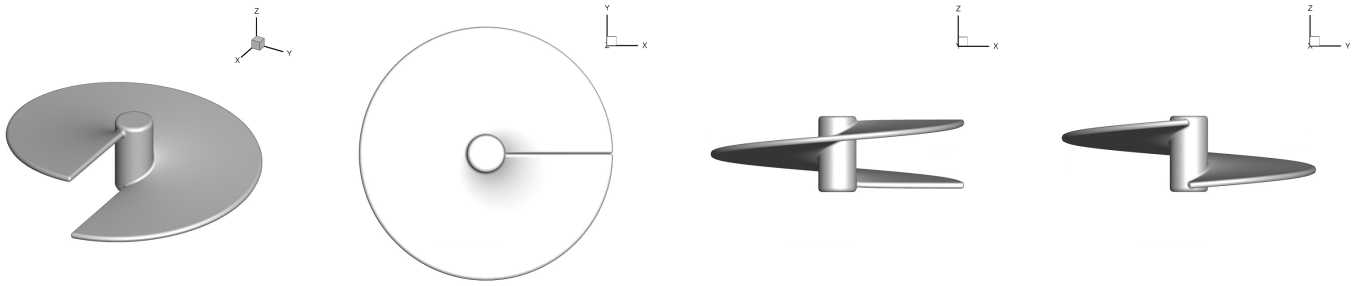


FIGURE 3.1: Four views of screw for case 1 (Low Pitch)

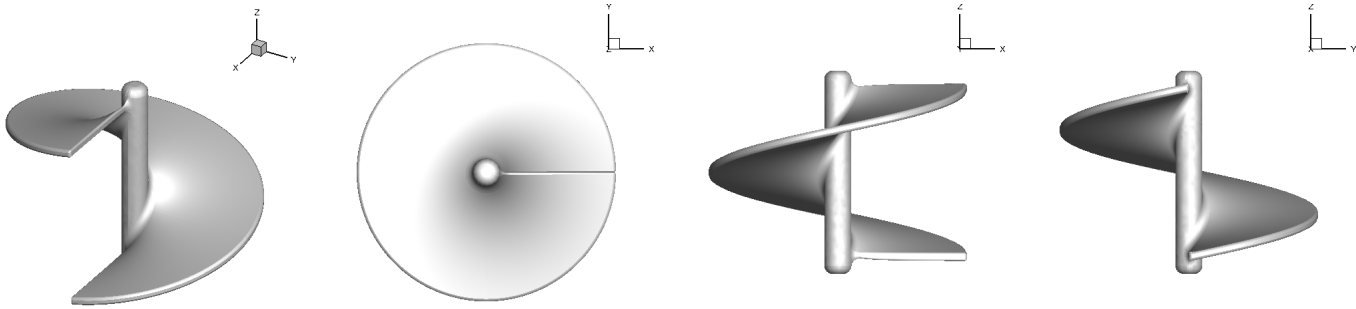


FIGURE 3.2: Four views of screw for case 2 (High Pitch)

same for each case, the change in pitch, hedral, or taper affects the total aerodynamic surface area of the aerial screw.

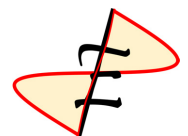
The baseline screw generated for the analysis can be seen in Figure 3.1. This shape was inspired by Leonardo's aerial screw, and designed to have a similar height to radius ratio but with no taper and only one turn for simplicity. The second geometry seen in Figure 3.2 investigates the effect of increased screw pitch. The third geometry, seen in Figure 3.3, and fourth geometry, seen in Figure 3.4, study the effects of adding an anhedral to the screw and taper respectively, and these geometries have the same increased pitch as the second geometry.

TABLE 3.1: Specifications of four different aerial screw geometries analyzed with CFD

Test Case	Pitch/Radius	Anhedral	Taper Ratio	Surface Area (m ²)
Case 1 (Low Pitch)	0.5	0°	1:1	7.4
Case 2 (High Pitch)	1.31	0°	1:1	7.9
Case 3 (Hedral)	1.31	10°	1:1	8.0
Case 4 (Tapered)	1.31	0°	1:2	4.8

3.2 Validation with the Experiments

Before understanding the influence of the design variables on the aerodynamics of the aerial screw, the results obtained from CFD were validated with the experimental data. Figure 3.6 shows power loading versus disk loading for both experiments and CFD predictions. The validation geometry is case 3 in Table 2.1 which is the case 2 in Table 3.1, and the data is compared at two different RPM.



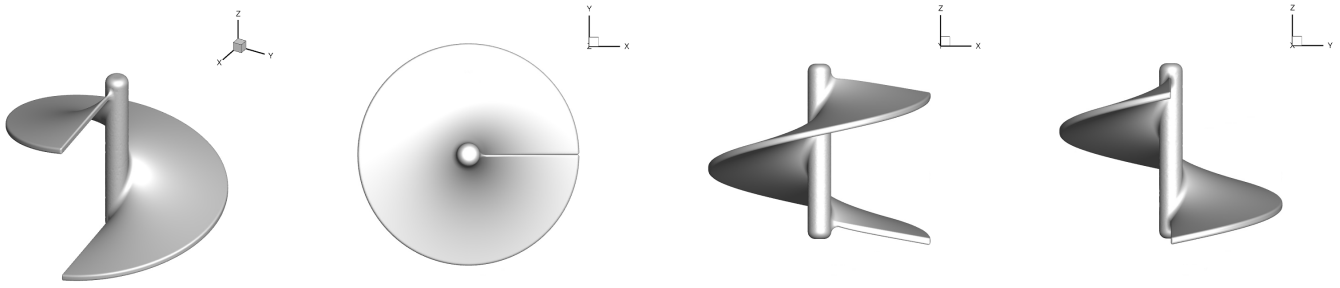


FIGURE 3.3: Four views of screw for case 3 (Hedral)

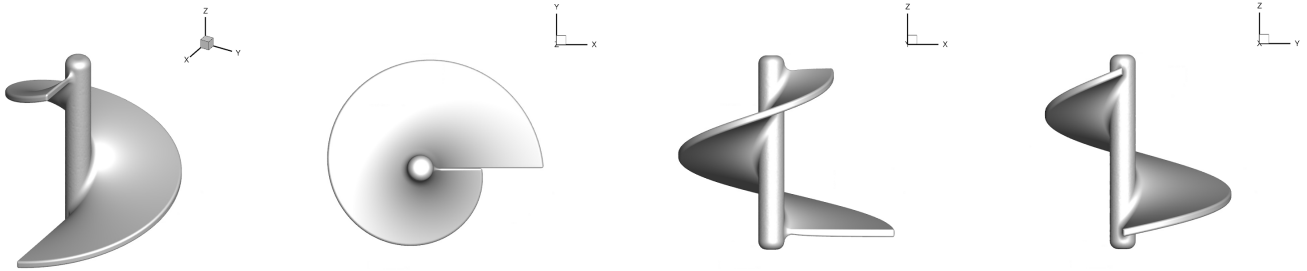


FIGURE 3.4: Four views of screw for case 4 (Tapered)

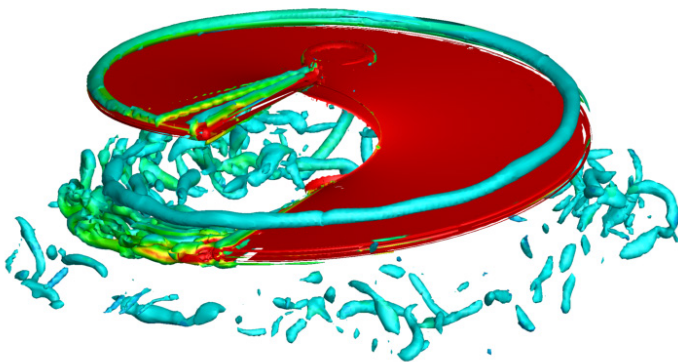


FIGURE 3.5: Case 1 aerial screw in hover with da Vinci vortex

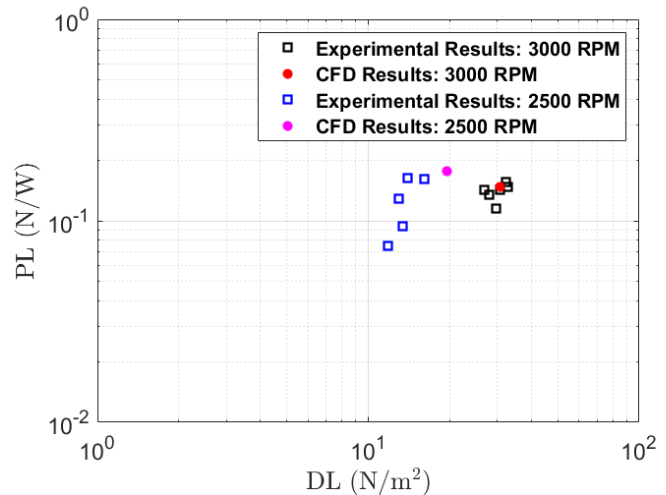
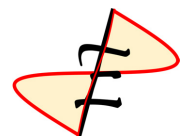


FIGURE 3.6: Validation with experiments

The results obtained from CFD solver are in agreement with the experimental results. The scatter in the experimental dataset may be attributed to the uncertainties in the measurements caused by vibrations due to force imbalances.

3.3 The da Vinci Code: Thrusting Mechanism of Aerial Screw

All the test cases were examined for hover performance using CFD. The solver assumes a Spalarat-Almaras one equation turbulence model. The thrust generation mechanism, revealed by the CFD flow field, is attributed to the stable helical “da Vinci” vortex attached with the top surface of



the screw. Figure 3.5 shows the da Vinci vortex on a typical airscrew geometry in hover. The vortex creates a pressure difference between the top and bottom surfaces by creating a suction on the top surface. The vortex remains suspended within 10 - 20% R from the rotor tip, while the inboard sections are inactive for thrust contribution.

The performance of the aerial screw is strongly coupled to the strength of the da Vinci vortex, and is both a key enabler and a design driving parameter. The effect of each design variable was examined using the test matrix and the results can be seen in Table 3.2. Increasing the pitch of the screw, case 2 dramatically increased the thrust and power loading of the aerial screw. Adding an anhedral, case 3 has no significant effect on hover performance. The thrust coefficient for the tapered geometry, case 4, is lower than that of the untapered, case 2.

TABLE 3.2: Performance estimates of the aerial screws

Test Case	C_T	C_P	FM	C_T/A
Case 1 (Low Pitch)	0.0051	0.0023	0.11	0.0007
Case 2 (High Pitch)	0.0439	0.0125	0.52	0.0055
Case 3 (Hedral)	0.0437	0.0123	0.52	0.0054
Case 4 (Tapered)	0.0274	0.0080	0.40	0.0057

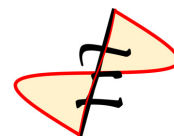
3.4 The Geometry of *Elicó*

For *Elicó*'s rotor design, the tapered geometry, case 4, was selected. While the untapered geometries, cases 2 and 3, produced higher thrust, Table 3.2 indicates that it is mostly due to the increased surface area. The surface of a tapered screw is more efficient at generating lift than the untapered cases. For this reason, a tapered screw requires a smaller surface area and therefore is a lighter rotor. For the tapered geometry, the strength of the da Vinci vortex is constant throughout the screw, making the thrust distribution nearly constant for the overall screw surface. This is because the taper ensures the spirally outward drifting da Vinci vortex to remain on the screw surface. Further, the thrust coefficient normalized with the effective lifting surface area is slightly higher for the tapered geometry confirming a stronger da Vinci vortex. Also, the larger radius sections in the tapered geometry contribute more for thrust and leads to a lighter, more thrust efficient aerial screw design.

The vorticity field around *Elicó*'s rotor can be seen in Figure 3.7. The left image is shown for screw orientation.

Figure 3.8 shows the variation of pressure along sections of constant span location with azimuth, and Figure 3.9 shows radial variation of the pressure distribution at a fixed azimuth on *Elicó*'s rotor surface. The blue curves are for the top surface and the red curves for the bottom.

The pressure distribution in Figure 3.8 clearly shows that the near-tip locations contribute greatly to the thrust and the near-hub locations are relatively passive.



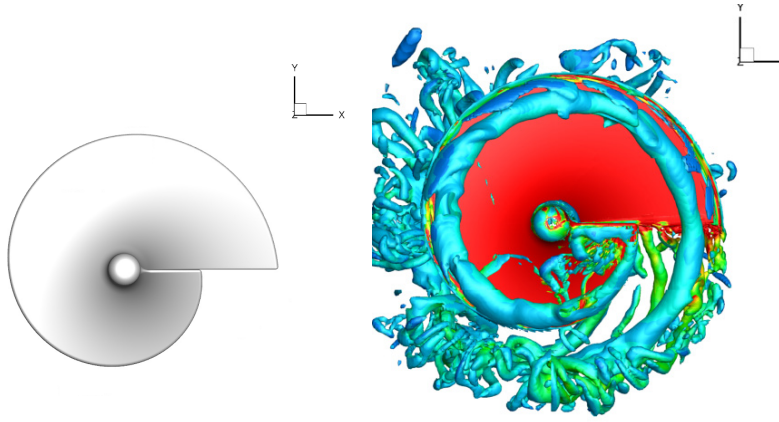


FIGURE 3.7: Vorticity isosurfaces of the *Elico*'s rotor

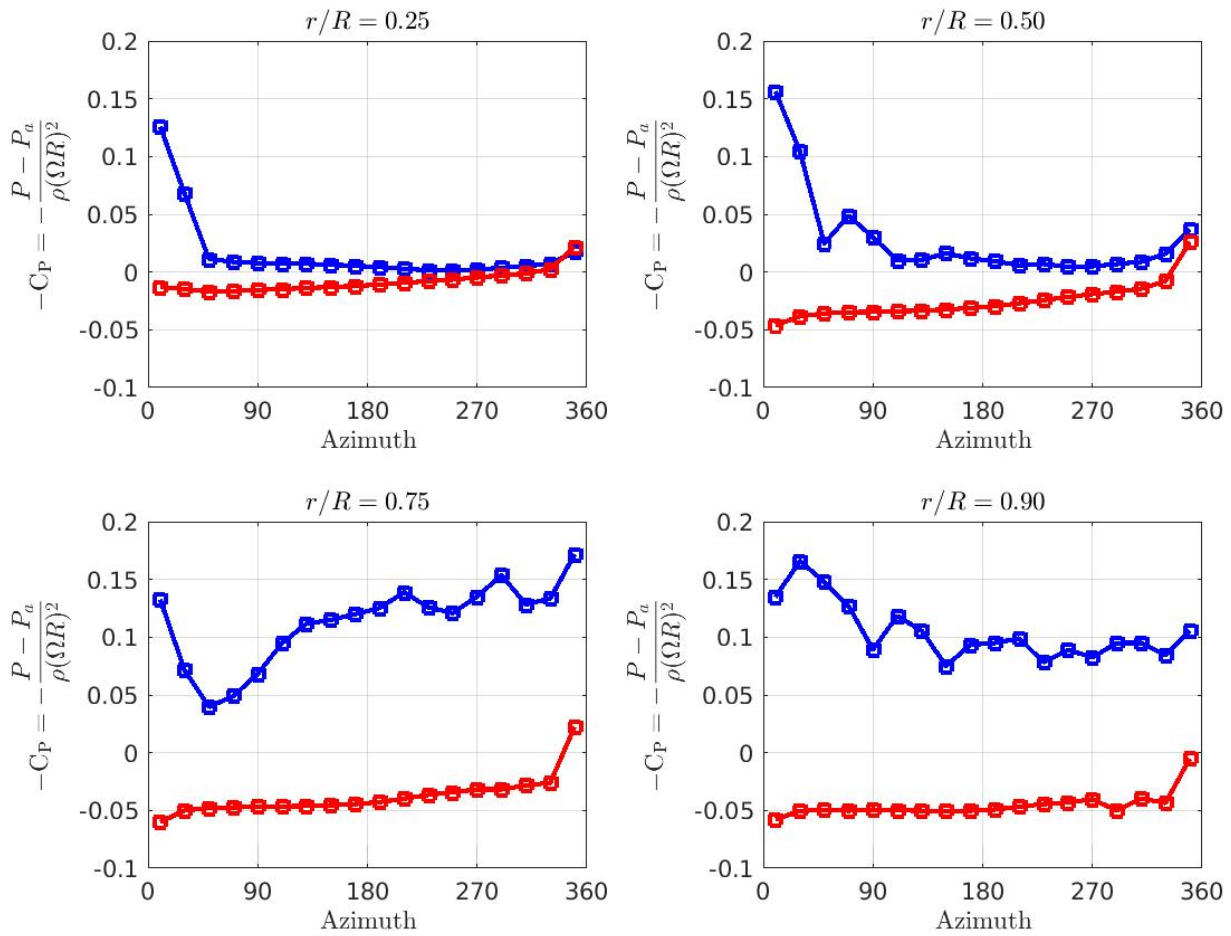
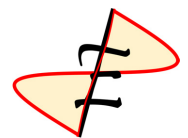


FIGURE 3.8: Azimuthal variation of pressure



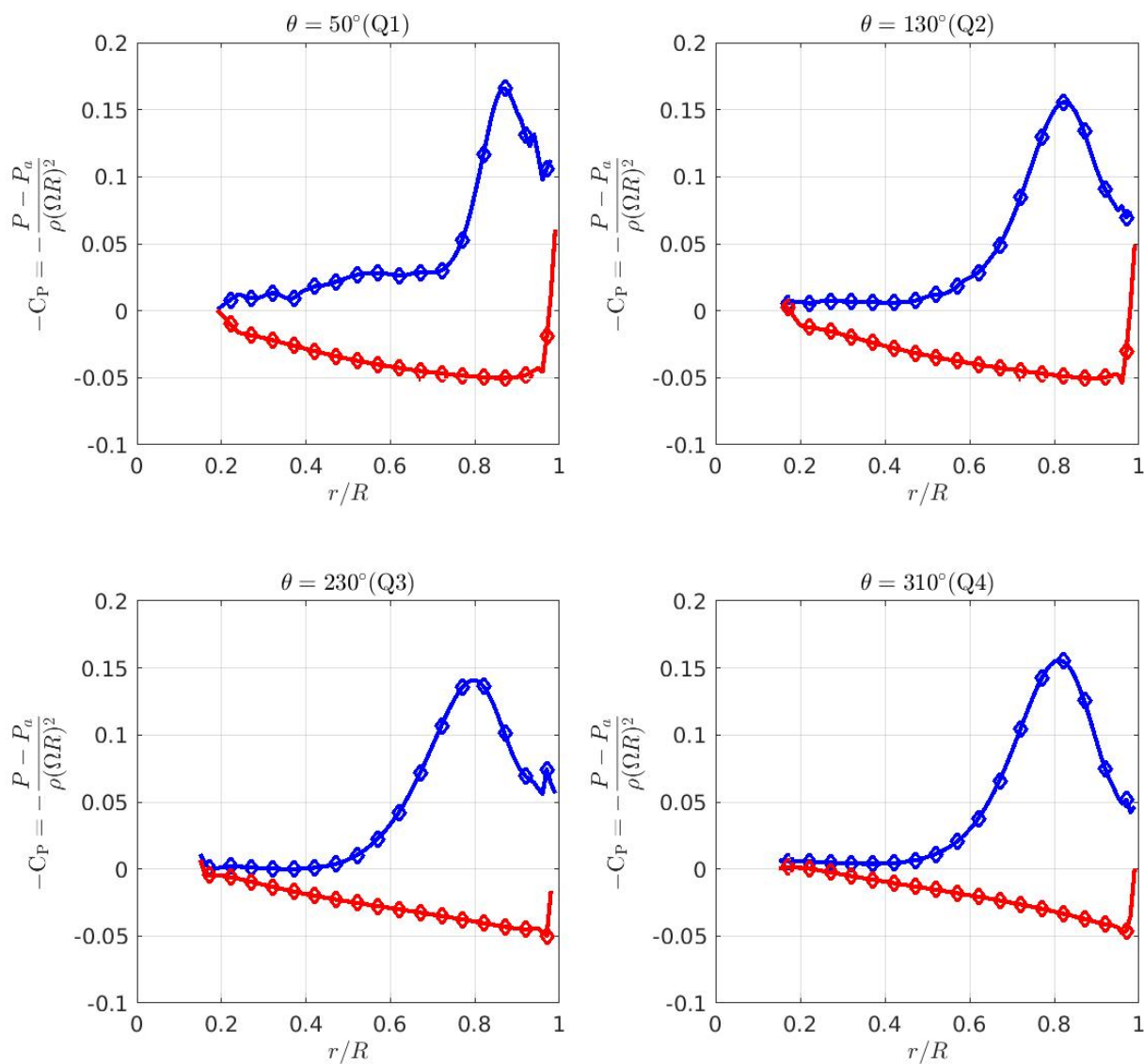


FIGURE 3.9: Radial variation of pressure

The variation of pressure along the radial direction is constant after the da Vinci vortex is fully developed. A suction peak can be seen in the pressure difference at the location of the vortex in Figure 3.9

Once the geometry for *Elico* is chosen, it was tested for the effect of varying tip speed and size on the performance.

3.4.1 Performance Variation with Tip Speed

The baseline case of *Elico* rotor was originally tested at a tip mach number of 0.25. In order to explore the effect of tip speed on the rotor's performance, test cases with different tip speeds were analyzed. The results can be found in Table 3.3.

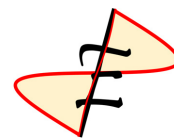


TABLE 3.3: Performance of *Elico*'s rotor at different tip speeds

M_{tip}	C_T	C_P	FM
0.10	0.0275	0.0088	0.37
0.25	0.0265	0.0080	0.38
0.30	0.0263	0.0074	0.41
0.40	0.0260	0.0075	0.40

TABLE 3.4: Performance of *Elico*'s rotors of different sizes

R (m)	R (ft)	C_T	C_P	FM
0.0762	0.25	0.0272	0.0080	0.40
0.1524	0.50	0.0272	0.0078	0.41
1.5240	5.00	0.0261	0.0074	0.40
3.0480	10.0	0.0260	0.0071	0.42

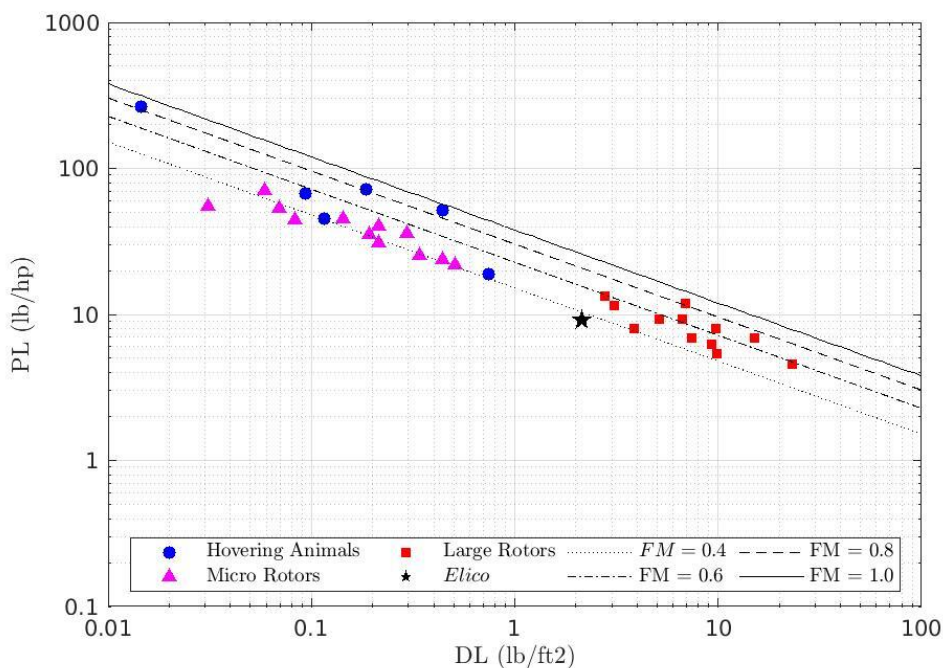
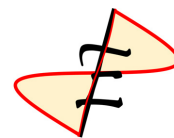
The thrust coefficient is nearly constant with varying tip speed. The power coefficient increases with decreasing tip speed, owing to the effect of low Reynolds numbers.

3.4.2 Performance Variation with Size

The baseline case of *Elico* rotor was originally tested at the experimental scale radius of 7.6 cm (3 in). To understand the effect of size of the rotor on performance, test cases with different length scales were analyzed. The results can be found in Table 3.4.

3.5 Summary

The thrust mechanism of an aerial screw is understood and the effects of a representative set of design variables on the performance is studied. The rotor geometry of *Elico* is arrived at, after a critical review of the effect of each design variable in the thrust generation. A comparison of *Elico* rotor performance to that of various aircrafts at different scales can be seen in Figure 3.10.

FIGURE 3.10: PL vs DL for various hover vehicles and *Elico* rotors

4 Configuration Selection

With a physical understanding of how the aerial screw operates and an estimate to its hover efficiency, it becomes possible to move forward with the design of a vehicle around this unique geometry. The VFS Design challenge requires the vehicle to be based on Leonardo da Vinci's aerial screw concept with the requirements that the vehicle should be able to take off vertically, cruise at least 20 m in 60 seconds, and land vertically. The total mission time is 70 seconds in near hover conditions. The challenge at hand is to transform Leonardo's dream into reality, a flying vehicle.

The Analytical Hierarchy Process (AHP) was used to evaluate the design drivers and quantify the voice of the customer. In this method, each vehicle attribute is scored against each other to obtain the relative importance of each attribute. Each member of the team constructed an AHP matrix based on their interpretation of the Request for Proposals (RFP) and Table 4.1 represents the average consensus of the team.

Using the results of the AHP, a Pugh matrix was constructed to evaluate potential design configurations. Each configuration receives a score for each attribute, compared to a baseline. Multiplying these weights with the weights from the AHP and taking the sum gives an overall score for the configuration.

4.1 Voice of the Customer

4.1.1 Selection Criteria

After analysis of the RFP, 8 key criteria for the design were selected and are listed below:

- **Aesthetics:** The design should have minimal deviations from Leonardo da Vinci's vision.
- **Controllability:** Effectiveness of maintaining stability and maneuverability in each flight mode. The vehicle is required to stay within a 10 m radius on take-off and landing.
- **Crew Safety:** The vehicle must be suitable for demonstrator-level operation by the ground crew and pilot.
- **Empty Weight Fraction:** Since the aerial screw is heavier than a typical rotor, the vehicle must save weight in other areas to be effective.
- **Hover Performance:** The total power required to maintain hover. This is the primary flight mode considered since the cruise speed is low enough to be nearly hover.
- **Life-Cycle Cost:** The total cost to develop, build, operate, and maintain the vehicle should be low.
- **Range:** The vehicle is required to fly at least 20 m. Additional consideration is given for distance exceeding the required range.
- **Robustness:** The number of missions before critical component failure. This metric encapsulates system complexity as well as component reliability and dictates the vehicle's lifetime.

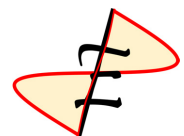


TABLE 4.1: AHP Weights

	Range	Aesthetics	Weight	Crew Safety	Hover Performance	Cost	Robustness	Maneuverability	Normalized Priority
Range	1.00	0.21	0.71	0.43	0.19	0.68	0.72	0.41	0.049
Aesthetics	4.88	1.00	3.48	2.09	0.90	3.33	3.51	1.99	0.240
Weight	1.40	0.29	1.00	0.60	0.26	0.96	1.01	0.57	0.069
Crew Safety	2.34	0.48	1.67	1.00	0.43	1.60	1.68	0.95	0.115
Hover Performance	5.40	1.11	3.85	2.31	1.00	3.69	3.88	2.20	0.265
Cost	1.47	0.30	1.04	0.63	0.27	1.00	1.05	0.60	0.072
Robustness	1.39	0.29	0.99	0.60	0.26	0.95	1.00	0.57	0.068
Maneuverability	2.46	0.50	1.75	1.05	0.46	1.68	1.77	1.00	0.121

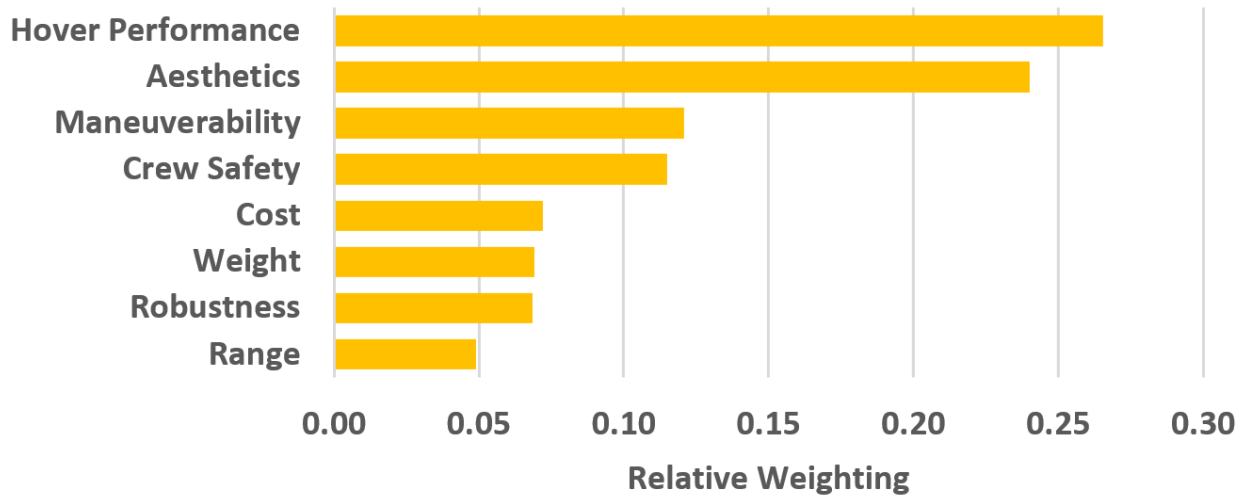
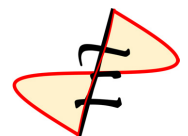


FIGURE 4.1: Relative weighting of design criterion from the AHP

4.1.2 Analytical Hierarchy Process

With the 8 criteria specified from the RFP, the Analytical Hierarchy Process (AHP) was implemented to quantify the relative importance of each criteria. The AHP, shown in Table 4.1, then allows for quantitative comparisons between different design concepts. The entries of each cell represent the importance of the design criteria at the beginning of the row compared to the design criteria at the column header. The values range from 1/5 (much less important) to 5 (much more important). The normalized priority vector is calculated by normalizing each entry by the column sum, then averaged by row. Each team member filled out the table individually, the averaged result is shown in Table 4.1 and Figure 4.1.

These results show that hover performance is the highest priority, followed closely by vehicle aesthetics. Since the vehicle is in near hover conditions for the entirety of the mission, the best design will minimize



the power required to maintain hover. Additionally, the RFP is clear in its desire for the vehicle to maintain the aesthetics of the original design.

4.2 Potential Configurations

Over the past 500 years, it has been observed that the most common critique of Leonardo da Vinci's helicopter design is the lack of mechanism to oppose the torque of the main rotor. Another critical concern for the design of this vehicle is ensuring adequate control. Leonardo's sketch indicates no mechanism to keep the vehicle level in hover or move in forward flight. Therefore, these two needs are addressed independently during the configuration selection. The options considered to address these needs are discussed below.

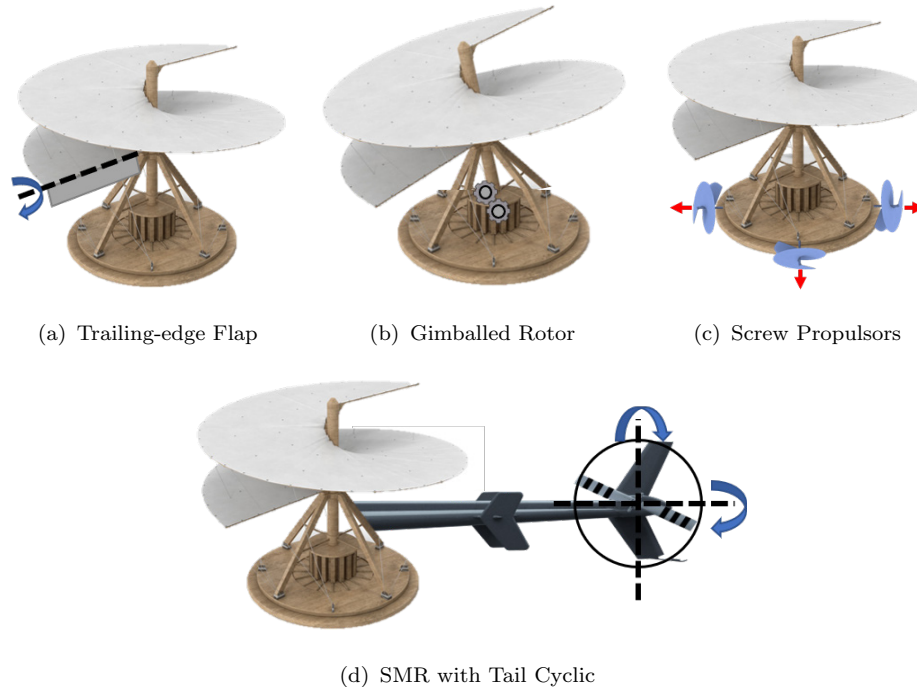


FIGURE 4.2: Conceptual design concepts for vehicle control solutions.

4.2.1 Vehicle Control Solutions

For multi-rotor configuration (4+ rotor), the thrust and torque of each rotor is sufficient for control. The number of rotors is studied in Section 5.4.2. For single or twin rotor concepts, a more novel control method is required. The main mechanism to control a conventional rotor is to vary the blade pitch cyclically as it rotates around the hub. However, changing the pitch of the aerial screw requires a change in surface area, due to the helical nature of the structure. This is impossible without complex mechanisms to extend the surface, so other alternatives must be explored to maintain vehicle stability.

- **Multi-Rotor:** Because RPM control of the motor is the simplest solution, it is used as the baseline for all other rotor control solutions.
- **Trailing Edge Flap:** The thrust of the screw could potentially be varied by a single trailing edge flap at the bottom of the screw. This is a relatively inexpensive and light-weight solution. However, a previous study with a single conventional rotor with a flap in the wake showed the vehicle is unstable near the ground and leads to a significant loss of power [7].

- **Gimballed Rotor:** Instead of trying to vary the rotor thrust, one option is to tilt the rotor both longitudinally and laterally to change the direction of thrust. The system required to provide this motion would be exceptionally heavy and complex, leading to a less efficient design.
- **Screw Propulsors:** A vehicle with the center of gravity carefully placed below a single aerial screw could utilize propulsors for translational control. These propulsors would also be aerial screws and, by placing them off axis, could provide attitude control as well. However, these screws add additional weight and complexity for minimal gains in control authority
- **SMR with Tail Cyclic:** A single main rotor (SMR) with a conventional tail rotor could be modified to include cyclic control. Adding additional swashplate controls would increase the weight in the tail as well reduce the system robustness. Lastly, while the tail rotor could provide ample yaw and pitch control, the roll control is severely limited.

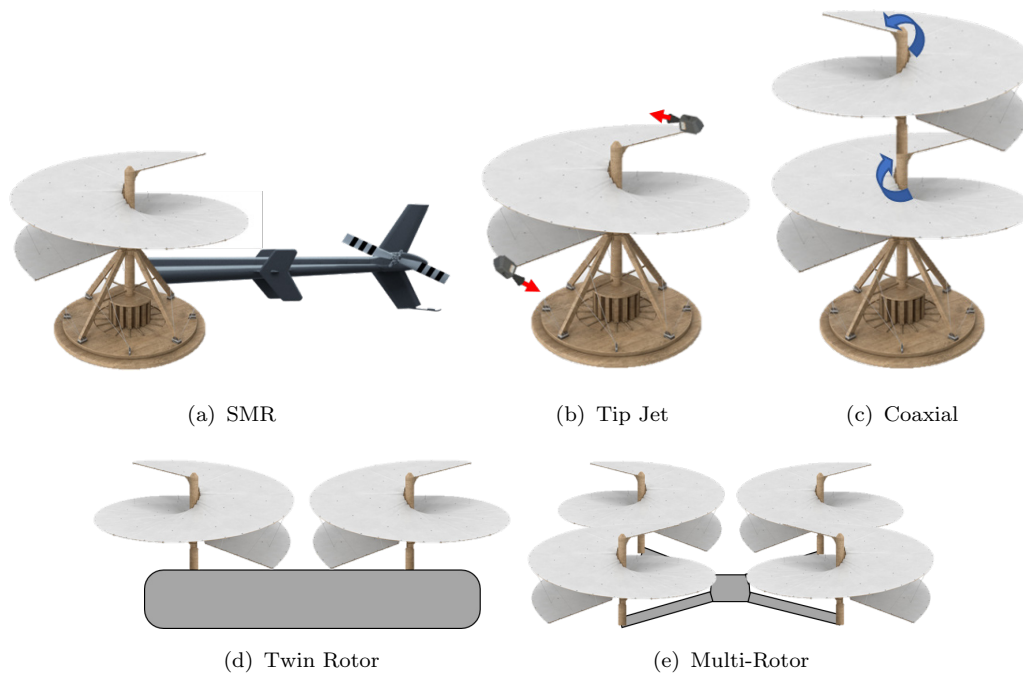


FIGURE 4.3: Conceptual design concepts for anti-torque solutions

4.2.2 Anti-Torque Solutions

- **Single Main Rotor (SMR):** This configuration utilizes a single main aerial screw rotor for lift and propulsion and a conventional tail rotor for anti-torque. It is used as a baseline configuration for all comparisons.
- **Tip-Jet:** The use of a single aerial screw matches well with Leonardo's first sketch. But, tip-jet drive is inefficient at powering the rotor. Additionally, supplying fuel to the rotor tip introduces additional complexity, and therefore reduced robustness, to the rotor structure.
- **Coaxial Rotor:** A coaxial rotor provides a torque balance without extensions of the structure for additional rotors. However, the interference between the two rotors reduces the efficiency of conventional rotors. It is unknown how drastically this would affect an aerial screw. The coaxial shaft also reduces the robustness of the rotor system. By eliminating the tail rotor, the vehicle is safer for flight and ground crew operating near the vehicle.

- **Twin Rotor:** A twin rotor vehicle has two non-overlapping rotors placed either side-by-side or in a tandem configuration. Since the rotors are separated from each other, there is less uncertainty on how the two aerial screws would operate together. The additional rotor allows for larger moments to be carried along one access as well as the possibility to utilize a lift offset. However, like the single aerial screw concepts, augmentation is needed to provide control.
- **Multi-Rotor:** The multi-rotor uses differential thrust and torque to maintain vehicle attitude and rates. While incurring penalties to vehicle range and weight, the simple control scheme allows for much higher maneuverability than any other design. This was informed by the first design challenge, rotor control.

4.3 Configuration Selection

Selecting the vehicle configuration, consisting of rotor configuration and control methods, was done using a Pugh matrix as a decision making tool. The weights from the AHP in Table 4.1 were used to evaluate each set of design concepts discussed in Section 4.2. The first column is used as a baseline configuration and each subsequent concept is rated against it. Values in this matrix range from -3 (much worse) to +3 (much better) in comparison to the baseline decision. The results analyzing each vehicle control is shown in Table 4.2 and anti-torque methods are analyzed in Table 4.3. The multi-rotor and trailing-edge flap designs have similar scores when evaluating vehicle control methods. However, since multi-rotor control offers a simpler solution through RPM control and the effectiveness of a trailing edge flap is difficult to evaluate for the aerial screw concept, the multi-rotor design is selected. For anti-torque concepts, excluding the multi-rotor, a trailing-edge flap control is assumed to evaluate the maneuverability of the vehicle. Because of the penalty to maneuverability, no design is able to score higher than the multi-rotor concept to provide anti-torque. Therefore, *Elico* was selected to be a multi-rotor design. Detailed sizing and weight estimates in Chapter 5 were used to determine the number of rotors in this design.

TABLE 4.2: Pugh Decision Matrix: Vehicle Control

Vehicle Control	Weight	Multi-Rotor	Tailrotor Cyclic	Screw Propulsors	Trailing- Edge Flap	Gimballed Rotor
Hover Performance	0.265	0	-1	-1	0	0
Aesthetics	0.240	0	1	1	1	1
Crew Safety	0.121	0	-1	0	0	-1
Maneuverability	0.115	0	-3	-3	-3	-1
Cost	0.072	0	1	0	1	0
Robustness	0.069	0	-1	0	-1	-2
Weight	0.068	0	1	0	1	-2
Range	0.049	0	0	0	0	0
		0	-0.420	-0.371	-0.034	-0.271

TABLE 4.3: Pugh Decision Matrix: Rotor Configuration

Anti-Torque Solutions	Weight	SMR Tail Rotor	Twin Rotor	Multi-Rotor	Tip Jet	Coax
Hover Performance	0.265	0	1	1	-3	-1
Aesthetics	0.240	0	-1	-1	2	-1
Crew Safety	0.121	0	2	2	1	1
Maneuverability	0.115	0	1	3	0	-1
Cost	0.072	0	-1	-2	-1	-2
Robustness	0.069	0	1	1	-1	-2
Weight	0.068	0	0	-1	0	-1
Range	0.049	0	-1	-1	-1	1
		0	0.330	0.420	-0.386	-0.801

5 Preliminary Vehicle Sizing

The configuration selection for *Elico* determined that a multi-rotor vehicle is the best design for this mission. Preliminary sizing using a specialized sizing code is now required to analyze the vehicle components' optimal size and corresponding weights. Modified Momentum Theory was used to determine the performance and weight metrics for the specified mission, and the aerodynamic analysis used results obtained through Computational Fluid Dynamics (CFD) to size the aircraft.

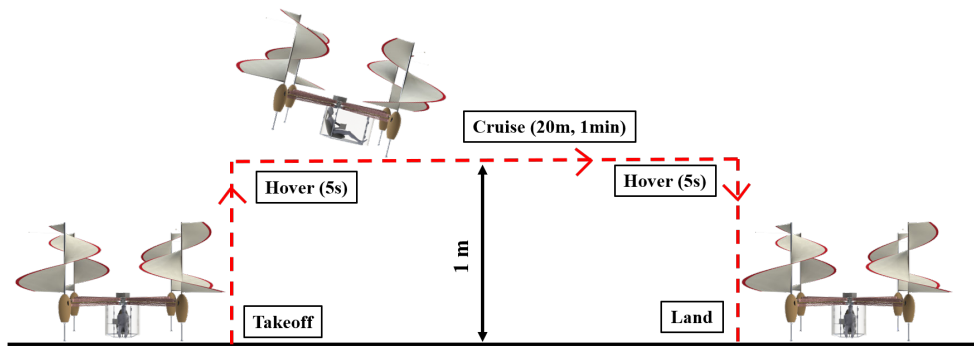


FIGURE 5.1: Mission specified by the RFP

5.1 Mission Profile

The size of the vehicle depends on the mission requirements. As seen in Figure 5.1, the RFP mission requires *Elico* to:

1. Vertically takeoff to an altitude of at least 1.0 meter;
2. Hover for 5 seconds at this location;
3. Fly a distance of at least 20 meters with a flight time of at least 1 minute;
4. Hover for 5 seconds at this location;

5. Land vertically.

The payload is specified as one person (pilot or passenger) weighing 60 kg. To give the vehicle a higher capability, *Eluco* was sized for a hover time of 3 minutes. Since hover requires more power than cruise, this ensures *Eluco* can perform the specified mission with sufficient power reserves, or extend its range beyond the requirements.

5.2 Design Constraints

1. Solidity ≥ 1

The RFP requirement for a solidity greater than or equal to 1.0 constrains the choice of configuration. For conventional rotors, solidity is defined by Equation 5.1, where N_b is number of blades per rotor, c is chord length, and R_{max} is the maximum rotor radius. Effectively, a solidity ≥ 1.0 means that the area of the blades must be greater than or equal to the rotor disk area. In the case of an aerial screw, the solidity is defined by the same equation but with the blade area being defined as the “2-D projection of the aerial screw (looking down the rotor shaft)”, and the disk area being defined as “the area of circle swept by the largest radius.” [8]

$$\sigma = \frac{\text{Blade Area}}{\text{Disk Area}} = \frac{\text{Projected Screw Area}}{\pi R_{max}^2} \quad (5.1)$$

2. Single-Bladed Rotor

The RFP states that each rotor must be single-bladed, to be faithful to Leonardo da Vinci’s original concept for the aerial screw design.

$$FM = \frac{C_T^{3/2}}{\sqrt{2}C_P} \quad (5.2)$$

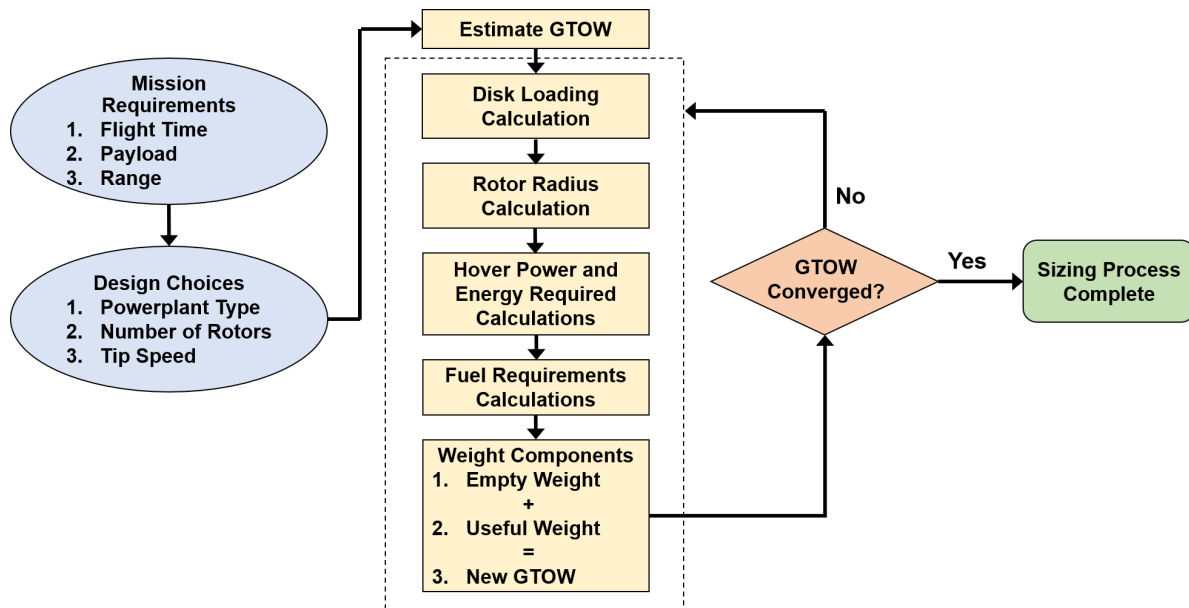
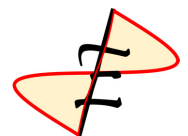


FIGURE 5.2: Process for preliminary sizing; iteration steps are within the dotted lines



5.3 Methodology

Sizing analysis followed a conventional iteration process, however the weight models for *Elicó* are unique and have been refined throughout the design process. The iteration process, seen in Figure 5.2, uses mission parameters as inputs, as well as a constant Figure of Merit (FM) and coefficient of thrust obtained from CFD aerodynamic results, to begin the process. FM is defined by Equation 5.3, where C_T is the coefficient of thrust and C_P is the coefficient of power. Based on the CFD results in Chapter 3 and taking into consideration the interactional aerodynamic effect discussed in Chapter 14, a conservative hover FM value of 0.35 was selected. While Chapter 3 selected an aerial screw with a FM of 0.41 to be the design point for *Elicó*, the sizing analysis discussed here uses the conservative FM estimate of 0.35 to account for any potential losses.

$$FM = \frac{C_T^{3/2}}{\sqrt{2}C_P} \quad (5.3)$$

The sizing analysis was performed over a tip speed (ΩR_{max}) parametric sweep. For each specified tip speed, the disk loading (DL) is calculated using Equation 5.4.

$$DL = C_T \cdot \rho \cdot (\Omega R_{max})^2 \quad (5.4)$$

The rotor radius is then calculated using Equation 5.5, where the thrust T can be estimated to be equal to the gross takeoff weight (GTOW). Next, the total hover power and energy required are then calculated using Equations 5.6 and 5.7, where the thrust T can again be estimated to be equal to the GTOW.

$$DL = \frac{T}{A} = \frac{T}{\pi R_{max}^2} \quad (5.5)$$

$$P_{req,h} = \frac{T}{FM} \sqrt{\frac{DL}{2\rho}} \quad (5.6)$$

$$E_{req,h} = P_{req,h} \cdot t_h \quad (5.7)$$

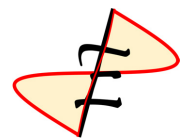
As this mission requires forward flight at a low speed of 0.33 m/s, for sizing purposes *Elicó* was assumed to be hovering for the entirety of the 3 minute flight time. This gives a more conservative estimate for the aircraft performance and weight targets.

With the total required power, the amount of fuel required can be determined depending on the type of powerplant selected. For the battery powered design, the fuel weight is the weight of the battery. The fuel weight and the payload (pilot or passenger weight, 60 kg) make up the useful weight.

Finally, the empty weight is calculated, consisting of the drive group, structural group, and contingency weight. Weight components were determined using physics based weight equations. Conservative estimates were used to allow for a margin of error, and the additional contingency group included an overhead of 30 kg and allowed for miscellaneous components. The components of each group are listed below.

1. Drive Group:

The drive group components change with powerplant architecture, varying between turbo-electric, pure turboshaft, and all-electric. For this analysis, these are defined as follows: “Turbo-Electric”



configuration includes a turboshaft engine that powers a generator, which then powers electric motors. The “Pure Turboshaft” configuration implements a conventional turboshaft engine. The “All-Electric” configuration utilizes currently available lithium-ion batteries (150 Wh/kg usable specific energy) to power electric motors. The electric motors are sized using the weight trend equation detailed in [9].

Pure Turboshaft:	Turbo-Electric:	All-Electric:
(a) Rubberized turboshaft engine	(a) Rubberized turboshaft engine	(a) Lithium-ion batteries
(b) Gearboxes	(b) Gearboxes	(b) Gearboxes
(c) Driveshafts	(c) Generator	(c) Electric Motors
(d) Rotor Speed	(d) Electric Motors	(d) Rotor Speed
Controllers	(e) Rotor Speed	Controllers
	Controllers	

2. Structural Group:

The structural group consists of the aerial screws, fuselage, arms extending from the fuselage to the aerial screws, and the landing gear.

(a) Rotors:

The aerial screw consists of the skin, spars, and shaft, detailed in Chapter 7. The skin was chosen to be a lightweight fabric covering both sides of the surface; the spars are manufactured using lightweight carbon fiber; the rotor shaft is a hollow aluminum shaft. All are unconventional designs and required unique weight estimations.

(b) Fuselage:

The open fuselage concept reduced the weight compared to conventional rotorcraft.

(c) Arms: The arms extending from the fuselage to the rotors are constructed using cellular truss technology, discussed in detail in Chapter 8. The weight of each arm is dependent on the rotor radius and the cellular truss weight per unit length.

(d) Landing Gear

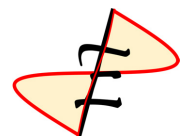
3. Contingency Weight (30 kg):

The contingency weight is added to account for components such as the necessary vibration weight discussed in Chapter 7, cockpit instruments, furnishings, and any other unforeseen parts.

A new GTOW value is obtained from the useful weight and empty weight, and the process iterates until it converges on a single GTOW.

5.4 Trade Studies

The final design for *Eluco* was decided based on parametric studies. One design choice was the type of powerplant system, discussed in Section 5.4.1. The configuration selection shown in Table 4.3 showed that a multi-rotor vehicle is optimal for this mission; Section 5.4.2 discusses the optimal number of rotors for this multi-rotor vehicle.



5.4.1 Propulsion System

Figure 5.3 compares the GTOW, rotor radius, and total power required for each of the powerplant options discussed. A turbo-electric powerplant is the least optimal choice for the specified mission as it results in the highest GTOW and required power at any given disk loading. At low disk loadings, the turbo-electric GTOW and hover power both increase quickly due to the high torque and corresponding increasing generator weight.

When comparing the remaining two powerplant choices, pure turboshaft initially seems to be the superior option as the GTOW, radius, and required power are all lower than those for the all-electric configuration. However, rotors driven by a turboshaft engine are less effective at aircraft control through variable RPM. For this reason, pure turboshaft is not a viable option. An all-electric powerplant was chosen as it results in low GTOW and required power, and allows for flight control through variable RPM. Additionally, a powerplant with all electric components inherently has more potential for less vibration compared to a conventional turboshaft engine.

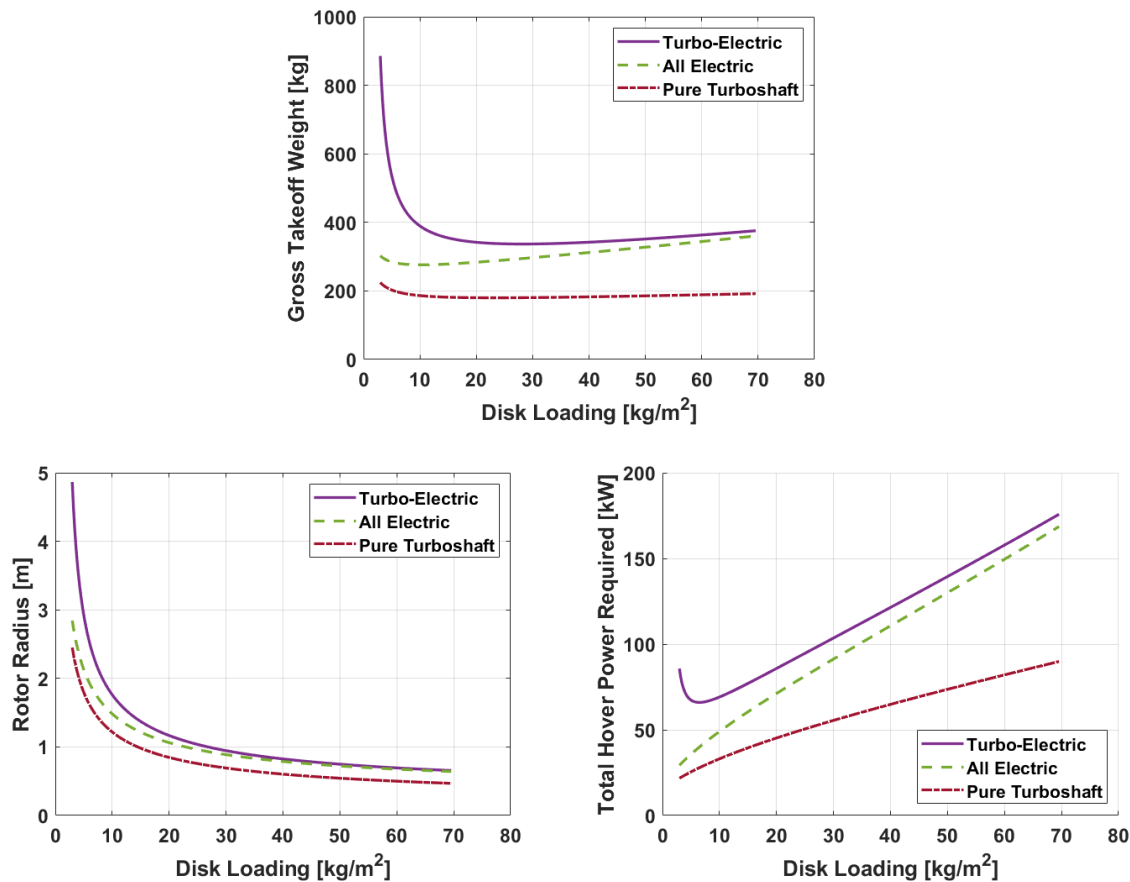
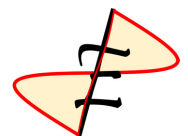


FIGURE 5.3: Gross takeoff weight, maximum rotor radius, and total hover power required vs disk loading for varying powerplant systems on an aerial screw quadcopter

5.4.2 Number of Aerial Screws

With the multi-rotor configuration chosen in Table 4.3, the optimal number of aerial screws had to be determined. Figure 5.4 shows how an increasing number of aerial screws also increases the GTOW



of the aircraft. This is due to the increase in the structural weight as the number of arms increases. However, the maximum rotor radius decreases with increasing number of rotors; with more rotors, each rotor needs to generate thrust equal to a smaller fraction of the GTOW and therefore a smaller radius is achievable. Finally, the total power required increases as the number of aerial screws increases. For the lowest power required as well as lowest GTOW, four aerial screws is the optimal number of rotors and a quadcopter configuration was chosen.

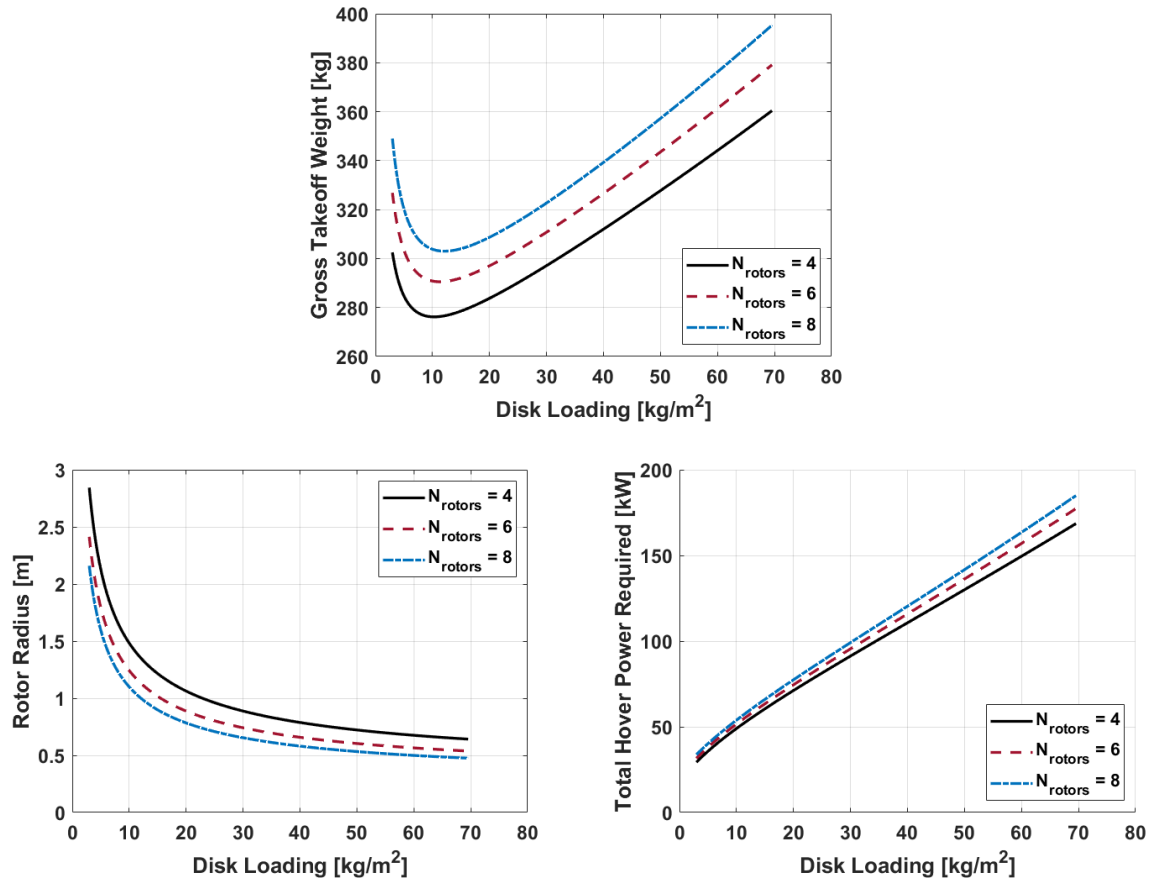


FIGURE 5.4: Gross takeoff weight, maximum rotor radius, and total hover power required vs disk loading for varying number of rotors

5.5 Summary of Aircraft Specifications

Elico is a revolutionary aircraft inspired by Leonardo daVinci's aerial screw concept. Sizing results showed that a battery powered quadrotor aircraft is the optimal choice for the specified mission. The GTOW, rotor radius, and total hover power required, as a function of disk loading, can be seen in Figure 5.5. Based on the Analytical Hierarchy Process (AHP) seen in Figure 4.1, hover performance is the highest priority when designing this vehicle. However, at the point of lowest required hover power the rotor radius is large at over 2.0 m (6.6 ft). To alleviate the possible structural issues with this large radius, the point of the lowest GTOW was chosen as the vehicle design point, shown by the vertical dotted lines in Figure 5.5. The final sizing specifications for *Elico* are found in Table 5.1.

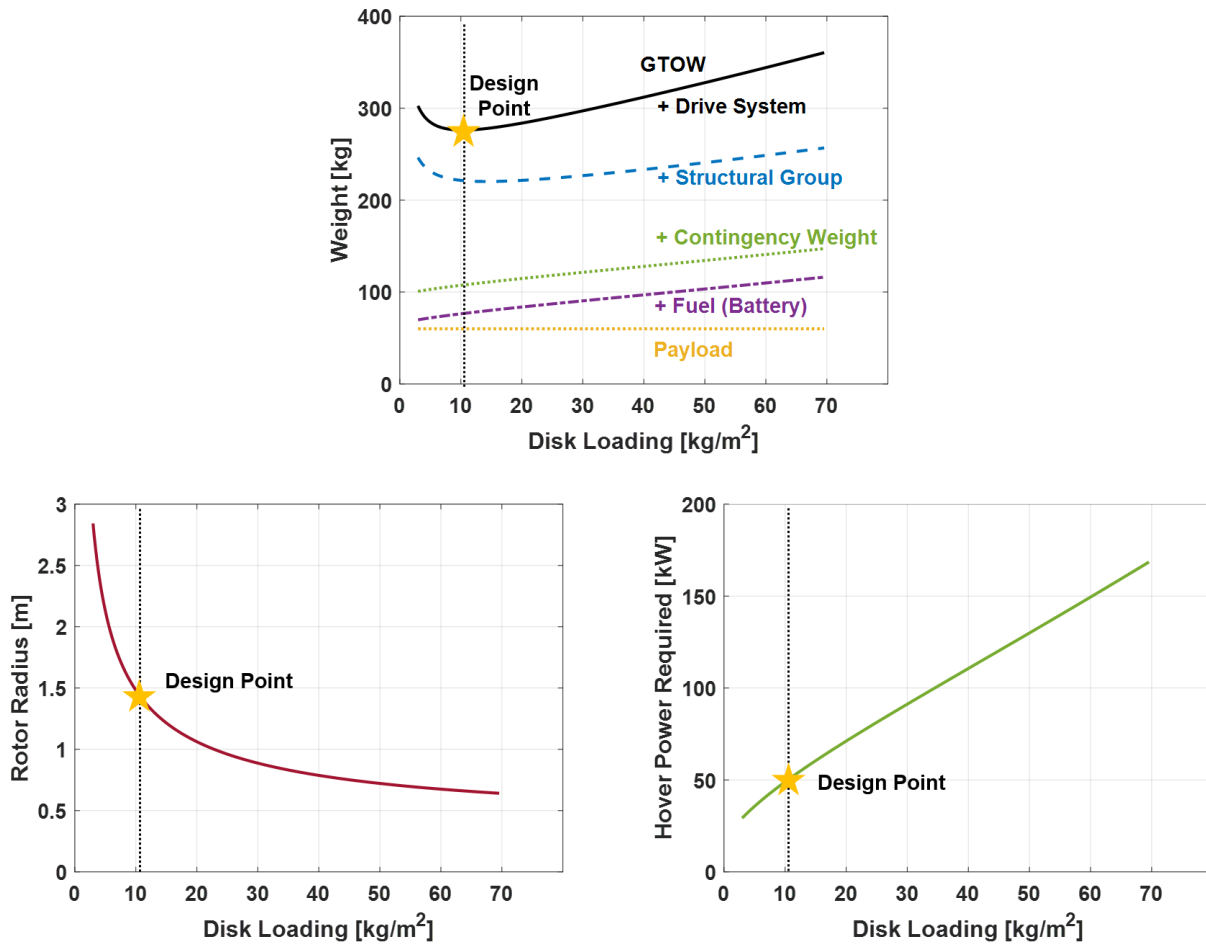
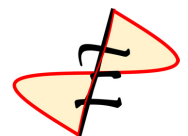


FIGURE 5.5: Weights, maximum rotor radius, and total hover power required vs disk loading for an all-electric quadcopter design

TABLE 5.1: Summary of aircraft specifications

Parameter	Metric	Imperial
Design gross takeoff weight	276 kg	609 lb
Empty Weight	200 kg	440 lb
Hover Power Required	50 kW	67 hp
Hover Figure of Merit	0.35	0.35
Maximum Rotor Diameter	2.92 m	9.58 ft
Disk Loading	10.4 kg/m ²	2.13 lb/ft ²
Hover Tip Speed	56 m/s	184 ft/s
Hover Rotor Speed	367 RPM	367 RPM
Mission Time	1.2 min	1.2 min
Reserves Time	1.8 min	1.8 min



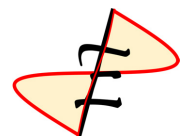
6 Vehicle Geometry

Elicó's appearance deviates from Leonardo da Vinci's aerial screw design in two major ways: a differently shaped aerial screw rotor as seen in Figure 6.1, and a quadcopter configuration as seen in Figure 13.1. As outlined in Chapter 4, the quadcopter configuration solves the two largest flaws of Leonardo's design, anti-torque and vehicle control. The change in rotor geometry is founded on extensive experimental tests and high-fidelity computational fluid dynamics (CFD) simulations.

The philosophy for *Elicó's* aerial screw design was focused on making systematic changes to Leonardo's original sketch to design a more efficient rotor. Figure 6.1 shows the design changes resulting in the final *Elicó* aerial screw design, beginning with Leonardo da Vinci's original sketch of an aerial screw seen in Figure 6.1a. The modifications resulting in *Elicó's* final aerial screw design are detailed below:

- a) Leonardo daVinci's original aerial screw sketch, seen in Figure 6.1a, was the starting design point.
- b) As a result of the experimental testing in Section 2.3.3, a single full revolution was decided as the optimal number of turns, as seen in Figure 6.1b.
- c) Next, the pitch of the aerial screw was modified to achieve a larger angle of attack and a greater lift and hover efficiency, shown in Figure 6.1c. The experimental results detailed in Section 2.3.1, specifically Figures 2.4 and 2.6, demonstrate how adding pitch to the aerial screw results in increased thrust and a higher Figure of Merit.
- d) A taper was applied to modify the aerial screw shape. This taper is necessary to keep the lift-generating da Vinci vortex, discussed in Section 3.3, attached over the length of the aerial screw surface.
- e) Modern materials were chosen to minimize rotor weight while maintaining necessary strength. Material selections and properties are discussed in Chapter 7. This was the final major change, and the converged design can be seen in Figure 6.1e.

Detailed vehicle design dimensions can be seen in Table 6.1.



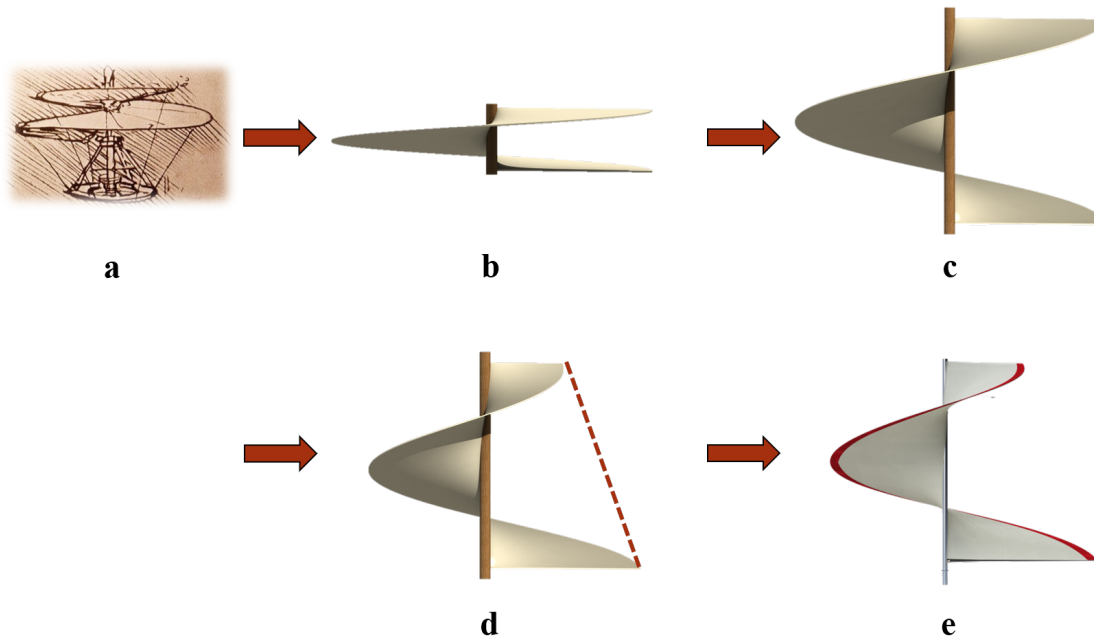
FIGURE 6.1: Design evolution of *Elicó's* aerial screw

TABLE 6.1: Aerial screw detailed dimensions

Parameter	Metric	Imperial
Upper rotor radius	0.725 m	2.4 ft
Lower rotor radius	1.46 m	4.8 ft
Rotor taper	1:2	1:2
Rotor number of turns	1.0	1.0
Rotor height	1.91 m	6.3 ft
Effective rotor area (all rotors)	26.4 m ²	289 ft ²
Distance between adjacent rotors	3.37 m	11.0 ft
Distance of rotor above ground	1.36 m	4.5 ft
Distance (horizontal) of pilot to nearest rotor	0.90 m	2.95 ft
Longest distance from rotor tip to rotor tip	7.65 m	25.1 ft
Distance of cockpit above ground	0.076 m	0.25 ft
Diameter of nacelle in downwash	0.36 m	1.17 ft
Footprint of cockpit	1.21 m ²	13.1 ft ²
Square footprint of rotorcraft	39.5 m ²	425 ft ²
Cubic footprint of rotorcraft	126 m ³	4470 ft ³
Width of truss arms	0.23 m	0.75 ft
Length of truss arms	1.93 m	6.33 ft

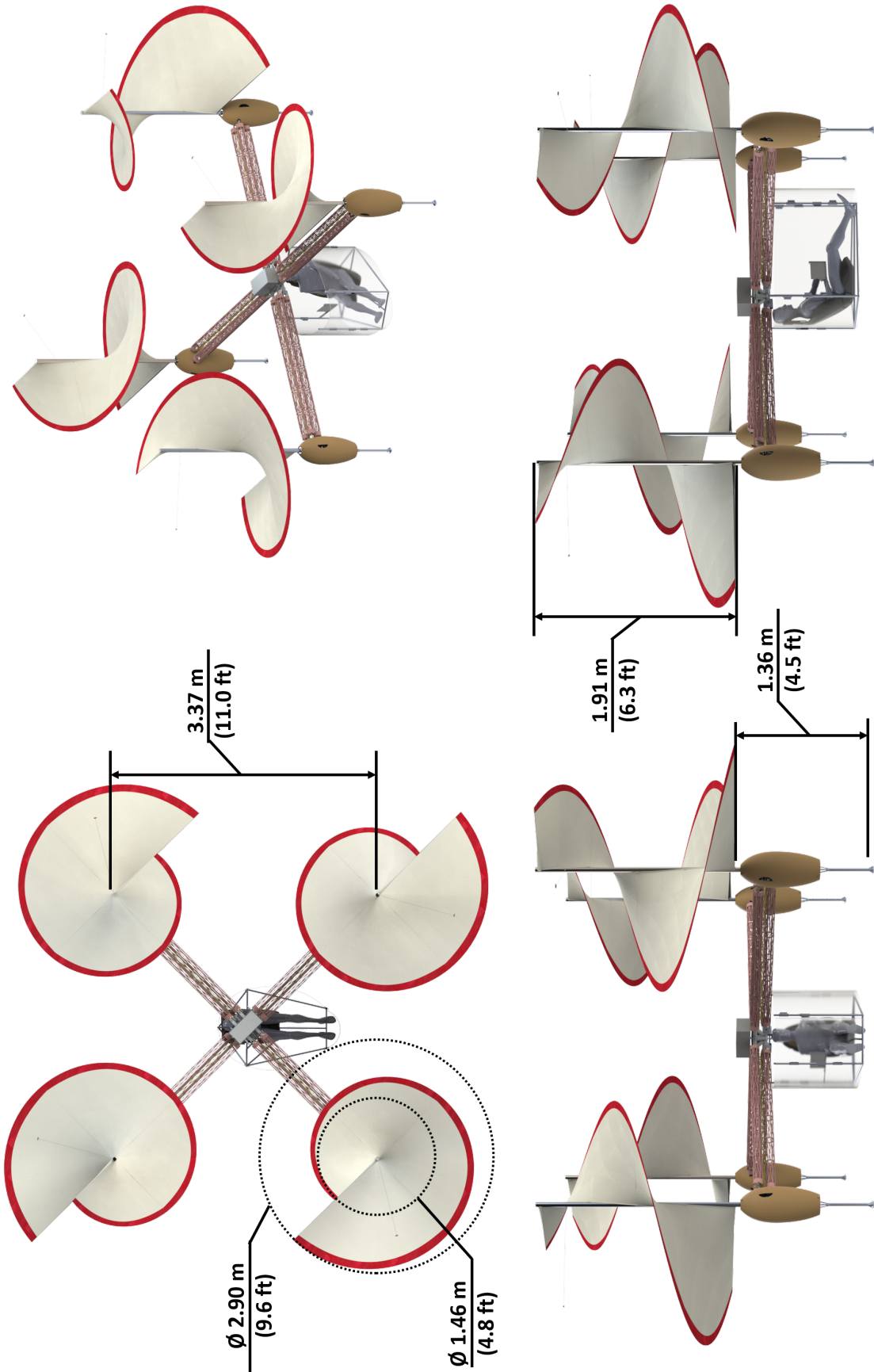
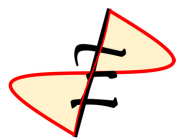


FIGURE 6.2: Overview of *Elico*



7 Rotor Structural Design

The rotor structure is critical to ensuring smooth operation with no mechanical vibrations from a naturally imbalanced rotor, as well as maintaining the helicoid surface of the aerial screw.

This section covers the design, structural analysis, and fabrication of the rotor, which allow for a total rotor weight of less than 3 kg (6.6 lb). The multi-rotor configuration of *Elicor* requires both clockwise and counterclockwise rotors, but due to symmetry they are structurally identical.

The general structure is inspired by Leonardo da Vinci's original design; a central rotating shaft supports several spars that hold up a flexible fabric skin which is impermeable to air. The full rotor with vibration absorber can be seen on the left in Figure 7.1.

The three major components of the rotor are the skin, the spars, and the shaft. The skin is a fabric constituting the main lifting surface of the blade and provides the aerial screw shape, the spars are the main blade structure components within the skin that transfer loads and maintain the shape, the shaft is the central structural component of the rotor transferring all loads to and from the gearbox and vehicle structure. Contrary to traditional rotors the high pitch of the aerial screw means that none of the blade structural elements are in plane. This drives an unusually long shaft which creates the height required for the high pitch aerial screw. Additionally, there are minor structural components that support the shape and allow for the assembly of the rotor. Each component is covered below in detail.

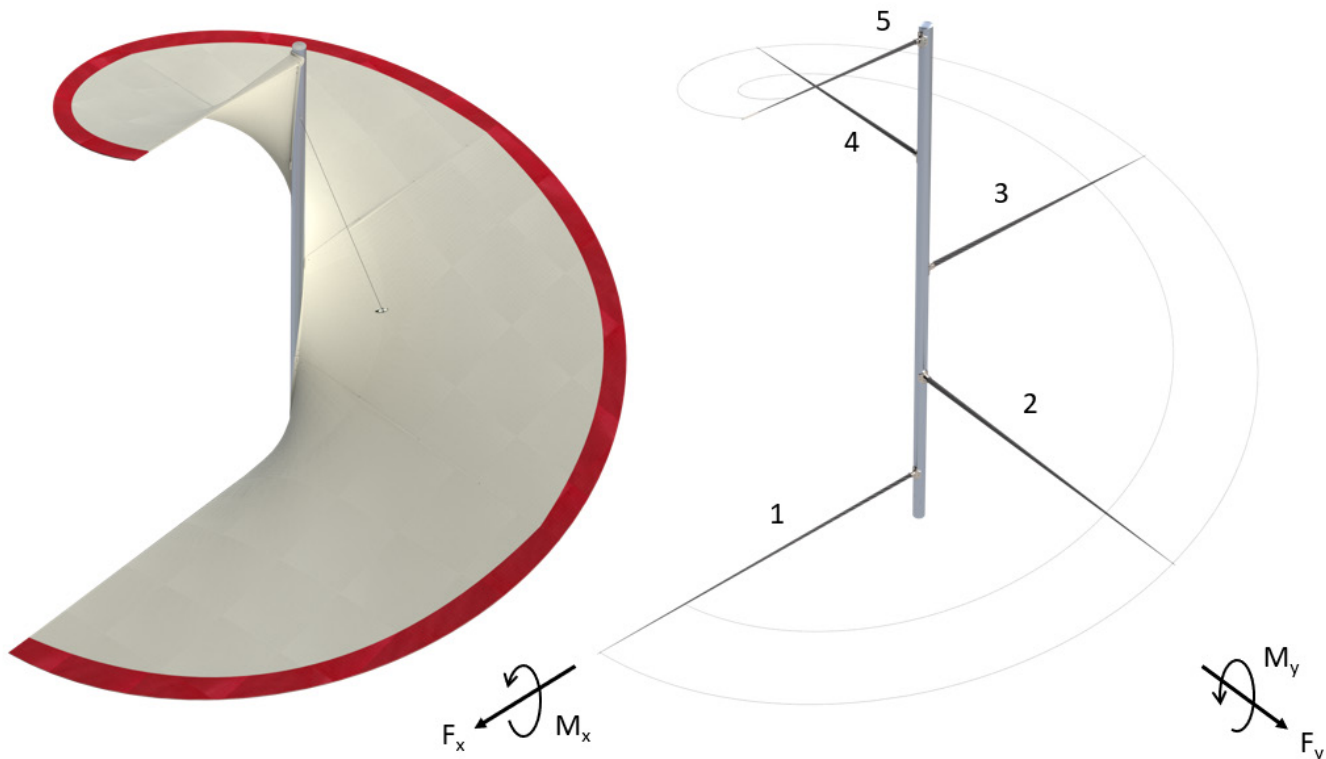


FIGURE 7.1: Overview of *Elicor's* rotor structure

7.1 Rotor Skin

The skin is the main aerodynamic surface of the aerial screw blade and is also the largest part of the rotor. As a result its smoothness is critical and material selection has a large influence on the total rotor weight.

Two skin surfaces cover the structural supports from the top and bottom to prevent the support structures from interrupting the flow, compromising the aerodynamic shape of the aerial screw.

7.1.1 Skin Material

Due to the intrinsically asymmetrical nature of the tapered aerial screw shape, the rotor has a natural mass and aerodynamic load imbalance. The skin was chosen to minimize this imbalance. The rotor has a single side surface area of 4.73 m^2 (50.9 ft^2).

A flexible fabric material was selected for the skin using the following considerations:

- A fabric skin most closely resembles Leonardo da Vinci's original design.
- Fabrics typically have a lower mass per unit surface area compared to metals and composites.
- The complex tapered helicoid surface shape is difficult to manufacture accurately out of a rigid material, but is simple to create with fabrics via tension between skeletal structural components.

The specific material selected is Ripstop 0.75oz Nylon Sailcloth. Sailcloths are designed to be an aerodynamic surface and have been innovated upon for this purpose for centuries. As a result they are guaranteed to have zero porosity, good durability and strength.

Other sailcloth materials were considered such as polyester based fabrics also known as Dacron. Dacron's is resistant to stretching, however due to the small area between rigid support structures (at most 1.71 m^2 (18.4 ft^2)) the importance of stretching is minimized compared to larger unsupported fabric sections. Additionally, some stretch is beneficial for the manufacturing process for tension control and ease of assembly. Furthermore, the fabric will passively conform to the helicoid shape due to centrifugal forces from rotation. Lastly, Ripstop nylon sailcloth is impregnated with melamine which prevents excessive stretching.

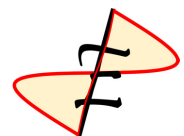
Nylon's advantage over Dacron fabric is its weight. At 31.5 g/m^2 (0.00021 lb/ft^2) it is over 5 times lighter than the lightest Dacron fabrics (168 g/m^2 (0.0344 lb/ft^2)).

7.1.2 Structure Interference Considerations

A challenge of skin design lies in the interaction of the skin with the spars. An ideal aerial screw surface is a helicoid that forms a helix as the intersection with the shaft. This ideal shaft helix intersects the centers of the spars, leading to large disturbances to the shape of the aerial screw surface, compromising the aerodynamic profile. Two skin surfaces, one above and one below the spars limit this disturbance near the rotor tip.

However, near the shaft, the extremely high pitch of the surface-shaft intersection helix results in a large spar intersection despite the vertical offset.

This is resolved with a 30° offset of the intersection helix shown in Figure 7.2. The resulting surface is negligibly different from the ideal helicoid (angles change by less than 1°) and the interference of the spars is minimized.



The skin conforms to the spars at most radial stations along the spars, but separates from the spars near the root. Due to the presence of mounting parts, the larger root spar sections and the attachment of the skin to the shaft, extra clearance from the spar near the root is necessary. As a result the skin mounts directly to the top of the spars from a radius of 300 mm to the tip and deviates slightly from the spar inboard of 300 mm. The 300 mm separation radius was chosen such that the angle of this deviation was minimal while still allowing a large length of direct spar attachment. The resulting angle is 1.65° , negligibly impacting the surface shape.

One possible solution used a segmented intersection helix with a higher pitch to avoid the spar and circular sections to maintain the same average pitch forming a “step” helix. This solution resolved the spar intersection at the root but created a different disturbance in the surface shape near the root.

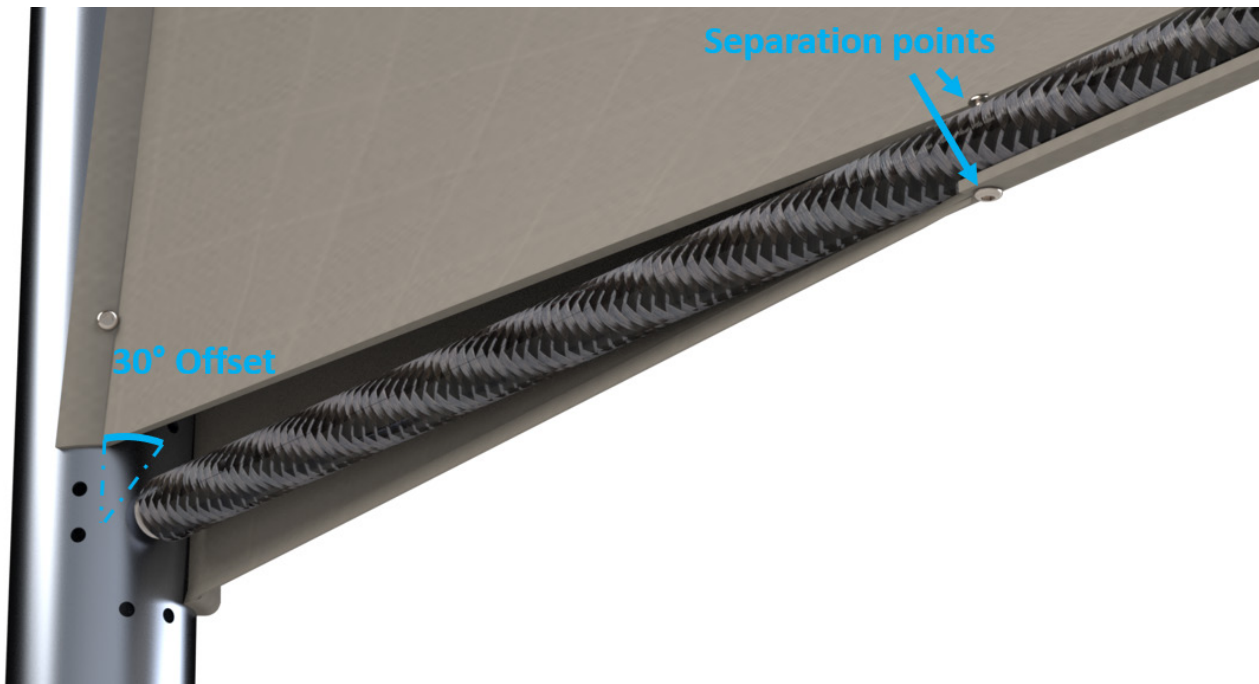


FIGURE 7.2: Image of the spar-skin interference

7.1.3 Skin Attachment

Attachment of the skin to the structure is accomplished with a combination of hardware through mounting points, sealant, and stitching. The loads that the skin transfers through these attachments are discussed in Section 7.2.2.

All of the hardware mounting points pass through a hole in the skin reinforced by a grommet, an example of which can be seen in Figure 7.3. This type of hole mounting is common for sails, and is used reliably on production sailboats.

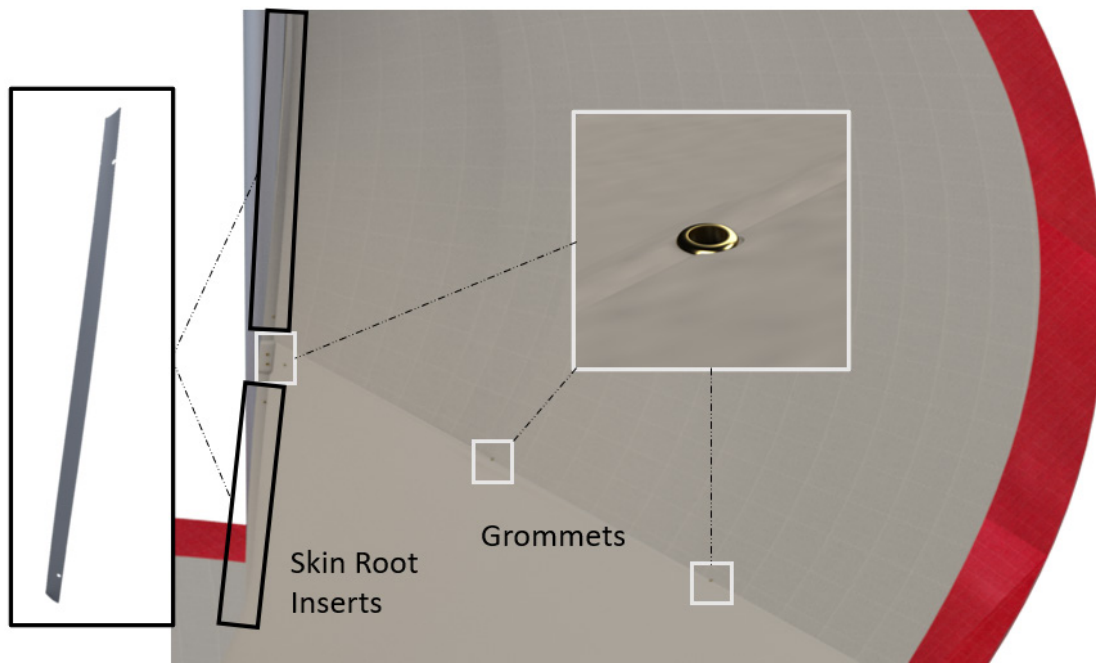


FIGURE 7.3: Embedded features in the skin

The spars and shaft have mounting points that are exclusively for the skin, additional points on the mounting plates are used by the skin to reduce the number of holes in the structure.

Generally M3 screws with low profile heads and nuts are used on the spars, with some M2 and M1 screws near the tip of the rotor where the smaller spar cross sections cannot support M3 screws without compromising structural integrity. M4 screws are used for attachment points on mounting plates.

The shaft attachment is facilitated via a thin aluminum insert shown in Figure 7.3. This insert is embedded inside a flap on the root edge of the skin and creates a rigid section. The root flap is mounted to the shaft and the insert keeps the fabric flush against the shaft, preventing any gaps and leakage of air between the skin and shaft.

The leading edge is formed by wrapping the fabric around the 5th spar, this can be seen on the left in Figure 7.1. Proper attachment here is critical as it prevents any air from entering between the top and bottom skin sections. This would compromise the aerial screw shape and increase drag. The wrap forms an aerodynamic rounded leading edge shape to decrease drag. The connection between the wrap and the shaft is reinforced and made impermeable by sealant to facilitate this.

The cone-like leading edge shape is formed by tension, the various locations that create this tension are indicated in Figure 7.4. The lengthwise tension is supported between hardware mounting points labeled 1, and the points labeled 2 and 3. Some additional root tension is supported by the skin insert shown in Figure 7.3 and is indicated by the green area labeled 4 in Figure 7.4. Transverse tension is supported by the continuation of the fabric to the top and bottom sections indicated by the the red areas labeled 5, with additional support from the skin insert labeled 4. The wrap further towards the tip is flush against the round spar. The described tension alone creates a pyramidal shape.

A small plastic insert is used to round out the leading edge, it is shown in Figures 7.6 and 7.5. This insert forms the blue edge labeled 6 in Figure 7.4 and provides attachment point 3. The insert is attached

to the structure via the mounting plate through the two counter-bored holes. The skin attaches to the insert via the hole with an embedded nut.

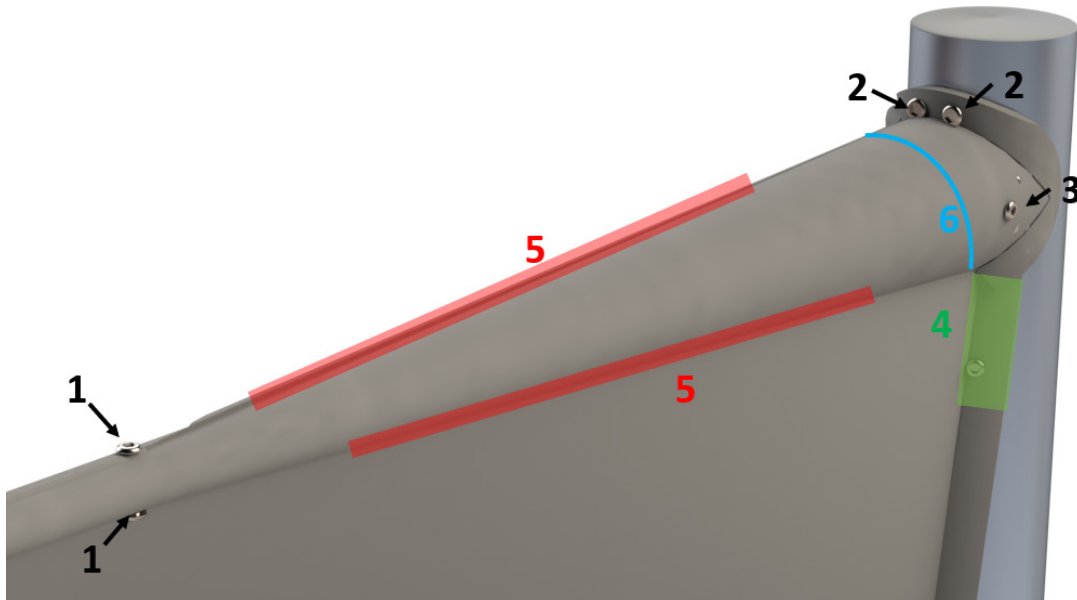


FIGURE 7.4: The leading edge wrap with labeled tension bearing locations

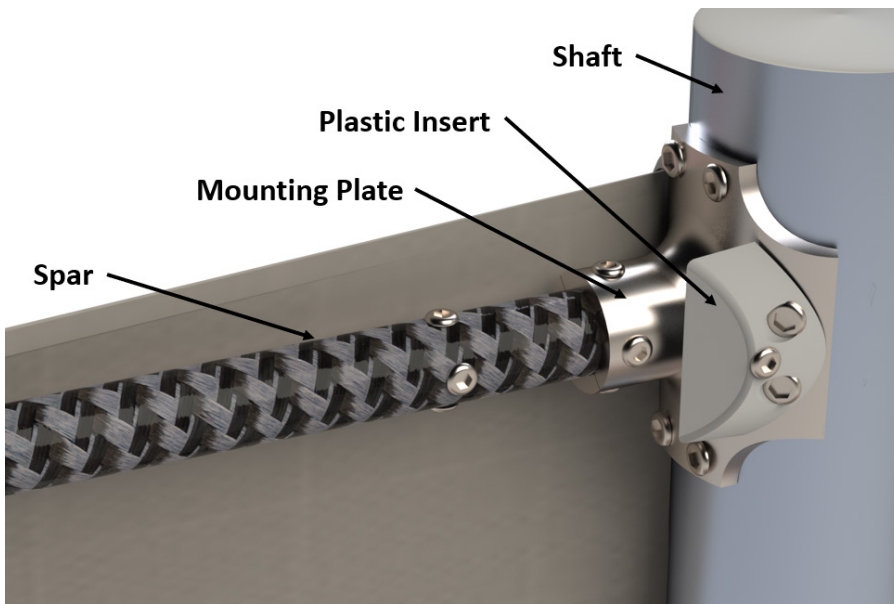


FIGURE 7.5: The plastic insert mounted to the structure

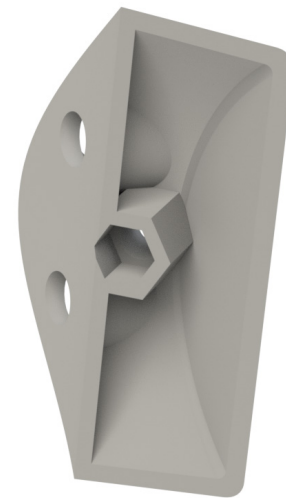
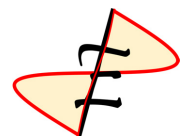


FIGURE 7.6: Backside view of the insert in isolation

Stitching is used to attach the skin to thin carbon fiber helical supports. These supports are too thin to support hardware and will not bear large loads. The outer helix keeps the tip of the rotor in a helical shape, preventing straight edges created by tension between the tips of the spars. The inner helix support is located at 75% radius and serves to add additional support for the shape.



7.2 Spars

Five spars are positioned every 90 degrees around the aerial screw and can be seen in on the right in Figure 7.1 along with the support helices. Each spar has a unique length to match the 1:2 radius taper of the overall aerial screw as well as a unique cross-sectional taper to maintain a constant factor of safety (FOS) along its length. The spars have holes every 300 mm to facilitate the mounting of the skin. These holes are 3 mm in diameter with the exception of some near the tip where the smaller cross-section drives a smaller mounting hole size.

7.2.1 Number of Spars

The number of spars was based on two factors. Fewer spars would have caused the angle between spars to exceed 90 degrees. This causes the outer ring to support high tensile loads in the form of tension and a helicoid surface shape may not be guaranteed. A configuration with more than five spars was analyzed and the trend in weight with respect to number of spars can be seen in Figure 7.7. Increasing the number of spars increases the weight and provides relatively little benefit to the shape. It should be noted that the attachment components necessary to mount the spar to the shaft are not included in this analysis, and would further increase the weight.

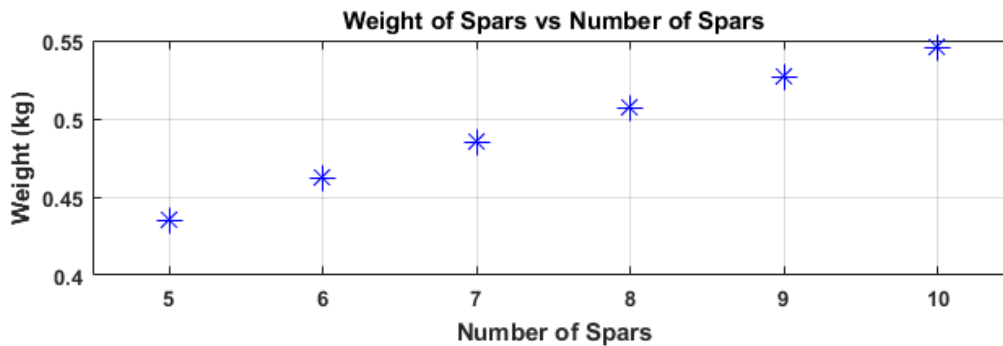


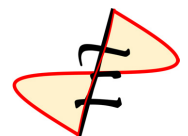
FIGURE 7.7: Weight of all spars increases with increasing number of spars

7.2.2 Spar Loads

A critical part of spar sizing is the estimation of the loads on each spar. These consist of distributed bending loads from lift and drag in the vertical and horizontal directions respectively, as well as axial loads due to centrifugal forces.

The centrifugal forces arise from the weight of the skin and the spars themselves. As part of the sizing process the spars are split into 500 segments, each segment has a cross-sectional area, elemental length, and a distance from the axis of rotation. Using the structural mass density and the operating RPM the distribution of centrifugal forces due to spar weight is calculated. The centrifugal forces from the skin are not straightforward to calculate and some conservative assumptions are applied. At each radial section the assumed skin mass contributing to centrifugal forces is calculated using Equation 7.1 where m is the mass per surface area, p is the pitch, and r is the radial station. This conservatively assumes that each spar carries one fourth of the skin weight despite the fact that there are 5 spars.

$$2(1/4)\sqrt{(2\pi r)^2 + p^2}dm \quad (7.1)$$



The airloads are also complex to estimate and was approached with an iterative method that is based on Computational Fluid Dynamics (CFD) results discussed in Chapter 3. This approach allows for a reasonably good approximation of the lift and drag distribution on each spar labeled $i \in [1, 2, 3, 4, 5]$ depicted on the right in Figure 7.1, where 1 is the lowest and largest spar and 5 is the topmost and shortest spar. All of the aerodynamic loads are assumed to be carried by the spars only, conservatively ignoring the load path directly into the shaft via the skin shaft connection.

The shape of the lift distributions is based on the surface pressure plots determined with CFD analysis, shown in Figure 3.8, accounting for forces that occur on the skin in between the spars. These distributions are approximated by a Gaussian curve with a mean μ_i and standard deviation σ_i for each spar.

The scaling factor s_i for the lift distribution of spar i is found using:

$$s_i = \frac{Tw_i}{\left(\sum_{n=1}^5 w_n\right) \int_{r_{shaft}}^{R_i} \frac{1}{\sigma_i} \varphi\left(\frac{x - \mu_i}{\sigma_i}\right) dx} \quad (7.2)$$

where w_i is the weighing factor assigned to a spar i , r_{shaft} is the shaft radius, R_i is the length of spar i , and φ is the probability density function of the standard normal distribution. The result is a configurable weight for each lift distribution that ensures that the total lift matches the total thrust of the rotor. These weights are the first set of tuneable parameters.

The second set of tuneable parameters is the drag scaling factor. Here the drag is assumed to be directly proportional to the lift, and therefore has the same distribution. Each spar has a drag scaling factor that gives the drag magnitude.

Both sets of tuneable parameters are first assumed based on the pressure distribution plots, then the total aerodynamic loads are calculated and the weights are tuned such that the calculated loads match the CFD scale result for validation. The results are shown in Table 7.1, with forces defined in Figure 7.1. The same weights are then applied for the vehicle scale case.

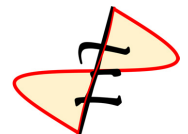
This methodology results in the aerodynamic force distributions shown in Figure 7.8. Note that, the lift on the leading edge (5) and trailing edge (1) spars is reduced due to the circulation of flow from the top to the bottom surface at those edges. The drag on those spars remains relatively large due to the incidence and wake flow. The drag on spars 5, 4 and 3 is large due to the strong attached vortex present in the upper half turn of the screw. The lift on spar 2 is disproportionately larger than the drag due to the large area and detaching vortex in that region.

TABLE 7.1: Validation of calculated with CFD aerodynamic loads (10 ft radius case)

Method	\mathbf{F}_x N (lb)	\mathbf{F}_y N (lb)	\mathbf{M}_x Nm (lb-ft)	\mathbf{M}_y Nm (lb-ft)
CFD	173 (39)	-881 (-198)	5253 (3874)	-1912 (-1410)
Calculated	252 (56)	-738 (-166)	5288 (3900)	-2021 (-1490)

7.2.3 Spar Sizing

The spar cross section is a hollow circular tube with a thickness to radius ratio of 0.2. This ratio is chosen subject to two constraints. The upper constraint is weight: a lower t/r ratio leads to lighter



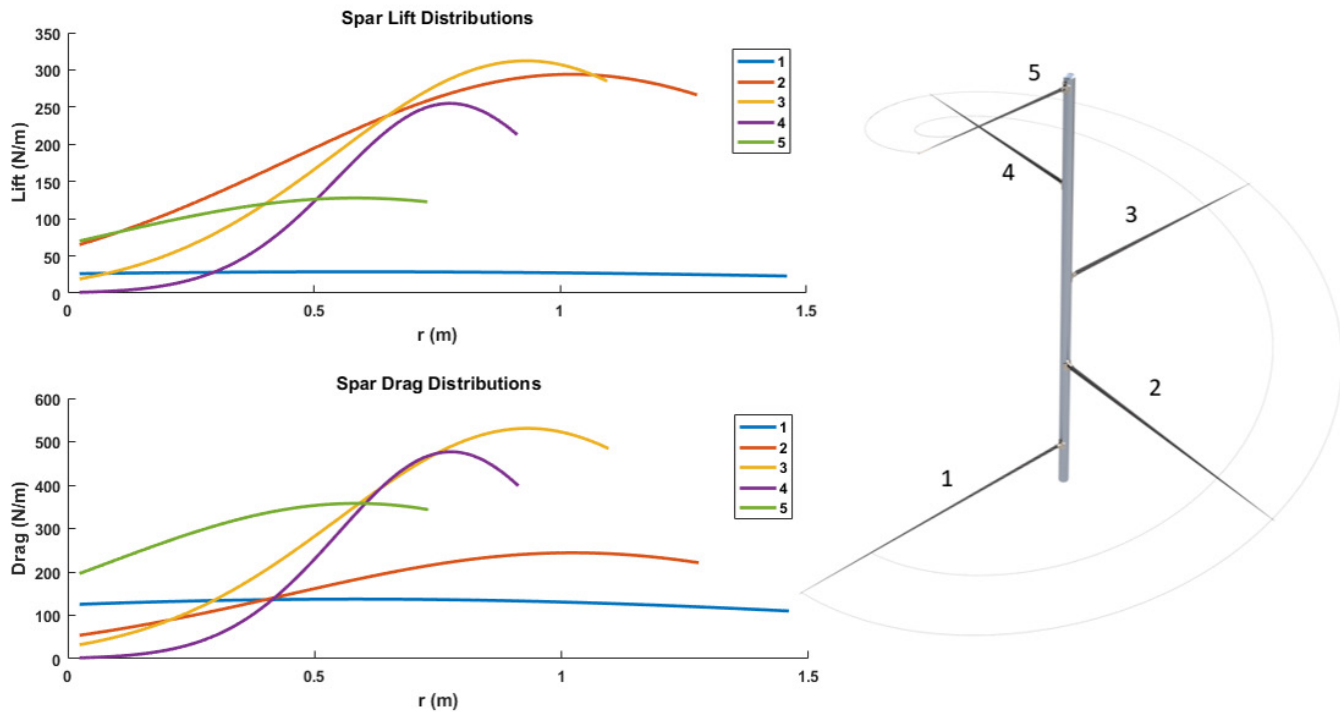


FIGURE 7.8: Lift and drag distributions over each spar

overall spars, where t is the thickness of the cross section and r is the outer radius. The lower constraint is minimizing r for reduced spar-skin interference and risk of buckling. Smaller spars also decrease the weight of the mounting pieces. Figure 7.9 displays the relationship between weight and thickness ratio t/r . A t/r of 0.2 results in a small size spar with minimal weight penalty and no risk of buckling failure.

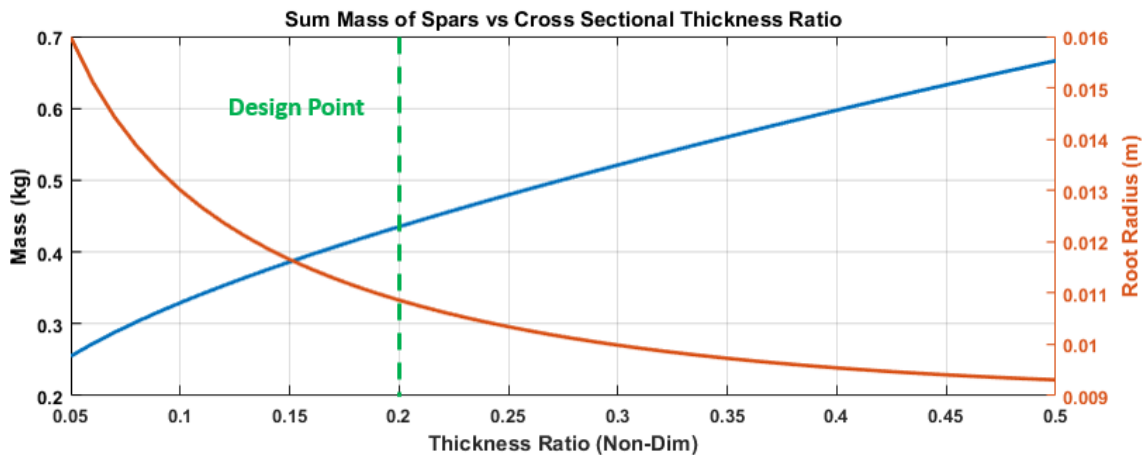
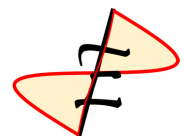


FIGURE 7.9: The relationship of spar thickness ratio to root radius with the design point shown

Each spar’s cross-sectional taper is determined via an iterative procedure such that a factor of safety of 3 is present at the point of maximum stress along the entire length. Each successive iteration uses the previous iteration’s taper in centrifugal force calculations until the spar weight does not change between



iterations. The resulting taper of each spar is depicted in Figure 7.10. Practically, the minimum radius is 1 mm (0.04 in) at the tip.

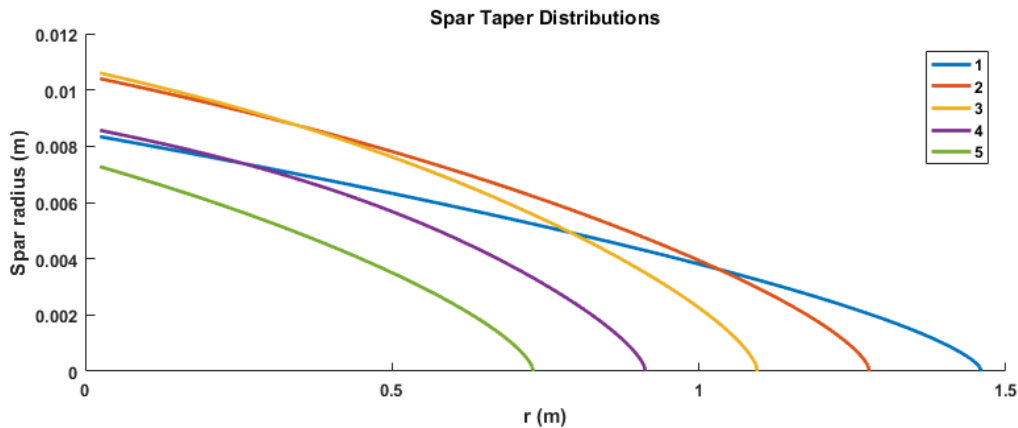


FIGURE 7.10: Designed spar taper distributions

7.2.4 Spar Material

The spar material is a $[0, 90, 0]^\circ$ carbon fiber epoxy composite layup with a tensile strength of 1.5 GPa and elastic modulus of 159 GPa in the axial direction.

An aluminum material was also considered, but was not chosen due to the higher strength to weight ratio of carbon fiber. Because the spar is subjected to only axial stress from axial and bending loads a designed layup material minimizes the total weight.

7.2.5 Spar Finite Element Analysis

To validate the analytical result a Finite Element Analysis (FEA) was performed using Solidworks Simulation on the spars, shown in Figure 7.11. FEA validates the factor of safety set for the spar of 3, and confirms that the stress concentrations around mounting holes will not lead to material failure. This study applied the centrifugal, lift, and drag forces described in Section 7.2.2 and conservatively did not include the support helices or skin.

It should be noted that the factor of safety (FOS) is defined with respect to yield strength for metals and ultimate strength for composites in both analytical and FEA results. FEA calculates general Von Mises stresses, whereas the principle stresses are used in the analytical approach.

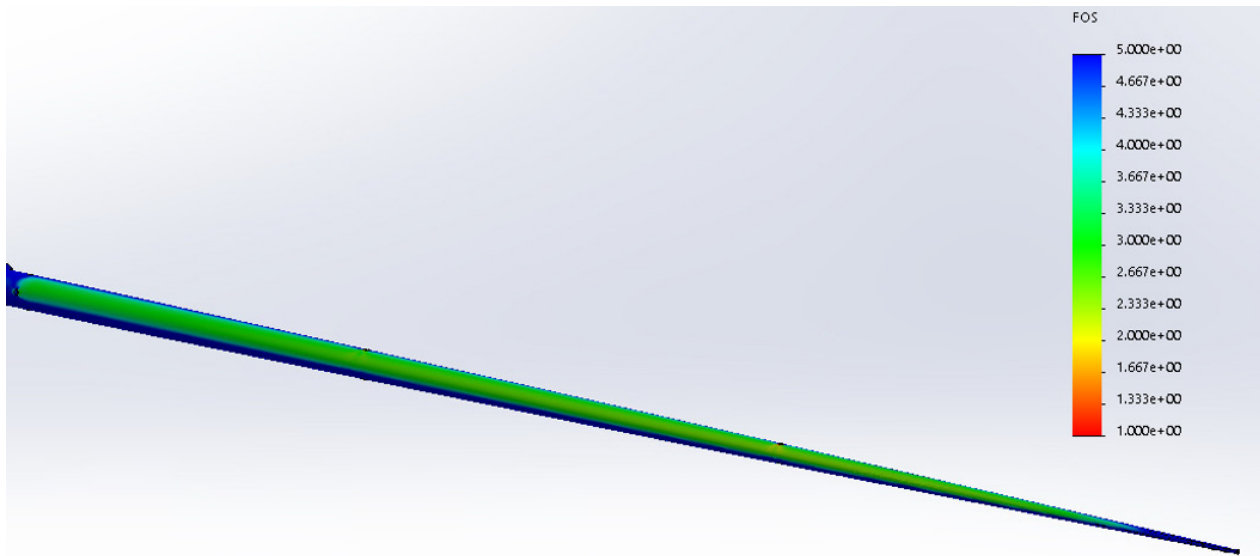


FIGURE 7.11: FEA result for a spar

7.3 Rotor Shaft

The rotor shaft is a flight critical component responsible for transferring all rotor loads to the gearbox system. For analysis the gearbox system is assumed to apply a cantilever condition to the end of the shaft; this is a conservative assumption that leads to higher loads at the root of the shaft.

7.3.1 Shaft Loads

The loads on the shaft are derived from the loads already described in Section 7.2. Additionally, the rotor torque is assumed to be applied over the entire length of the shaft, this assumption is conservative because the full torque only acts on the section between the support and the lowest spar. Also, the same centrifugal force analysis is used, leading to loads that account for a skin weight 25% larger than the real weight.

The unbalanced loads at the base of the shaft in the rotating frame are tabulated in Table 7.2, these include both aerodynamic and centrifugal loads. As before the forces in Table 7.2 are defined in Figure 7.1. These loads drove the shaft sizing, conservatively not accounting for balancing measures described in Section 7.4.

TABLE 7.2: 1/rev Loads at the Base of the Shaft in the Rotating Frame

Thrust N (lb)	F_x N (lb)	F_y N (lb)	Torque Nm ($lb-ft$)	M_x Nm ($lb-ft$)	M_y Nm ($lb-ft$)
686.7 (154.4)	63.6 (14.3)	-14.6 (-3.3)	330 (243.4)	292.4 (215.7)	-175.5 (-129.4)

7.3.2 Shaft Sizing

The shaft cross section is a hollow circular tube. The outer radius was set and the thickness was calculated such that the shaft has a factor of safety of 3. The shaft FOS is the minimum of those with respect to principle shear and axial stresses and respective strengths. Principle stresses were calculated with Mohr's circle method accounting for axial, bending, and torsional loads.

A FOS of 3 is used because the shaft is a mission critical component and stress concentrations around mounting points are not included.

The outer radius choice is subject to constraints above and below. It is constrained from above by buckling risk, and from below by strength, weight, and geometric considerations for spar-skin interference and mounting.

7.3.3 Shaft Material

The shaft material is aluminum 7075-T6, chosen for its high shear and tensile strength and low mass density. The outer radius is 2.4 cm with a wall thickness of 1.33 mm.

An alternative was a carbon fiber shaft with custom layup designed for the combined shear and axial loads of the shaft. Despite resulting in a lighter shaft, this $[45, -45, 0, 90, 45, -45]_s$ layup was not chosen due to practical issues. Primarily, there was an issue with mounting the spars without compromising structural integrity due to the nature of carbon fiber composites. Additionally, the range of acceptable shaft radii and thicknesses proved geometrically incompatible with skin mounting.

The comparison of shaft weight and wall thickness with varying outer radius and material can be seen in Figure 7.12.

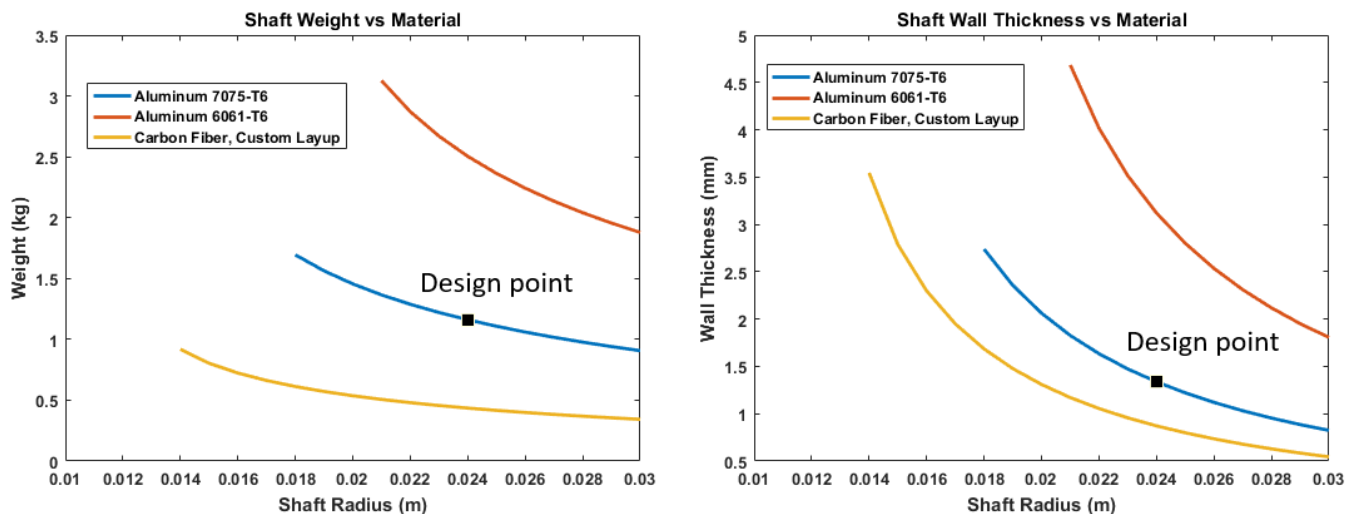


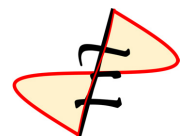
FIGURE 7.12: Shaft weight and wall thickness with varying outer radius and material

7.4 Vibration Absorber

Without a vibration absorber system the rotor would deflect by 4.17 degrees about the arm at 1/rev, causing a 0.305 m (12 in) vibratory amplitude at the top of the aerial screw. This problem is solved in *Elenco* with a vibration absorber that makes the deflections negligible and only increases the total rotor weight by 112.2 g (3.95 oz).

This vibration was a challenge in experimental testing and is a possible reason why no full scale aerial screws have been successfully designed and built.

The cause of vibrations and mechanism of the solution are shown in Figure 7.13. The aerial screw has a center of pressure that is not aligned with the rotation axis, this combined with the mass imbalance



of the rotor creates a bending moment on the shaft in the rotating frame, shown in blue. When this moment is translated into the fixed frame, it rotates at $1/\text{rev}$ with the rotor and creates an oscillatory twisting moment on the arm structure that supports the rotor and nacelle. The twisting of the arm deflects the nacelle and rotor from the upright orientation by an angle Θ .

The forcing moment comes from the same forces as those described in Section 7.2.2. It is similar to the moment detailed in Table 7.2 except calculated about the arm neutral axis, depicted as a black dashed line in Figure 7.13, rather than shaft base. It should be noted that due to the high bending stiffness of the arm, described in Section 8.2, the bending deflection of the arm from this moment as well as rotor side forces is negligible.

To counteract these vibrations a weight is used to create a centrifugal force that creates a moment about the arm equal and opposite to the forcing moment, shown in green in Figure 7.13.

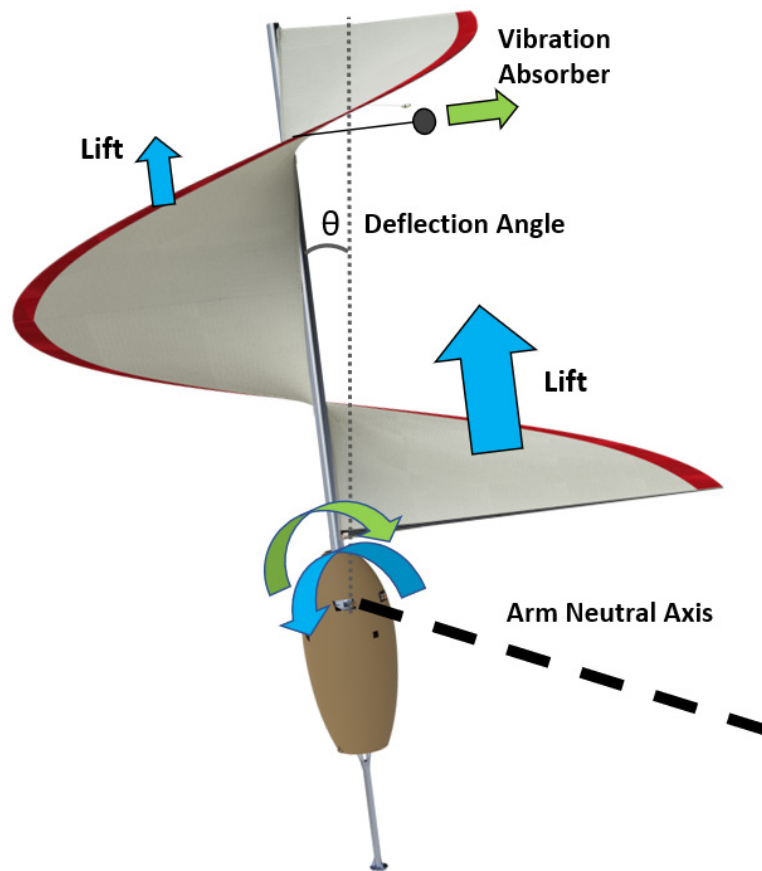


FIGURE 7.13: Diagram of the forces and deflection relating to $1/\text{rev}$ vibration of the aerial screw

As seen in Figure 7.14, a $[0, 90, 0]^\circ$ solid circular carbon fiber epoxy rod of diameter 1.5 mm (0.06 in) weighing 3 g (0.1 oz) is attached to the shaft with a small Polylactic Acid (PLA) plastic part at a point 250 mm (9.84 in) below and 30.12° ahead of the topmost spar. This rod supports a 108.8 g (3.84 oz) aerodynamically shaped tungsten weight at a distance of 1 m (39.37 in) from the axis of rotation. The tungsten weight is epoxied into a circular receptacle on the end of the rod. The centrifugal force created by the tungsten weight results in a 321 Nm (237 ft-lb) moment about the neutral axis of the arm that cancels the forcing moment.

The rod has a factor of safety of 12 for combined gravitational and centrifugal forces and was placed away from the aerial screw vortex to have a negligible aerodynamic effect. At the operating RPM, the tungsten weight at the tip will deflect down by 6.6 mm (0.26 in). The plastic root part does not allow the carbon fiber rod to contact the aluminum, preventing galvanic corrosion.

The assembly was analyzed with FEA, shown in Figure 7.15, to properly size the plastic root and confirm there are no issues at the tungsten weight attachment. The minimum factor of safety is 1.5 at a small stress concentration in the plastic part, which has a FOS of 2.5 for the overall structure. The FOS at the tungsten weight attachment location is 4.5 and the study confirms the overall FOS of the rod of 12.

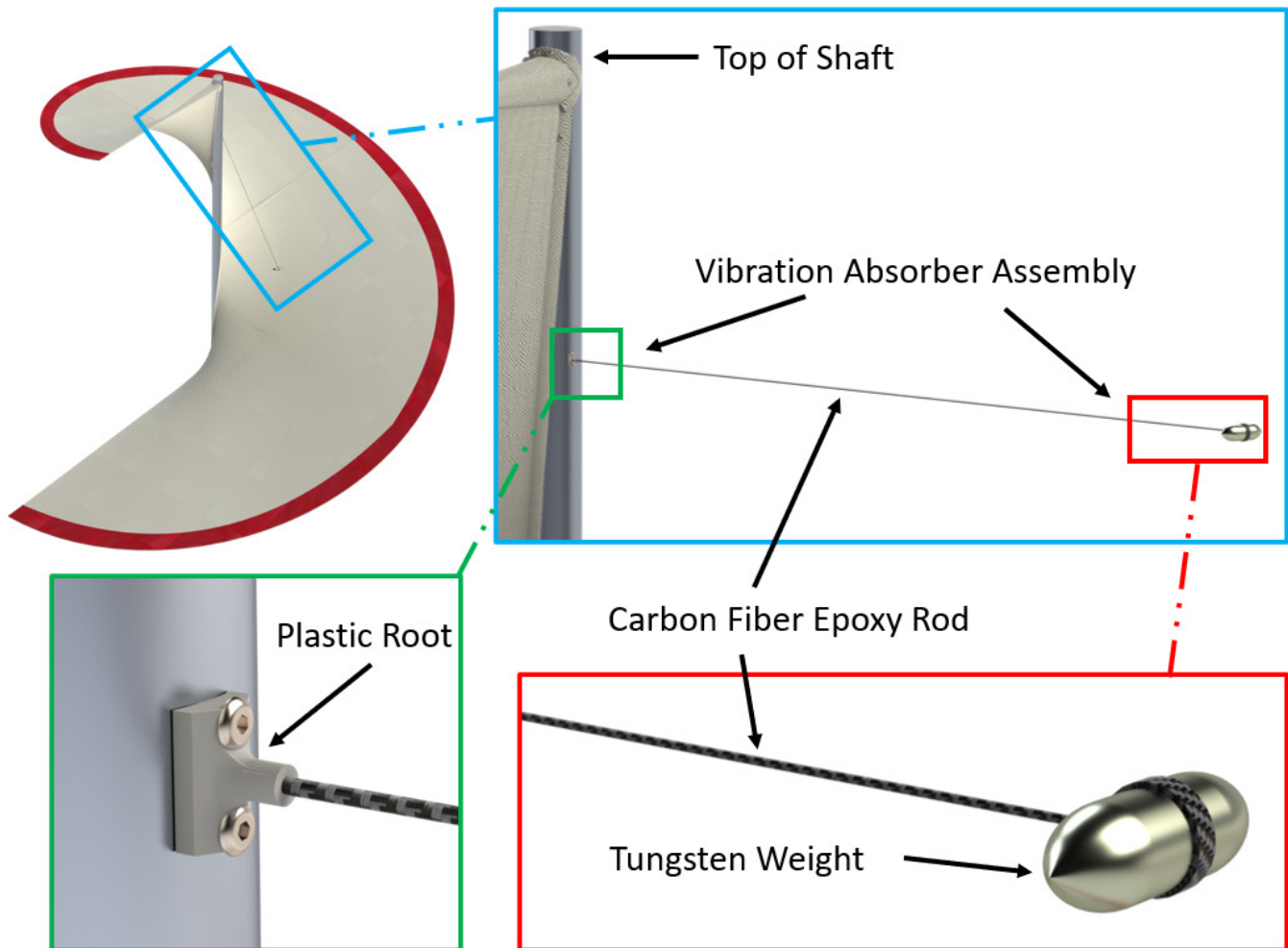


FIGURE 7.14: The vibration absorber assembly

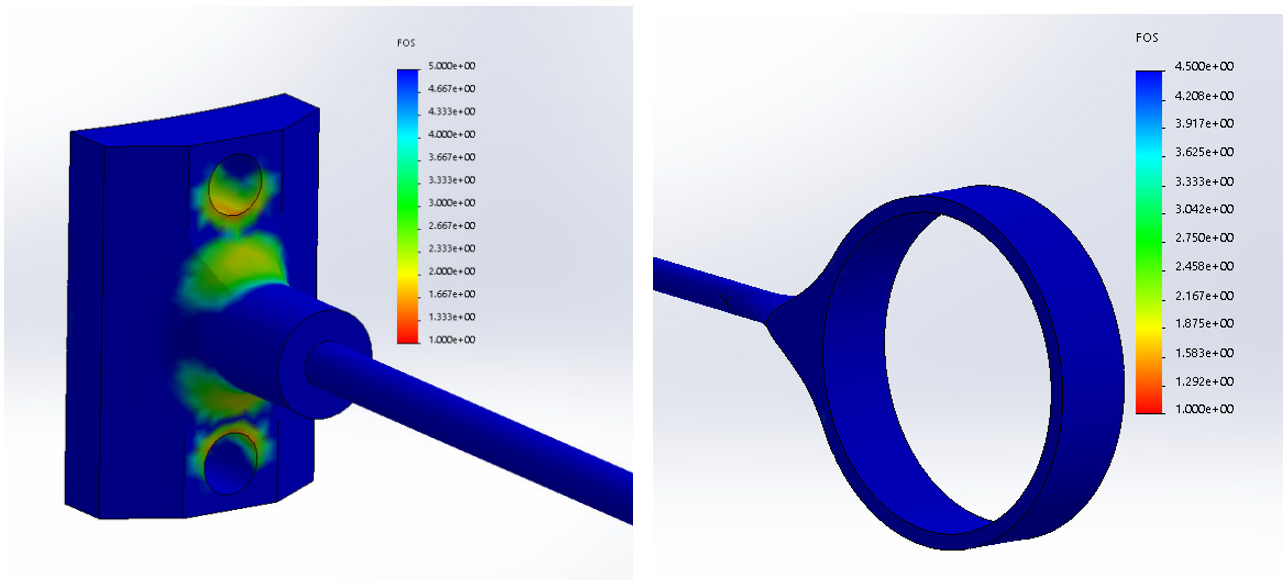


FIGURE 7.15: FEA study for vibration absorber attachments

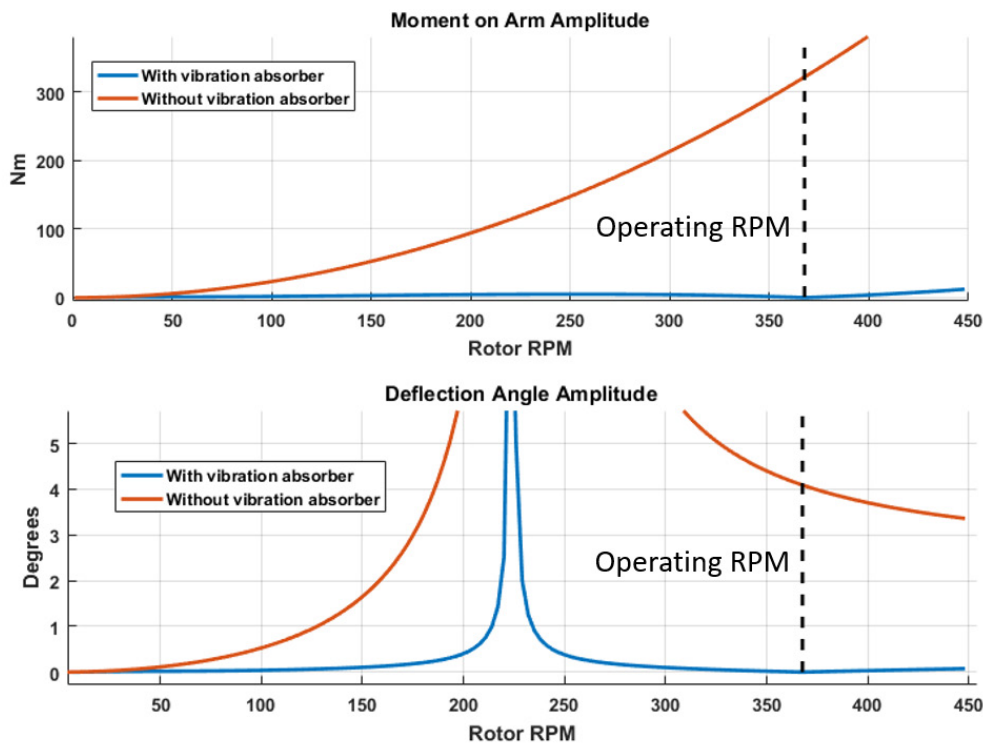
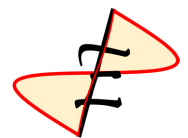


FIGURE 7.16: 1/rev rotor moment and arm twist deflection amplitude vs RPM

The aerial screw speed will not always be at the operating RPM due to both start-up procedure and RPM modulation for control. As a result the effect of the vibration absorber at a range of rotor RPM was investigated.

Figure 7.16 shows the effect of the vibration absorber on both the total 1/rev moment and the 1/rev deflection angle. The moment amplitude is drastically reduced, with a local peak of 5 Nm (3.69 ft-lb)



at 253 RPM. The deflections are lowered to under 0.3° at all RPM except the structural resonance range. The vibration absorber narrows the critical resonance RPM range to 193-256, minimizing risk during spin-up. It is worth noting that while the vibration absorber completely negates the moment imbalance, it does increase the total side force from 65 N (14.6 lb) to 155 N (34.8 lb). However, because of the high bending strength of the cellular truss, as discussed in Section 8.2, these are easily carried by the structure.

7.5 Attachments

The mounting components used to attach the spars to the shaft, the shaft to the vehicle and provide support of the skin are critical to the structure and transfer of loads. They can be seen in Figure 7.17 the investigation of their performance with FEA can be seen in Figures 7.18 and 7.19.

7.5.1 Spar Mounting Assembly

A mounting plate and spar insert are used to attach each spar to the shaft. These parts can be seen individually and assembled in Figure 7.17.

The mounting plate is the main mechanism of load transfer. A threaded area accepts the spar insert on the face of the mounting plate and an extrusion supports the spar from the outside.

The spar insert is a metal component epoxied into the spar root with a male thread for attachment into the mounting plate, and 8 female threads for accepting mounting hardware that supports the spar. This insert reinforces the root of the spar preventing buckling and accepts bending moment loads.

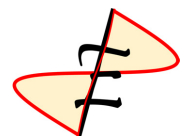
7.5.2 Support Helix

As seen in Figure 7.17, two support helix structures are used in the rotor design, the outer helix is positioned at the rotor tip and inner helix is positioned at 75% radius. The outer helix supports skin tension to maintain the aerial screw shape near the tip. Both helices add rigidity to the spars and are directly sown to the skin fabric.

The inner helix passes through holes in the spars, whereas the outer helix has bulbs with holes that the spars pass through. These connections are all reinforced with epoxy.

7.5.3 Shaft Mounting Assembly

The shaft is created with gearing on the bottom inside edge for torque transfer from the gearbox. A lift collar is used to transfer the lift to the structure and is bolted into the shaft the same way the mounting plates are, also with M4 bolts. These parts can be seen in Figure 7.17.



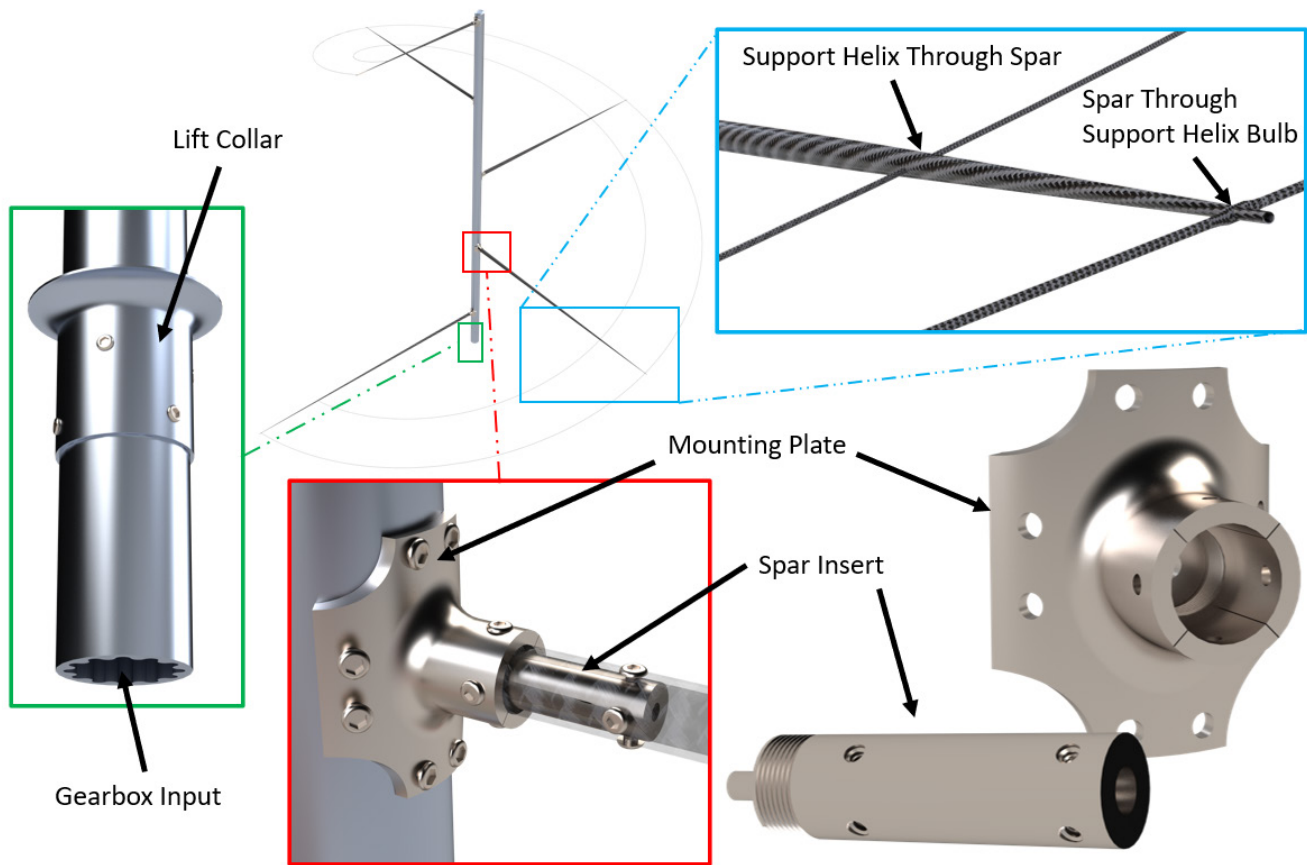


FIGURE 7.17: Summary of rotor attachment components

7.5.4 Attachment Materials

The material chosen for the spar mounting plate and insert parts is a titanium alloy Ti-6Al-4V. An important consideration for these parts is galvanic corrosion due to the presence of carbon fiber spars and aluminum shaft.

Duranickel alloy material was considered due to its machinability but excluded due to low strength. FEA analysis was conducted with Duranickel and determined that the Duranickel parts would fail.

This prompted an adjustment to increase part thickness and the switch to the titanium alloy. As shown in Figure 7.18, FEA on the reinforced part shows no failures. In general the factor of safety is between 2 and 6 with small areas around 1.2 at locations of stress concentrations.

The support helix material is a carbon fiber epoxy composite for its high specific stiffness. Due to the constraint of a small profile and high stiffness no other materials were found to be suitable. Additionally, carbon fiber helix structures will have a strong epoxy bond to the carbon fiber spars which allows for a minimal profile.

The lift collar is made from the same material as the shaft, aluminum 7075-T6, due to its high strength to weight ratio. FEA was performed to verify that the collar is sufficiently strong and that no issues from the mounting holes to the shaft would occur. As shown in Figure 7.19, the entire collar has a factor of safety of more than 5. And the stress concentrations near the mounting holes from both the torque and thrust are not large enough to cause failure, maintaining a FOS of over 2.

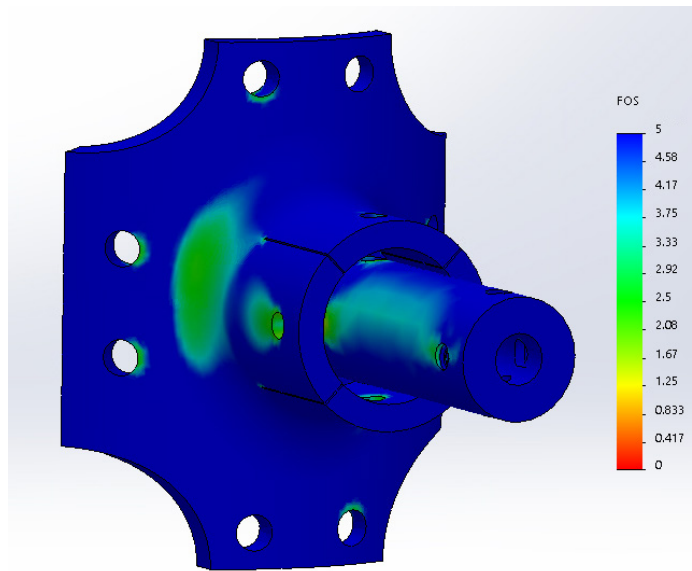


FIGURE 7.18: Factor of safety plots of the spar mounting parts

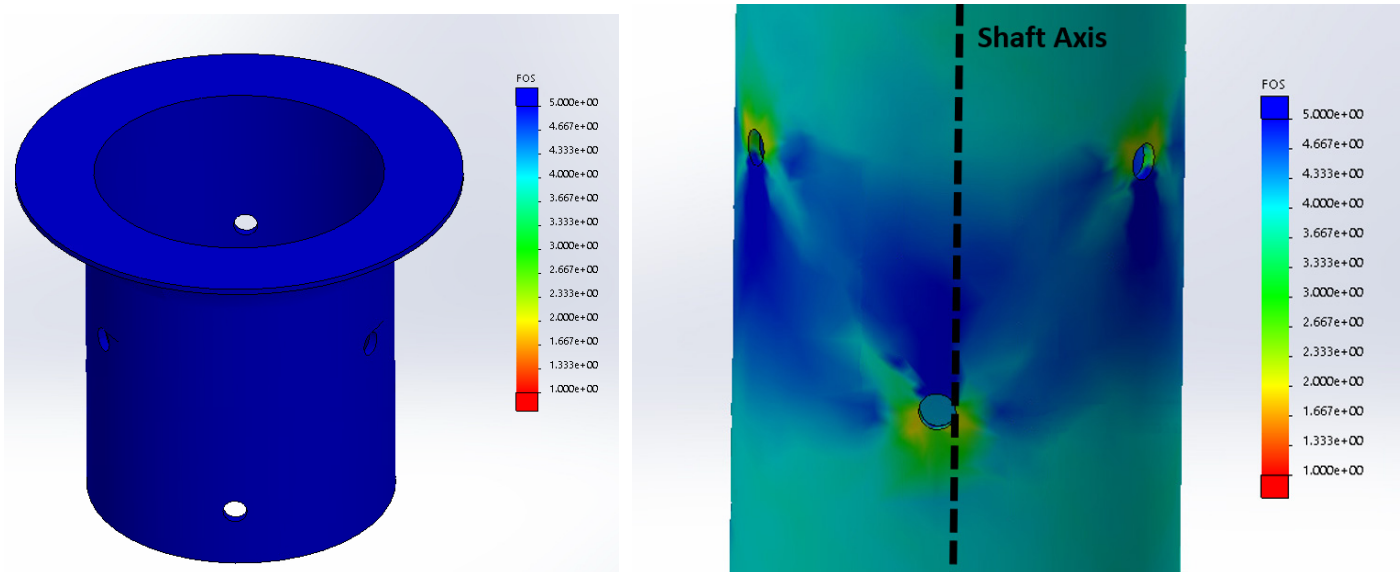


FIGURE 7.19: FEA results on the lift collar and corresponding mounting holes on the shaft

7.6 Aerial Screw Fabrication

The shaft is made of extruded aluminum, the gear teeth are created by gear hobbing. The leading edge insert is 3D printed out of PLA and sanded for a smooth finish.

The spars are manufactured on a specialized mandrel with fiber placement techniques and then cured. Mounting holes for the spar insert, skin attachment points and inner helix are drilled. The inner and outer support helices are likewise made on specialized mandrels with fiber placement and allowed to cure.

The spar inserts are machined on a lathe, the mounting plates are machined on a CNC machine.

The counter-balance rod is made with fiber placement, the root support is 3D printed out of PLA and the tungsten weight is machined on a lathe.

The skin is made in sections out of the Ripstop fabric and the top and bottom are stitched together at the leading edge wrap. The holes are punched and reinforced with grommets, and the root insert is embedded into the root flap.

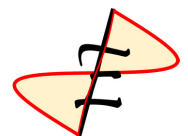
The assembly process starts by fixing the mounting plates to the shaft. A specialized nut with a rounded edge is held on the inside of the shaft by a long tool, only the mounting points exclusive to the plates are attached now. The spar inserts are epoxied into the spars and then screwed into the mounting plates, then the spar is bolted to the mounting plate and insert. The leading edge insert is attached. Then, the inner and outer helices are epoxied to the spars. The skin is then fastened through the mounting plates first, then the inserts to the shaft. The skin is then pulled taut and fastened to the spars radially outwards. The outside seam is stitched closed with a zig-zag stitch past the outer helix. Finally, the counter-balance is epoxied into the rod that supports it, and the rod root is epoxied into the plastic root part. The counter balance is bolted to the shaft as the last step.

7.7 Rotor Weight Breakdown

The overall mass of each rotor is 2.792 kg (6.15 lb). This low weight is facilitated by hollow cross section members, sizing to a factor of safety of 3, a lightweight vibration absorber and careful material selection. The breakdown can be seen in Table 7.3.

TABLE 7.3: Weight breakdown of a rotor

Component	g	oz
Shaft	1223	43.14
Spars	372	13.12
Skin	352	12.42
Mounting Plates	275	9.70
Spar Inserts	146	5.15
Counter-Balance	109	3.84
Hardware	108	3.81
Support Helices	66	2.33
Collar	56	1.98
Shaft Cover	4.4	0.156
Counter-Balance Rod	3.0	0.104
Grommets	1.6	0.056
LE Insert	1.0	0.035
Counter-Balance Rod Root	0.95	0.034
Total	2792	98.47



8 Airframe Design

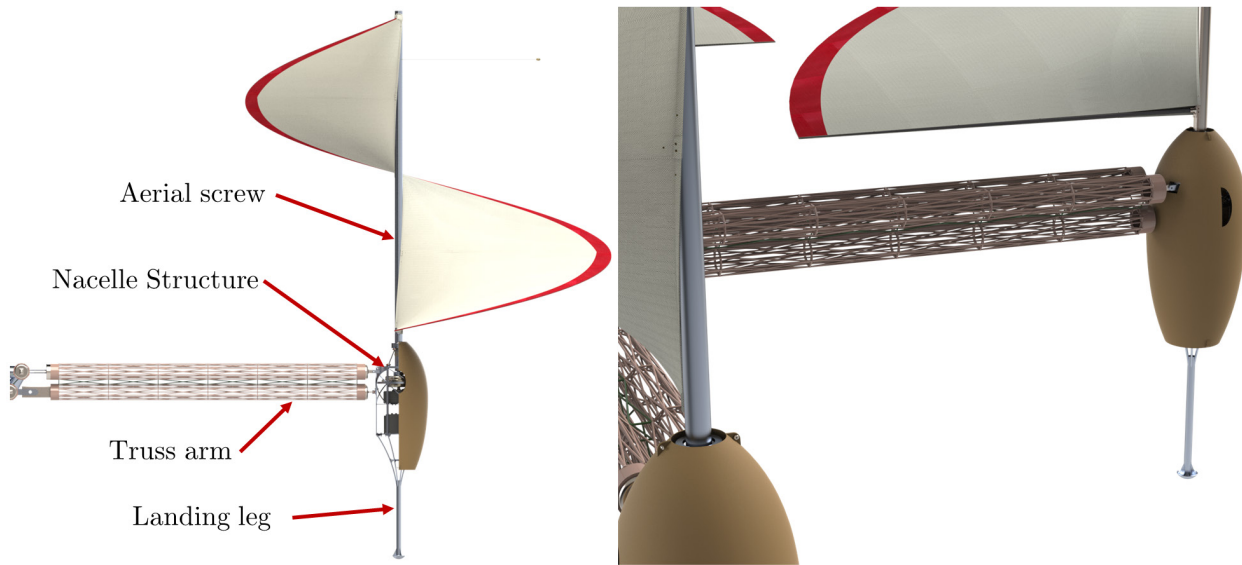


FIGURE 8.1: Rotor, nacelle and arm connections

8.1 Nacelle and Drivetrain Structure

The primary objectives of the nacelle structure for *Elico*, as seen in Figure 8.2, were to house drivetrain components and to transfer loads effectively from the rotor to the vehicle arms and landing legs as seen in Figure 8.1. The objectives were accomplished by providing sufficient load paths for each component in a compact package.

8.1.1 Connection to Rotor

The connection to the rotor from the nacelle structure must be capable of retaining the full lift capabilities of the rotor while providing alignment measures to prevent the shaft from developing unwarranted oscillations. Two radial bearings are offset from each other to transfer bending moments generated by the rotor, while a thrust bearing transfers the thrust to the structure.

Lifting load transfer was accomplished by modifying a small portion of the rotor shaft to accept 6 bolts as seen in Figure 8.3(b). The holes are positioned offset from each other to allow for clearance and to not cause excess stress concentrations as seen in the rotor structure section. The holes allow for a custom sleeve which presses against a thrust bearing in the upper bearing housing. To prevent the shaft and rotor from damaging the internals of the gearbox, a second thrust bearing is placed between the flex coupling and gearbox assembly. The static resting weight of the rotor is then transferred through the housing of the gearbox and into the structure. During operation, no axial load is transferred through the gearbox, as the entire lifting force is taken by the upper bearing housing which uses three lift struts in Figure 8.3(a).

Each lift strut was capable of carrying the entire thrust load of the rotor individually with a factor of safety of 2. Although, it would reduce weight to only have two lift struts, the high 1/rev loads induced by the non-symmetric rotor would cause excess loads in each rod in transverse directions. Each lift strut

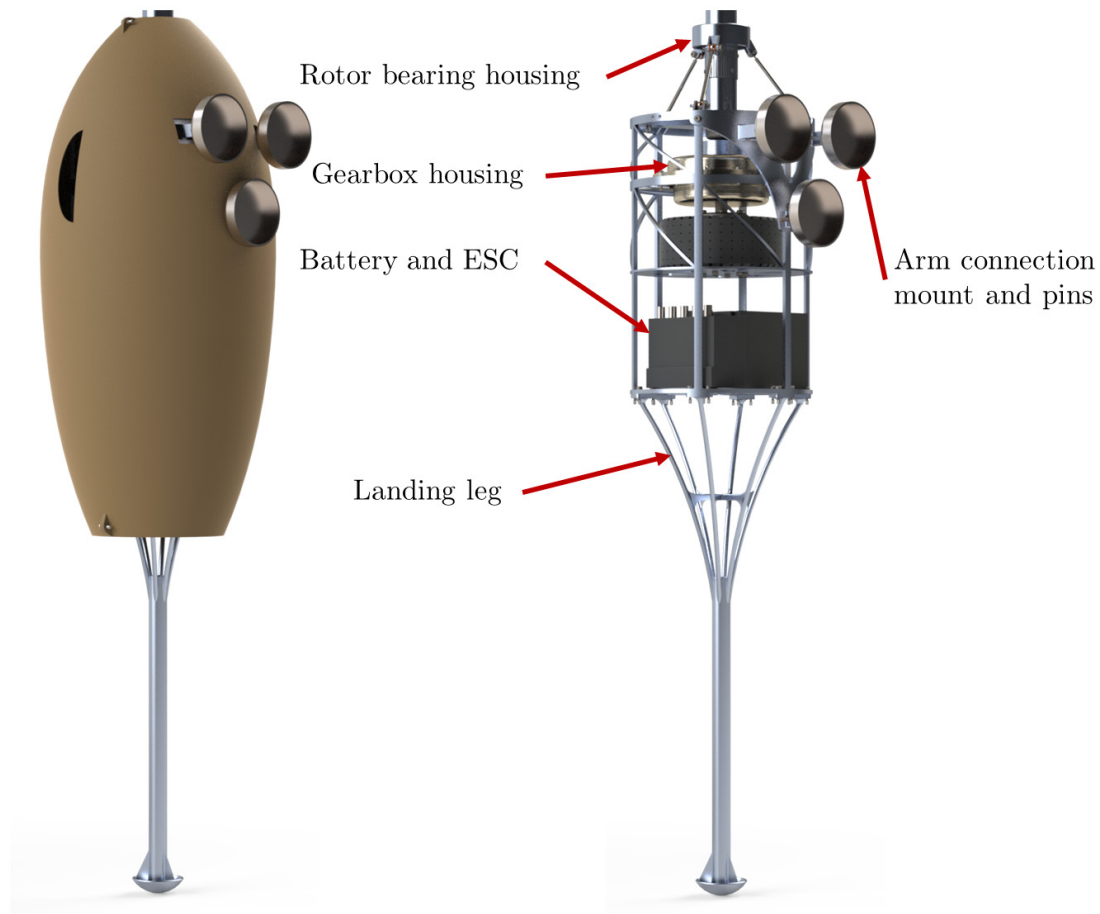


FIGURE 8.2: Nacelle assembly with and without cover

was designed for a 3.125 mm (0.25 in) diameter so standard eye bolts could be used. The lift struts were designed to have a factor of safety of 20 such that hardware used is common across all aspects of the nacelle.

8.1.2 Drivetrain Housing

The main components housed are the gearbox, motor, battery and ESC (electronic speed controller). Spatial accommodations for devices such as Light Detection and Ranging (LIDAR) sensors and IMUs (Inertial Measurement Units) are considered but not mentioned here, as the devices have minimal impact on the structural design.

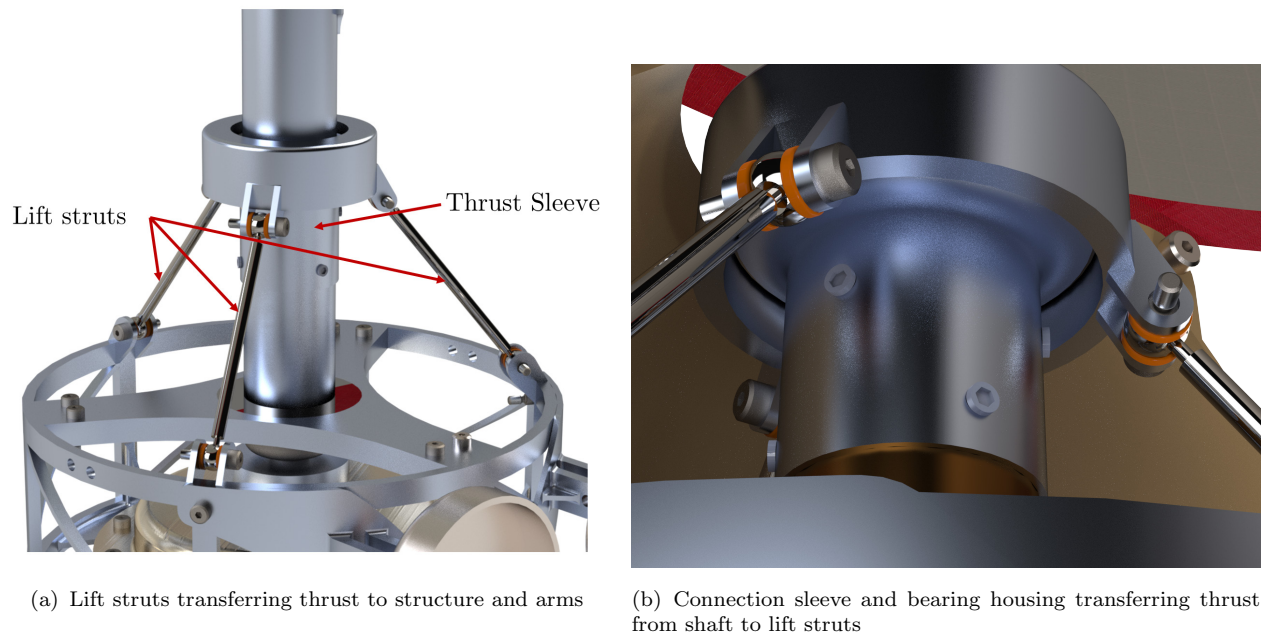


FIGURE 8.3: Connections holding rotor shaft

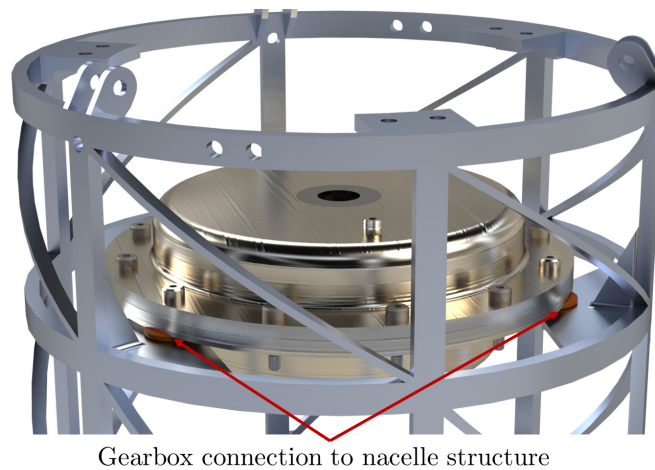


FIGURE 8.4: Gearbox shroud as positioned and connected in nacelle structure

The gearbox assembly, found in Figure 8.4, is housed in cast Magnesium-Zirconium alloy and is secured directly to the structure via three shoulder bolts distributed equally around the circumference. Due to the rotor shaft being directly connected to the gearbox, the torque transferred through the gearbox housing into the structure is 312 N-m (230 lb-ft). The hardware is more than sufficient for handling the loads at significantly lower radii; however, the standardization of hardware across the entire structure allows for easy assembly and tooling.

To transfer the torque of the motor effectively, a mounting plate of 3.175 mm (0.125 in) thick aluminum was used. Sections were removed in non-loaded areas to minimize weight. Adequate space was left for the routing of power and signal cables, with provision for active cooling as an option should a longer flight be considered. Slight modifications of length to the lower section would also allow for larger battery configurations.

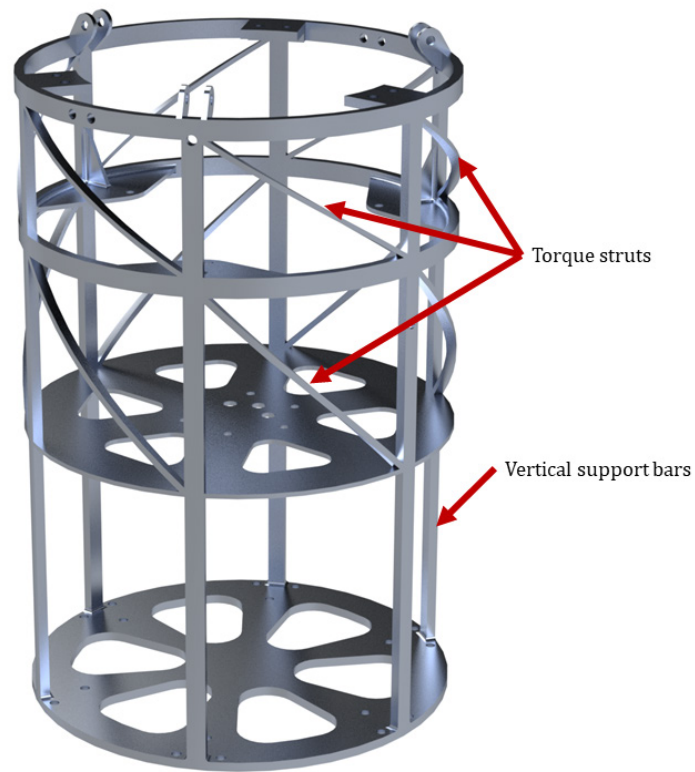


FIGURE 8.5: Nacelle structure as a single welded part

To assist the transfer of torque through the structure to each arm, struts were included between the upper rings in positions that acted as tensile members for clockwise and counter-clockwise orientations. The struts are mounted specifically for the rotation direction of each rotor, making clockwise and counterclockwise structures slightly different. Struts were not included for the shroud surrounding the battery and ESC due to torques not being transmitted to the landing legs seen in Figure 8.5. Vertical connections are maintained through aluminum bars to allow the structure to transfer loads through to the landing legs. The aluminum bars are a continuous part through the length of the enclosure, allowing for easy manufacturing.

To allow each component to be replaceable and have space to operate, adequate cutouts were provided when viewing from the top of the structure. Figure 8.6 depicts the rotor moment load transfer bar, which is removable in order to access the components below. The gearbox mount does not interfere with the assembly of the motor to its mounting position. Space is present between the motor and gearbox components to aid in air cooling of components.

The nacelle shown in Figure 8.2 includes side access holes to support airflow and assembly. The downwash passes by the opening due to the lower relative pressure compared to inside the nacelle. At the bottom of the nacelle, an opening exists which allows air to convect upward due to the higher pressure air further below the rotor. While the current iteration supports short duration flights, an active cooling solution may be adopted for longer durations. The top of the nacelle would have a larger diameter exposed such that the effects of downwash would be directly cooling components. Active cooling requires the installation of a radiator/fan combination and rearrangement of the battery configuration.

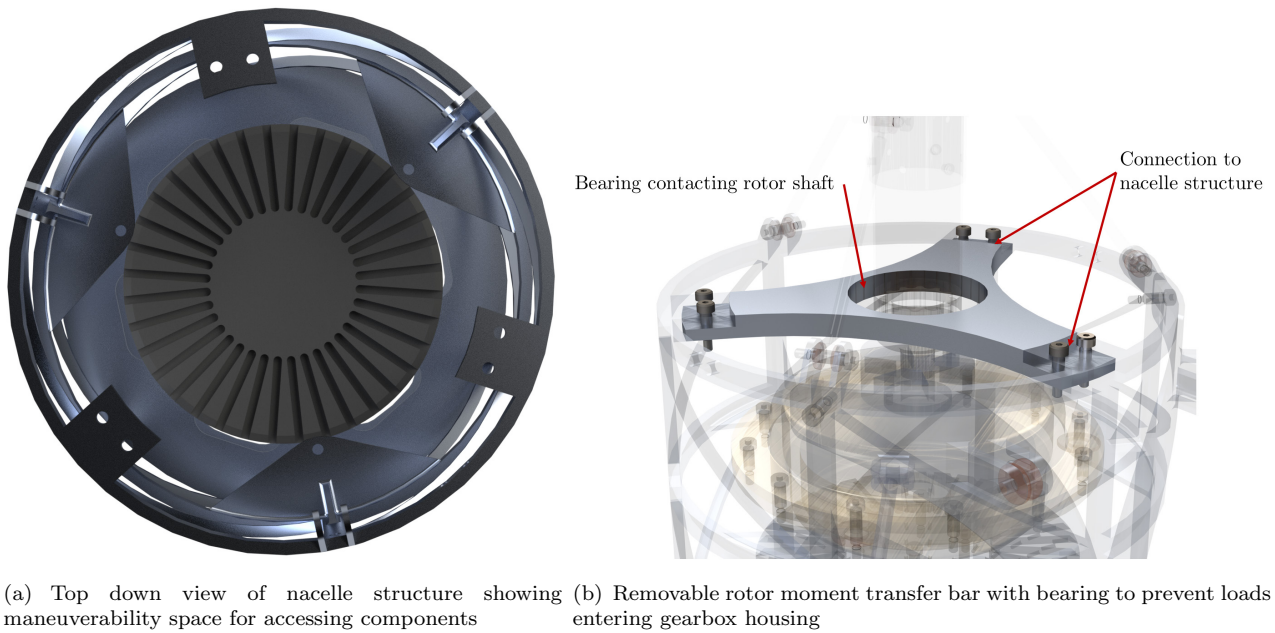


FIGURE 8.6: Access to inner components of nacelle structure

The ESC and batteries are accessible without the removal of the motor or gearbox, but instead directly through the lower vertical box beams. To secure the ESC and batteries during flight, they are bolted to the supporting plate on top of elastomeric dampers. This mounting configuration is mirrored on all vibratory components in the nacelle structure.

The structure is made out of weldable aluminum alloy 7039, which is heat treated post welding to remove internal stresses built up during the process of fabricating. By laser cutting a sheet of metal rolled into the cylindrical shape, fabrication would result in uniformity among arms. Alternatively, welding curved box beams and flat plates provides less waste material.

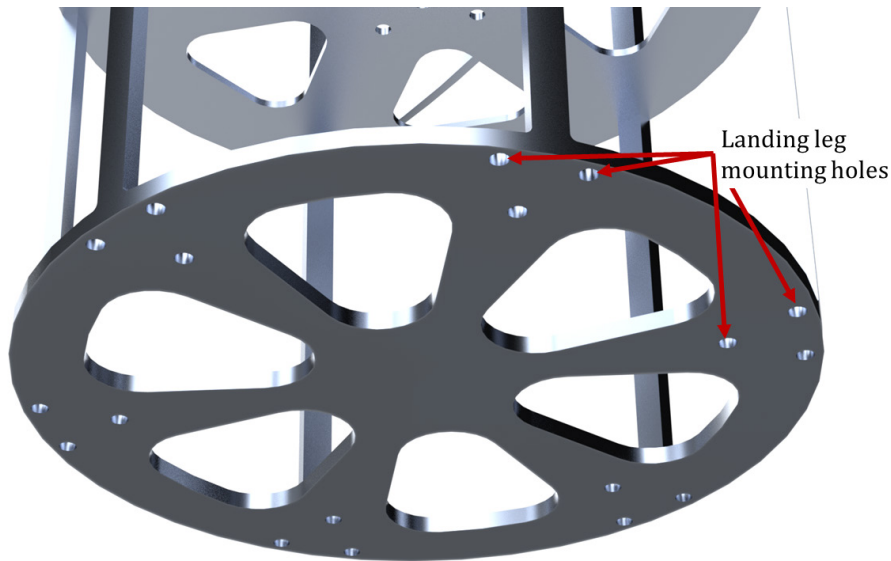


FIGURE 8.7: Array of landing leg attachments to nacelle structure

8.1.3 Landing Legs

Landing legs, as seen in Figure 8.8 are required to support the aircraft when landing and in extreme cases of failure. In the case of *Elicó*, having safe landing legs was even more crucial due to the position of the pilot underneath the structure. Crash landings impart shock loads to the system and can cause structural failures. Due to *Elicó* having the majority of weight at each rotor location, the risk for pilot safety was reduced. The total load absorption capacity of the landing legs remained unchanged.

The design drew from traditional helicopter landing skids, where upon landing, the skids flex to absorb the impact energy. This was achieved by diverting the loaded members outside of the optimal load path. The feet of each landing leg are rounded which allow for landing on soft and uneven ground.

For ease of fabrication and assembly, the landing leg is a separate part from the housing structure. It is attached via an array of bolts along the bottom plate where the battery and ESC are located as seen in Figure 8.7. The array is located in the same position as each vertical box beam to transfer loads directly to the structure rather than through the base plate. Similar to the drivetrain housing structure, the landing leg is also made from 7039 aluminum alloy to be weldable with a higher than average strength.

The legs are individually sized to sustain a fully vertical impact of 4g for the entire vehicle weight. Each leg has a factor of safety greater than 2 for this hard landing condition. The vertical impact is less detrimental to the structure than a transverse landing. The landing legs are extended from ground level high enough to provide vertical space for the pilot. The increased length provides a larger moment arm, thus smaller transverse loads have a larger effect on the legs rather than a similar vertical load. Despite the increased moment, a transverse load equal to 25% of the aircraft weight provides a factor of safety of 2.1 for each leg.

Total structure resonance must be taken into account when analyzing effectiveness and feasibility. Using the built in SolidWorks solver for frequencies, connection conditions were made for the arm connection points. Including the mass and position of battery, ESC and motor, the analysis provides a first natural frequency of 29.1 Hz for the nacelle structure only. With the frequency of the rotor loads occurring at 6.2 Hz due to large 1/rev oscillations, there will be no interactions of the nacelle structure resonance to the rotor main frequency.



FIGURE 8.8: Individual landing leg attached to nacelle structure

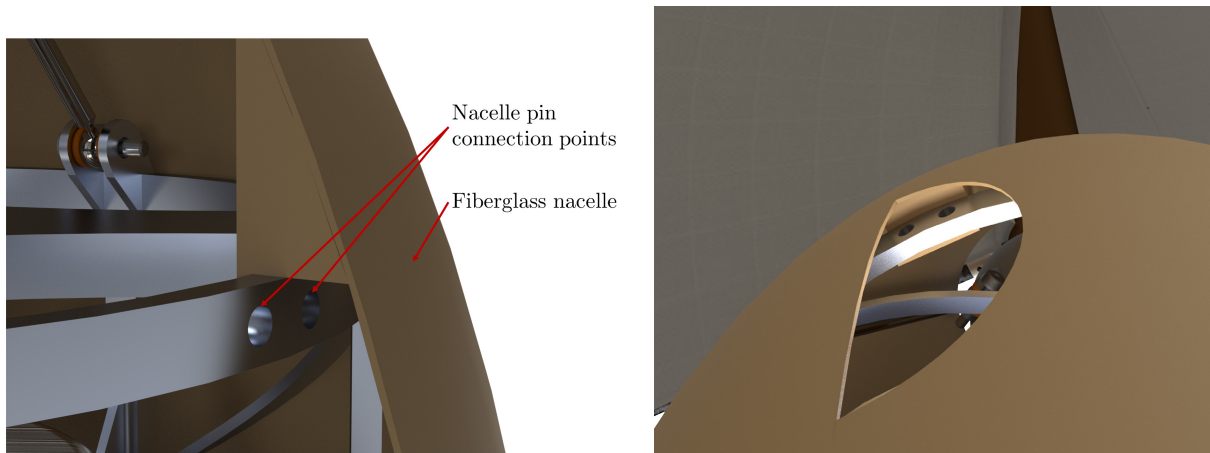


FIGURE 8.9: Connection point of nacelle shroud to nacelle structure and access cutout for assembly and airflow management

8.1.4 Nacelle Skin

The nacelle skin is divided into two halves for easy manufacturing and assembly as seen in Figure 8.9. The skin is made from 2 layers of fiberglass woven sheet to result in a light structure with the ability to hold its shape in the downwash of a rotor. Each portion is connected to the top ring of the nacelle structure with the same standardized bolts utilized elsewhere. To access the hardware when one portion of the shell is attached, a small access port is available to reach in. The access port also acts as an airflow port to assist with the passive cooling of the components. No rotor loads are transferred through the shell, as it only provides a smooth transition of air from rotor to ground. Space is left at the connection points to the arms to allow for cables and the aforementioned pin connections to be accessed.

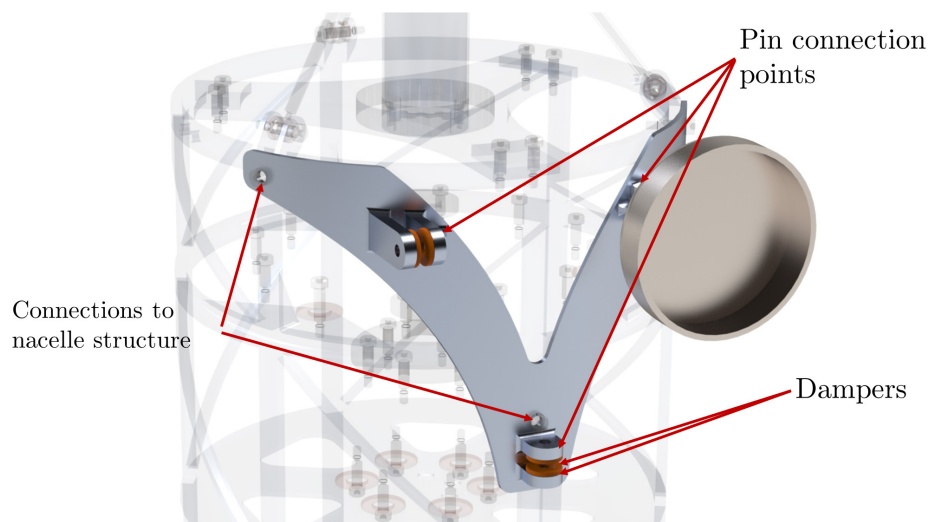


FIGURE 8.10: Connection to arms

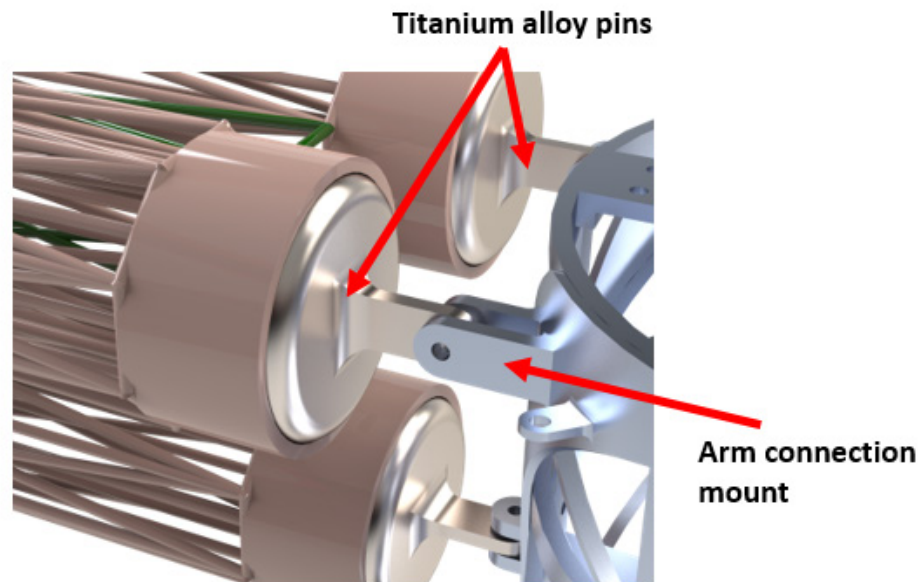


FIGURE 8.11: Arm to nacelle attachment

8.1.5 Connection to Arms

Each arm's nacelle structure requires a load bearing connection to the respective arm as seen in Figure 8.10. The connection had to be able to transfer the loads of the rotor effectively while not impeding the easy assembly capability of the overall structure. The connections to the arm consist of pinned tabs similar to those found on formula car suspension rods. In the case of *Elenco*, the rods are the tri-truss members. The pins and tabs act as quick, adaptable, yet safe connection methods.

To connect to the nacelle structure, the tabs are welded to a custom aluminum frame which is contoured to rest on the outside of the nacelle structure. Pins are used to connect to the nacelle frame in order to allow for easier replacement and fabrication techniques. The entire connection plate is laser cut and rolled to form, also following the same welding and heat treating principles as the nacelle structure.

From the nacelle structure, the moments and forces are distributed into the arms via the three arm connection pins. All are designed in a double shear case to reduce excess stresses and misalignment from vibrations. Two pins are oriented in a horizontal position while a single pin is oriented vertically. By having pins vertically, the lifting loads are able to be transferred more effectively, and the vertical pin allows for torque transfer in multiple directions.

The nacelle structure and cover provide a method of connecting the main structure to the rotors while housing essential components for operation. Rotor loads are transferable to the arms through the nacelle, making it a vital component in designing *Elenco*.

The nacelle structure and arms are connected by titanium alloy (Ti-6Al-4V) pins which are bolted to the nacelle structure via shoulder bolts. At the ends of each truss are unidirectional carbon fiber connection sleeves, which allow for attachment to the titanium pins.

On the other end of the titanium pin is the cylindrical portion which is bonded to the unidirectional cylindrical fiber sleeve of the cellular truss using DP-420 gray epoxy adhesive. The adhesive surfaces for this connection are the inner walls of the connection cylinder and the circular face of the titanium

alloy insert. Titanium is chosen over aluminum to avoid galvanic corrosion of the aluminum. Using a pinned connection at both ends of the cellular truss arms ensures ease of disassembly for maintenance purposes. The two arms placed on the top to take the compression bending, while the lone arm at the bottom is in tension. The two top pins were oriented horizontally for effective shear transfer, while the bottom was positioned vertically for effective torque transfer. FEA was also conducted on the pins to ensure that the pins did not deform when the rotor thrust and torque were applied. The minimum factor of safety from this loading condition was 2 as shown in Figure 8.11.

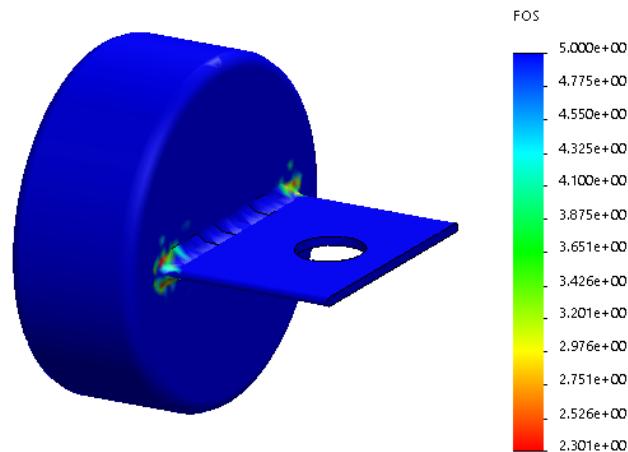


FIGURE 8.12: Finite element analysis of titanium pins

8.2 Arms Structures Design

Elicó's arms structure comprises of three cellular truss members sized to support the rotor's static and dynamic loads. Due to the shortened flight duration for *Elicó*, emphasis was placed on choosing a very lightweight structure capable of withstanding the rotor loads in hover, which is the primary flight condition for this mission. Because of the limited speed requirement, aerodynamic design was not a priority for the arms. A wing structure was considered to be too heavy because of the additional weight of the skin, therefore a truss configuration was immediately attractive based on the aforementioned criteria.

8.2.1 Truss Configuration Selection

The quadrotor configuration of *Elicó* requires four structural arms capable of bearing the rotor loads in hover. The ultimate goal of the truss design was to ensure that the lightweight truss would react these loads, without any significant structural deflections that would impair the vehicle in any manner. Off-the-shelf carbon fiber tubes were considered for the truss structure, but the invariability of sectional properties limited analysis and thus was eliminated from consideration. Micro-truss technology developed and implemented on the Human Powered Helicopter by the Gamera team from the University of Maryland [10], was also considered but the large cross-sectional area would present issues with attachment to the nacelle. The specific truss selected for *Elicó* was an inverted triangular configuration of cellular trusses. The truss is a three-dimensional lattice structure with remarkable strength-to-weight characteristics. It achieves its high strength-to-weight capabilities by a distinctive geometry of longitudinal and helical members wound together. The longitudinal members run parallel

to the centroidal axis, while the helical members spiral around this axis [11]. The longitudinal members carry the axial and bending loads. Similarly, the helical members provide the torsional rigidity while also supplying lateral stability for the longitudinal members.

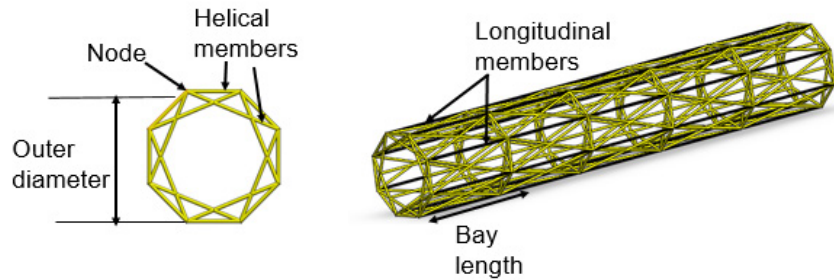


FIGURE 8.13: Components of the cellular truss

The parameters used in designing the cellular truss are: the number of nodes, bay length, inner and outer diameter of the truss cross-section and the material type. Figure 8.13 shows different cross-sectional single grid configurations for the truss. The cellular truss cross-section chosen for *Elico* is an 8-node double grid configuration shown in Figure 8.14.

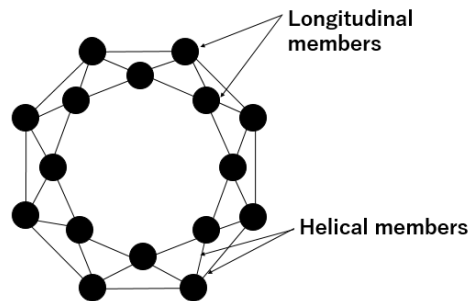


FIGURE 8.14: 8-node double grid truss cross-section

By dispersing the members around a common centroidal axis, the cross-sectional moment of inertia about the neutral axis is increased, therefore raising the flexural stiffness. Furthermore, an 8-node double grid lattice provides a smoother outer surface as opposed to a 6-node grid configuration with protruding outer nodes. A triangular configuration of cellular trusses was then considered not only to increase the cross-sectional moment of inertia, consequently increasing bending stiffness, but also to effectively react the side forces and moments from the rotor and minimize weight.

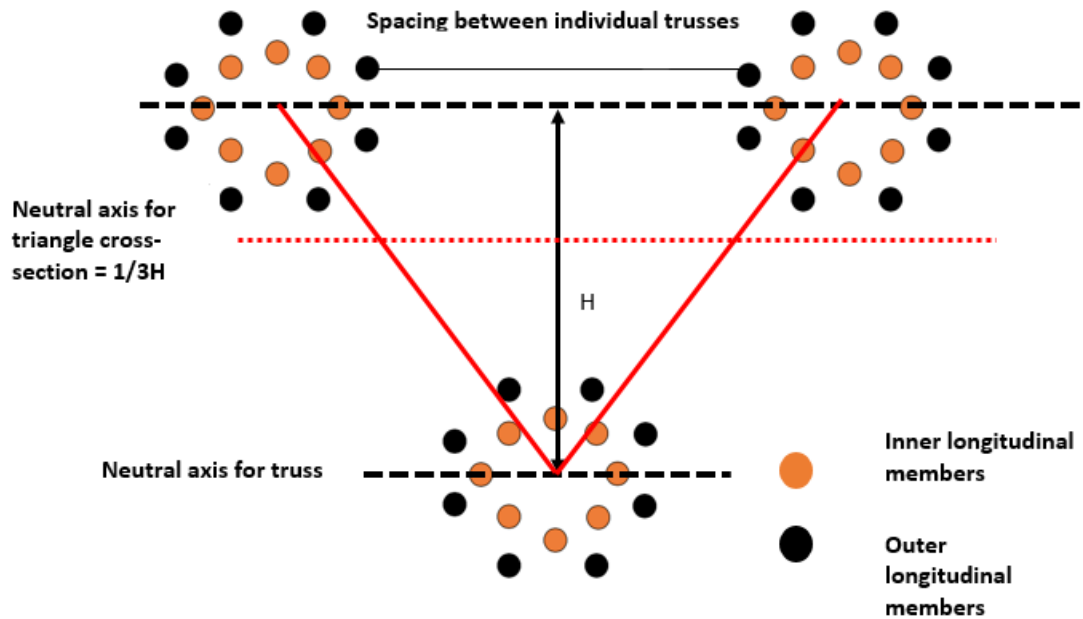


FIGURE 8.15: The triangular cellular-truss cross-section

8.2.1.1 Rotor support arms sizing

A unidirectional carbon-fiber Toray T700SC-18000-50C pre-impregnated with TCR Composites UF3369-100 resin system was chosen for the cellular truss on the grounds of relative strength to weight ratio. The properties for the carbon-fiber/epoxy polymer used for the truss are shown in Table 8.1.

TABLE 8.1: Carbon Fiber-Epoxy Material properties

	Metric	Imperial
Density	1661 kg/m ³	0.06 lb/in ³
Young's Modulus (E)	129 GPa	1.87 × 10 ⁷ psi
Ultimate Tensile Stress σ_{ult}	1200 MPa	1.74 × 10 ⁵ psi

The cellular truss was sized based on the applied bending moment from the rotor thrust. The effect of rotor torque was also considered, but analysis showed that the dominant loading came from the thrust with the latter constituting 81 % of the bending moment at the root of the arms. Initial sizing analysis showed that each rotor support arm would need to support a tip load of 700 N (157 lb) from the rotor thrust. This resulted in the two top cellular trusses undergoing compression while the bottom truss members experienced tensile loading. The maximum bending stress was predicted to be experienced by the member furthest away from the triangular neutral axis at the bottom of the triangular-truss configuration. The limiting factor for the truss sizing was the local member compression buckling, for which a factor of safety of 1.5 was applied to give the truss dimensions shown in Table tab:tri-cellular props.

$$\text{Factor of Safety (FOS)} = \frac{\text{Buckling load}}{\text{Compressive force}} = \frac{\frac{\pi^2 EI}{(0.8L)^2}}{\sigma_{compression} A} \quad (8.1)$$

Fig. 8.16 shows a single truss bay. This factor of safety was particularly sensitive to the bay length. The bay length is the repeating unit in the longitudinal direction, which combined together forms the entire cellular truss beam. A bay length of 0.3048 m (1 ft) was chosen for *Eluco* in order to obtain a FOS of 1.5. A rotor radius of 1.46 m (4.79 ft) meant that a beam length of 1.83 m (6 ft) would constitute 6 bays. This ensured a rotor shaft to shaft spacing of 3.37 m (11.06 ft) between adjacent shafts in the quadrotor configuration.

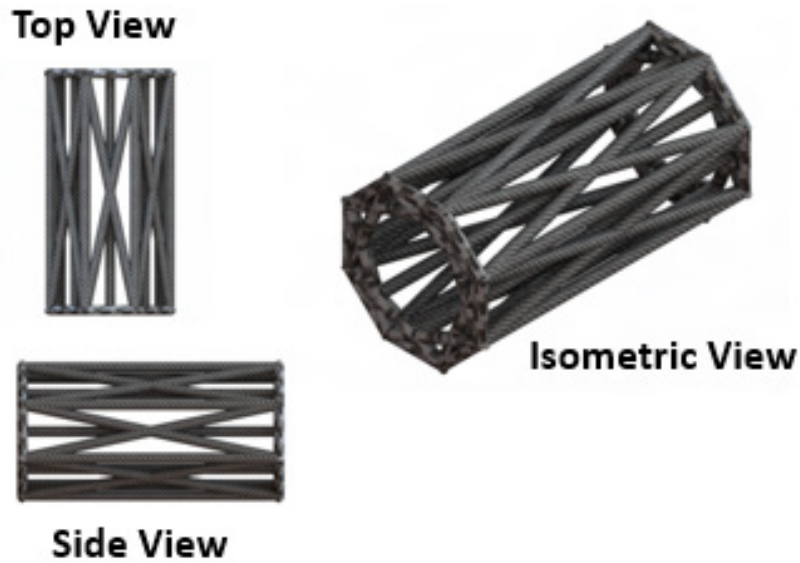


FIGURE 8.16: A cellular truss bay

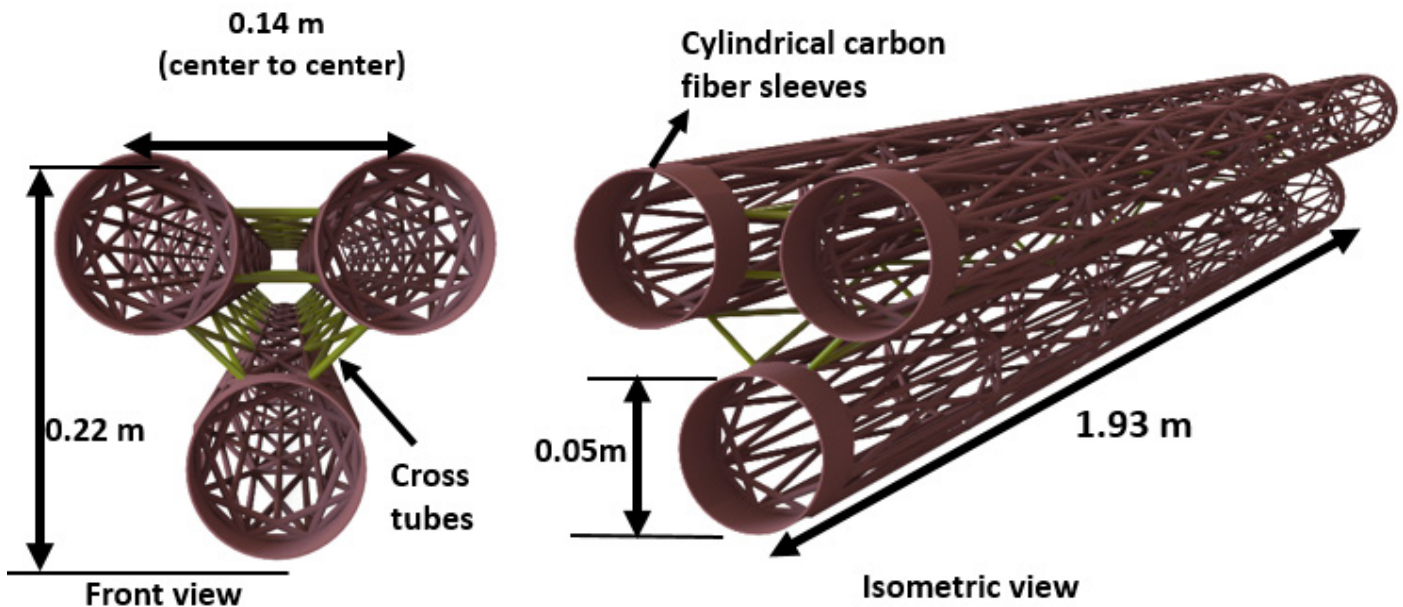


FIGURE 8.17: Fully assembled tri-cellular truss

TABLE 8.2: Tri-cellular truss properties

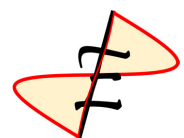
Parameter	Metric	Imperial
FOS in buckling	1.5	1.5
FOS in tension	34	34
FOS in compression	52	52
Bay length	0.305 m	12 in
Outer radius	5.08 cm	2.0 in
Length	1.93 m	6.33 ft
Spacing between trusses	14.5 cm	5.7 in
Longitudinal outer diameter (OD)	0.51 cm	0.20 in
Cross-tubes OD	0.51 cm	0.20 in
Weight	6.9 kg	15.3 lb
Bending stiffness (EI)	$7.13 \times 10^5 \text{ Nm}^2$	$1.49 \times 10^4 \text{ lbft}^2$
Tip deflection	2.03 mm	0.08 in
First natural frequency (ω_B)	21.8 Hz	21.8 Hz

Due to the 1/rev rotor oscillatory loads, it was important that the bending frequency of the arms structure was not in the vicinity of the nominal rotor RPM of 6.1 Hz. This minimizes the dynamic amplification of rotor loads due to resonance. Table 8.2 shows the calculated first bending frequency to be 21.8 Hz.

Figure 8.17 shows the full tri-cellular truss and the associated dimensions. Integrally wound sleeves from the tows use to wind the longitudinal and helical members continue down to form carbon cylindrical connection sleeves at each end. These sleeves are 0.051 m (2 in) long to allow for adequate adhesive bonding surface area to the connection pieces. The yellow cross tubes shown in Figure 8.17 provide lateral stability for the structure and also contribute to the torsional stiffness of the arms structure.

8.2.2 Finite Element Analysis (FEA) of Rotor Support Arms

A static analysis on the rotor support arms was carried out in Solidworks to examine the response to rotor loads. The primary loading case was the rotor thrust and the axial stress distribution on the arms, shown in Figure 8.18. Because the arms are bolted at the fuselage end, the root of the arm is assumed to be fixed. As expected, the compression stress regions occur at the top of the beam, with the bottom arm in tension. The bending stress analysis showed that the region of maximum bending occurs at the bottom member where it is furthest from the neutral axis of the triangular configuration, which is in agreement with the initial analysis. Table 8.3 shows the results from FEA. The axial stress results also revealed the diagonals and cross-members to be load bearing members contributing to the bending stiffness of the structure as shown in Figure 8.18.



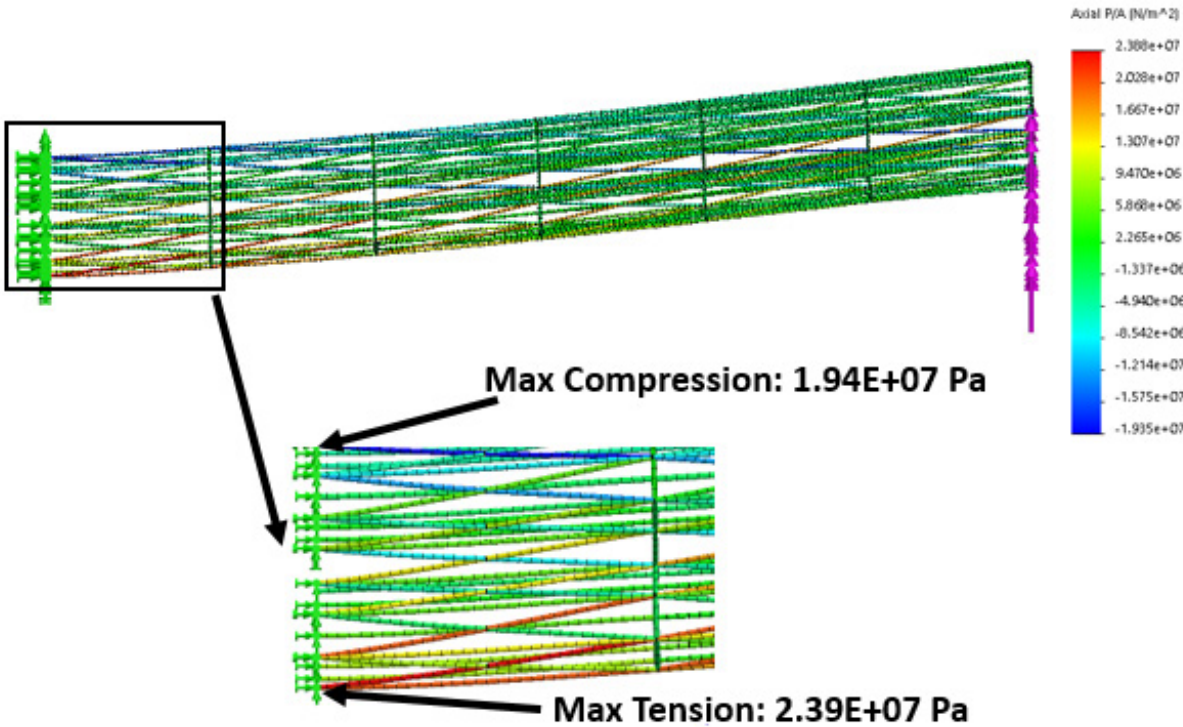


FIGURE 8.18: Axial stress distribution on arms from rotor thrust

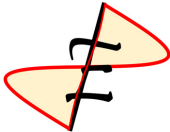
TABLE 8.3: FEA Results

Parameter	Metric	Imperial
σ compression	1.94×10^7 Pa	2.81×10^3 psi
σ max bending	2.67×10^7 Pa	3.87×10^3 psi
Tip deflection	2.96 mm	0.12 in
Bending stiffness (EI)	5.76×10^5 Nm ²	1.20×10^5 lbft ²
Moment of inertia	7.45×10^{-6} m ⁴	8.63×10^{-6} ft ⁴
Bending frequency (ω_B)	15.5 Hz	15.5 Hz

After careful sizing and analysis, the arms and attachment pins were sized to react to the rotor loads at minimum weight based on appropriate safety margins. The final weight breakdown for the arms and the connection is shown in Table 8.4.

TABLE 8.4: Arms weight breakdown

Component	Metric	Imperial
Four arms	27.2 kg	59.9 lb
Connection pins for side arms (4 per arm)	7.2 kg	15.9 lb
Connection pins for bottom arm (2 per arm)	1.68 kg	3.7 lb



8.2.3 Manufacturing Process

The cellular truss is fabricated through a continuous filament winding process using a mandrel. A mandrel centered radially in a steel pipe is typically the set up for the truss braiding process, in which the tows are wound under tension [12]. Because all three trusses have identical properties, a single mandrel could be used for the fabrication process. After the mandrel is prepared, the cylindrical transition ends for the trusses are machined on the proper locations on the mandrel. Based on the dimensions given for the truss members, 18-K tow prepreg carbon fiber is used for the layup of each truss member. Eighteen tows are used for each of the inner and outer members since they have equal diameters. The winding sequence is done in a manner to provide optimal interlocking at the nodes where the longitudinal and helical members intersect. The filament winding process is typically automated with a Programmable Logic Controller (PLC) controlling the winding sequence. The cellular truss is then cured in an autoclave and finishing techniques are applied to remove residual material and rough edges smoothed out.

8.3 Central Structure

A pyramidal central structure made from aluminum was designed to enable attachment to all four cellular truss arms. The structure employs pinned tabs similar to the same connections used between the arms and the nacelle, with three protruding tabs on each side for each truss arm. The central structure was sized to effectively react the applied bending moments from the rotor thrust and torque, resulting in a weight of 3.95 kg (8.7 lbs). Figure 8.19 shows the connection of the central structure to the 4 rotor support arms. The two top pins are oriented horizontally to allow for effective load transfer for the thrust, while the bottom pin is oriented vertically for improved torque transfer. The titanium pins from the arms are pinned to the tabs via shoulder bolts connection. Because of the pyramid shape, the length of the bottom pin was increased to 12.7 cm (5 in) to allow for assembly between the titanium pins and the structure. The structure is also designed to have a rounded top to enable the attachment to the cockpit.

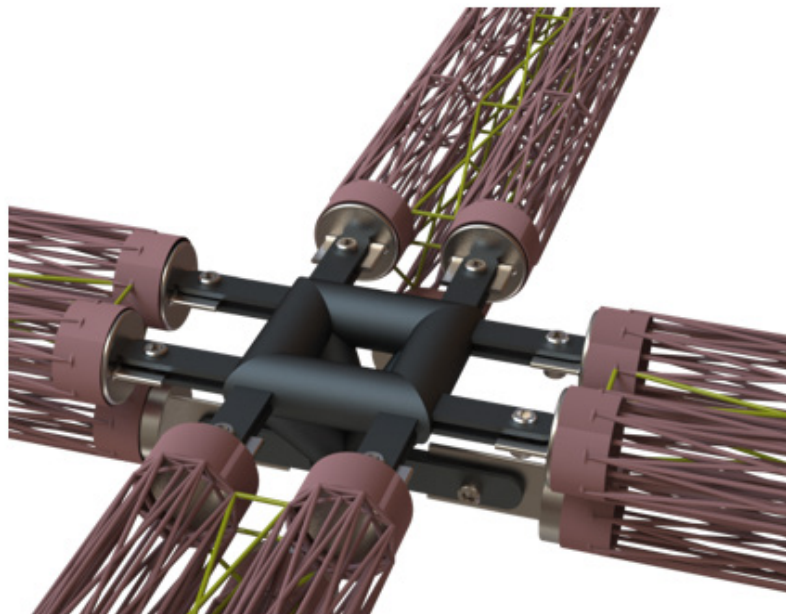


FIGURE 8.19: Arms to central structure attachment

9 Propulsion and Transmission

9.1 Battery Selection

A review of existing batteries began by considering the different types of batteries available in the consumer market and their specifications. Lead-acid, Nickel metal hydride, and Lithium ion (Li-ion) batteries were considered due to their availability in the market. Figure 9.1 shows that Li-ion type batteries have the highest energy densities currently available. Lead-acid, nickel metal hydride, and the other types of batteries have advantages over lithium type batteries, such as increased cold temperature performance. However, these were of secondary concern, as high energy density batteries are critical to aerospace grade applications.

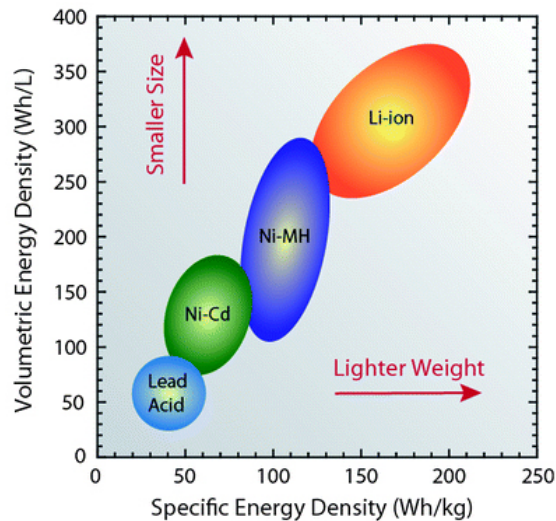


FIGURE 9.1: Commercial battery types and their power densities

A market survey determined potential lithium based batteries for *Elicó's* design and identified several prominent battery vendors, such as: Turnigy, Traxxas, and MaxAmps. After comparing available voltages, energy capacities, and price, the MaxAmps 12S 44.4V 22 Ah battery was found to have the best qualifications for the RFP mission, as it had an energy density of 193 Wh/kg and a power C-Rating of 40C. However, the battery depth of discharge is 80%, yielding an effective battery capacity of only 155 Wh/kg, which was used to inform the 150 Wh/kg capacity value for the sizing analysis.



Parameter	Value
DC Voltage	44.4 V
Advertised Energy Capacity	22 Ah, 193 Wh/kg
Mass	5.05 kg
Maximum C-Rating	40C
Depth of Discharge	80%
Effective Energy Density	17.6 Ah, 155 Wh/kg
Effective Power Density	6.2 kW/kg

FIGURE 9.2: MaxAmps reference battery specification

9.2 Electric Motor Trade Study

Critical to the success of *Elicó's* quadcopter design was the ability to use electric motors, with their quick timing responses, to accurately control the RPM of the aerial screw. When selecting the type of motor to be used on *Elicó*, a market study on commercially available electric motors was completed in order to analyze which types of motors should advance towards the detailed design phase. A comparison between commercially available brushless DC motors and AC induction motors is shown in Table 9.1.

TABLE 9.1: Market review of available electric motors

Brushless DC Motors				
Make/Model	P_{peak} [kW]	P_{cont} [kW]	m [kg]	P_{cont}/m [kW/kg]
EMRAX 188	52	30	7.0	4.3
EMRAX 208	68	41	9.1	4.5
EMRAX 268	200	107	20	5.4
YASA 750H	200	75	25	3.0
UQM Technologies Hi-Tor	50	30	41	0.74
UQM Technologies PP100	100	60	50	1.2
UQM Technologies PP125	125	45	41	1.1
UQM Technologies PP220	250	122	41	2.97
AC Induction Motors				
Make/Model	P_{peak} [kW]	P_{cont} [kW]	m [kg]	P_{cont}/m [kW/kg]
AC Propulsion 150	150	40	80	0.5
Tesla Motors S and X	185	50	52	0.98
Raser Teeth	200	107	112	0.48
Brusa HSM1	156	93	51	1.82
Brusa SSM1	160	60	49	1.22

The peak power, continuous power, and mass were determined for each type of motor, and the results are logged in Table 9.1. From the market survey, it is clear that EMRAX axial flux motors have the highest power densities of all motors that were considered. As such, the EMRAX axial flux motors were selected to be used in the detailed design phase.

9.3 Motor Controller Selection

After the EMRAX motors were found to have the highest power to weight ratios out of any electric motors considered, the next step was to pair the motor with a motor controller. EMRAX lists several companies that they have partnered with specifically to design motor controllers, mainly: Servon, Cascadia Motion, and emDrive. Each company was surveyed to determine the power densities of their products, with the results shown in Table 9.2.

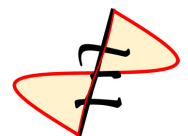


TABLE 9.2: EMRAX motor controller trade study

Company	Model	$P_{DC,cont}$ [kW]	m [kg]	$P_{DC,cont}/m$ [kW/kg]
Servon	Gen4 HVLP	25	2.3	10.9
Cascadia Motion	RM100	123	8.0	15.4
emDrive	H300	190	7.5	25.3

The motor controller was selected to be the emDrive H300, as it was found to have a high continuous power density of 25.3 kW/kg and operated at or above 95% efficiency. The emDrive H300 was scaled to operate at the required power setting based on the motor's operating characteristics.

9.4 Detailed Powertrain Analysis

When designing the powertrain system, it is important to start at the rotor's operating point and then size the motor, motor controller, and battery in that order. The design variables for the detailed powertrain analysis are to determine the operating DC bus voltage V_{DC} for the battery and steady state DC current I_{DC} being drawn for the battery.

Two stock EMRAX motors were considered, the EMRAX 188 and EMRAX 208 axial flux motors, at 3 different operating voltages each. After reviewing the motor efficiency plots, shown in Figure 9.3, a gear ratio of 10.75 was selected in order to ensure that either motor operating at above 90% efficiency. This placed the motor operating point at 31.3 Nm at 4000 RPM.

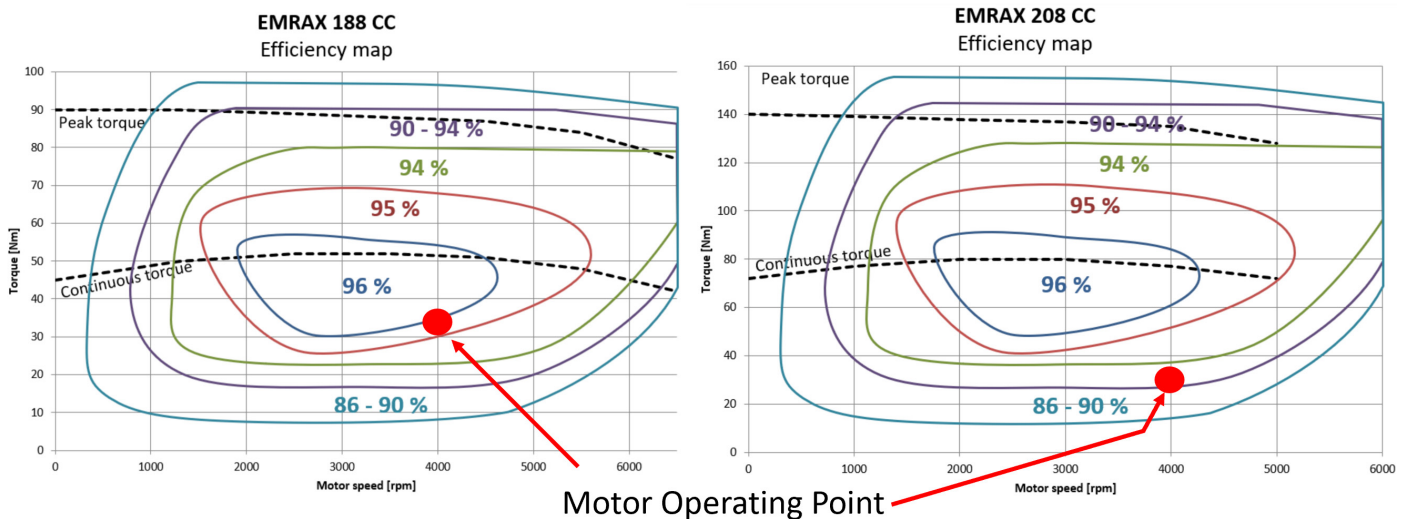


FIGURE 9.3: Efficiency plots for the EMRAX 188 and 208 brushless DC motors

The EMRAX motor specification sheets contained information on the motor's torque constant K_T , or amount of torque per amp of AC current I_{AC} , at different operating voltages. These data sheets allowed for the overall all-electric powertrain mass (motor, motor controller, and battery) to be calculated for each voltage setting. It is important to note that for both EMRAX motors, each operating voltage had a distinct K_T , which greatly affected the required current to run each motor. The effects of voltage

selection and resulting battery mass are considered in greater detail in the following sections. DC voltages between 100-450 VDC were considered.

The reference battery from MaxAmps, shown in Figure 9.1, was scaled in order to satisfy the vehicles powerplant requirements. A scaling factor was applied to the battery to account for the required DC battery voltage and a separate scaling factor accounted for the required energy capacity. Both scaling factors helped to determine the required battery mass. For example, if the design called for twice the voltage and twice the capacity of the reference battery, the required battery would weigh 4 times the reference battery. Although the reference battery had an advertised 22 Ah capacity, the design assumed a 17.6 Ah effective capacity due to the fact that only 80% of the battery's capacity would be discharged. The battery sizing estimate can be written as:

$$m_{bat} \text{ [kg]} = \underbrace{\left(\frac{V_{DC} \text{ [V]}}{44.4 \text{ [V]}}\right)}_{\text{Voltage scaling factor}} \times \underbrace{\left(\frac{4I_{DC}TOF \text{ [Ahr]}}{17.6 \text{ [Ahr]}}\right)}_{\text{Capacity scaling factor}} \times \underbrace{(5.05 \text{ [kg]})}_{\text{Reference battery mass}}$$

This allowed for the battery mass to be calculated for each operating voltage and for each motor. The results of the detailed powertrain are shown in Table 9.3:

TABLE 9.3: Effect of battery voltage on powertrain mass. The total mass m_{tot} is the sum of the battery, motor, and motor controller masses for the entire vehicle

EMRAX 188 Motor, $m_m = 7.0 \text{ kg}$, $\eta_m = 95\%$					
V_{DC} [V]	K_T [Nm/ A_{rms}]	I_{AC}/arm [A_{rms}]	I_{DC}/arm [A]	$\Sigma m_{battery}$ [kg]	m_{tot} [kg]
110	0.15	208.7	132.0	18.8	49.1
300	0.39	80.3	48.4	18.8	49.1
430	0.60	52.2	33.8	18.8	49.1
EMRAX 208 Motor, $m_m = 9.2 \text{ kg}$, $\eta_m = 90\%$					
V_{DC} [V]	K_T [Nm/A]	I_{AC}/arm [A_{rms}]	I_{DC}/arm [A]	$\Sigma m_{battery}$ [kg]	m_{tot} [kg]
120	0.19	171.2	132.8	20.6	60.0
350	0.50	65.0	45.5	20.6	60.0
550	0.80	40.7	29.0	20.6	60.0

The results of the detailed powertrain analysis show that the EMRAX 188 motor results in a configuration that has a lower overall weight when compared to the EMRAX 208 configuration. This is due to the fact that the EMRAX 208 motor operates at a lower efficiency at the hover operating point than the EMRAX 188 motor. The DC voltage level for EMRAX 188 motor was determined by examining the required DC current per arm (I_{DC}/arm). The 430 V design was selected as it resulted in only 33.8 A/arm, as it has the lowest $I_{DC}R_{wire}$ voltage drop between the battery and motor. The finalized powertrain components are shown in Figure 9.4.

FIGURE 9.4: *Elico's* final power train components

9.4.1 Battery Placement Consideration

After evaluating the required DC current for each arm, wires could be sized to carry the appropriate load. Traditional consumer off the shelf (COTS) quadcopters typically have only one battery located at the center of the vehicle and have wires running the entire length of the arms. However, adopting this methodology required sizing wires to run the entire length of the arm. It was found that by diverging from existing trends and placing the battery at the end of each arm resulted in a 94% reduction in wire length when compared to having a single central battery. Figure 9.5 shows the differences between the two battery placement configurations.

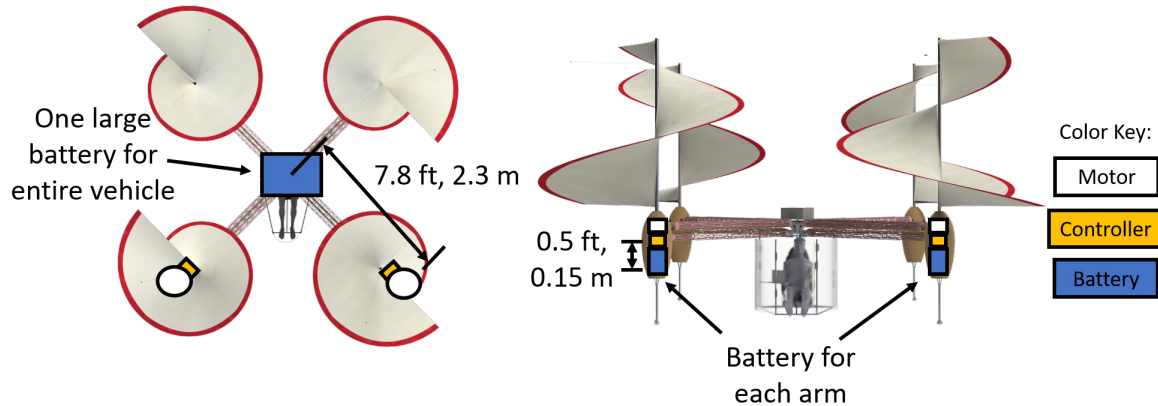


FIGURE 9.5: Battery placement options

In addition to significantly reducing the wire weight, placing the battery at the end of the arms helped alleviate the structural loads placed on the arm's truss structure. The tradeoff for placing the battery at the end of the arms is that there are now four separate batteries as opposed to one central pack. This increases the operational overhead and control logic of the vehicle. It was deemed that the benefits of reduced wire weight and reduced structural loads on the truss justified the decision to have four batteries on the vehicle.

9.4.2 Propulsion Power Schematic

The finalized powertrain design uses an all electric topology, featuring an EMRAX 188 brushless DC motor, a scaled emDrive H300 motor controller, and a scaled MaxAmps battery operating at 430 VDC. Due to the dramatic differences between the required motor voltage (430 V) and the avionics voltage (<15 V), it was determined that separate auxiliary batteries would be required to power the avionics. These auxiliary batteries were sized to power the avionics for 60 minutes to allow sufficient time for software development and hardware in the loop testing and have a total mass of 1.4 kg (3.08 lb). In addition, auxiliary batteries provided redundancy in the event that one nacelle fails, the others may continue to operate. A detailed discussion of *Elico's* avionics is given in Chapter 10.

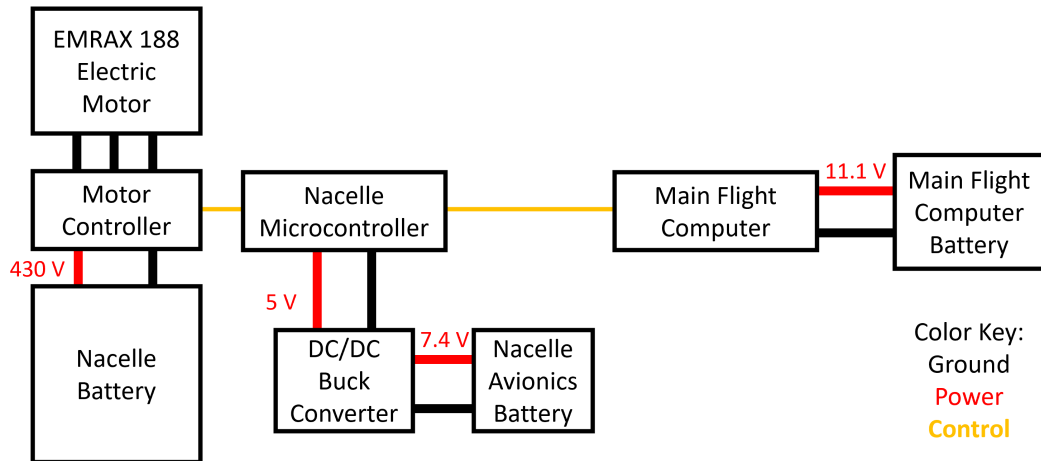


FIGURE 9.6: *Elico's* power schematic (only one nacelle shown for clarity)

9.5 Gearbox and Shaft Connections

The drivetrain is responsible for transferring the power from the motor to the rotor in an efficient and lightweight method. A standard transmission system for rotorcraft will include multiple gear train accessories for powering alternate items in the vehicle, such as the pilot interfaces, or accessories. In *Elico*, no power is needed to divert from the drivetrain, as all power was obtained from separate low voltage battery systems.

9.5.1 Gear Stages

There are two gear stages in the design of the gearbox seen in Figure 9.7. The stages were decided as planetary for the reasons of load sharing, size, and location constraints. Since each rotor has an individual drivetrain, each gearbox must be compact and reliable. Using other common layouts of gearing, such as large bevel or face gearing systems would be useful for a layout of a helicopter with a tail rotor. But with *Elico*, all rotors are separated mechanically, requiring no transmission interaction between rotors.

Each motor chosen for *Elico* operates most efficiently at 4000 RPM with each rotor operating at 367 RPM. This is achieved with a gear reduction of 10.75:1. With a planetary gearbox, load sharing is intrinsic to the design. By having multiple planet gears, the torque of the sun gear is split between multiple teeth, allowing for more weight savings by reducing diameters and size of teeth. Planetary gears

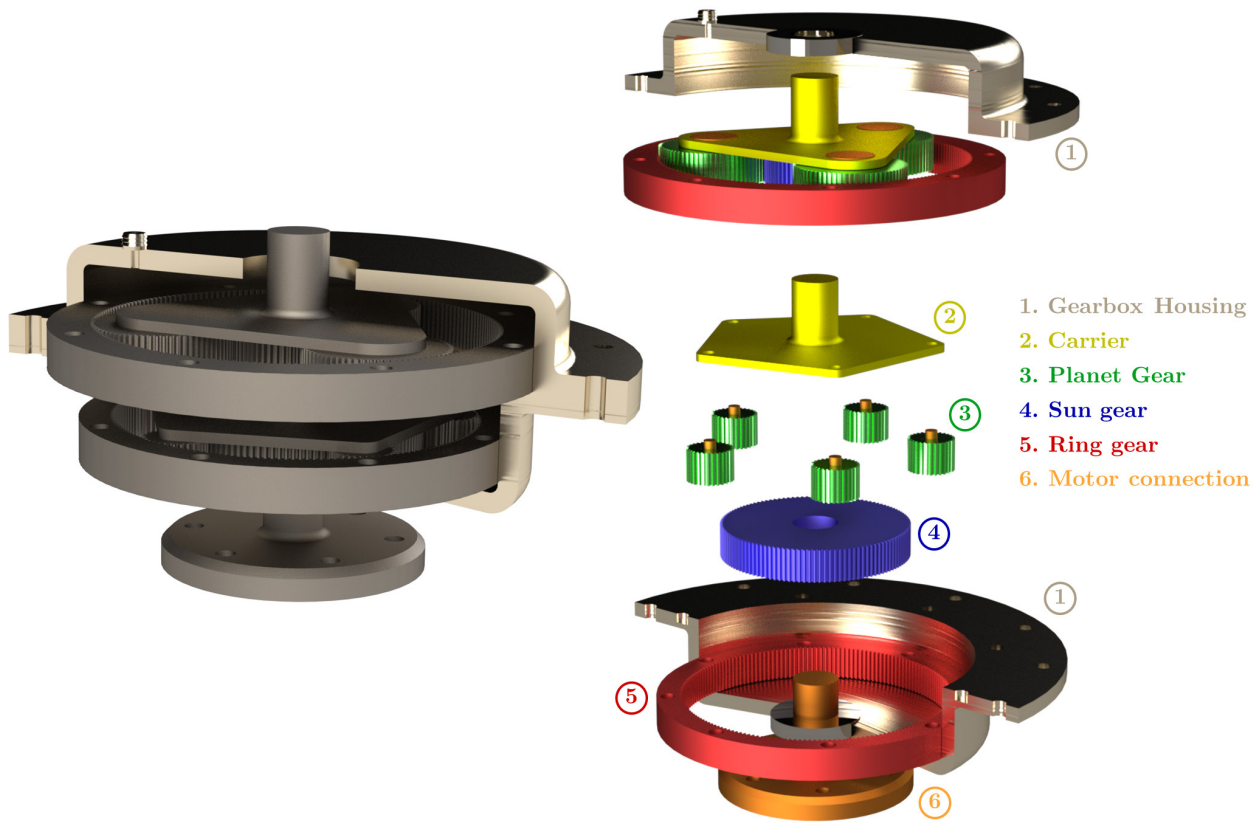


FIGURE 9.7: Gearbox with planetary gear reduction stages

have limited maximum ratios determined by geometry. To determine the size of the gearing, number of teeth and number of planets, a sizing code was deployed using AGMA standards and calculations [13].

To ensure the planets are evenly spaced around the periphery, the following must be true:

$$\frac{N_S + N_R}{N} = Integer$$

And to ensure no interference of adjacent planets:

$$N_P + 2 < (N_S + N_P) \sin\left(\frac{180}{N}\right) = Integer$$

where,

N_P is the number of teeth on planet gear

N_S is the number of teeth on sun gear

N_R is the number of teeth on ring gear

N is the number of planet gears.

Stresses for each gear are calculated using contact and bending stress on the teeth. The equations, formatted for U.S. customary units, are:

$$\sigma = W^t K_o K_v K_s \frac{P_d K_m K_B}{F J}$$

$$\sigma_c = C_p \sqrt{W^t K_o K_v K_s \frac{K_m C_f}{d_p F I}}$$

where,

W^t is the tangential transmitted load, N (lb)

K_o is the overload factor

K_v is the dynamic factor

K_s is the size factor

P_d is the transverse diametral pitch

F is the face width of the narrower member, mm (in)

K_m is the load-distribution factor

K_B is the rim-thickness factor

J is the geometry factor for bending strength (which includes root fillet stress-concentration factor K_f)

C_p is an elastic coefficient, $\sqrt{\text{N}/\text{mm}^2}$ ($\sqrt{\text{lb}/\text{in}^2}$)

C_f is the surface condition factor

d_p is the pitch diameter of the pinion, mm (in)

I is the geometry factor for pitting resistance

Interference of gearing and uneven wear are concerns when designing the stages. To keep gearing from wearing unevenly, non-integer gear ratios are chosen. Alternatively, gear ratios might be chosen such that planet gears would not be evenly spaced around the perimeter of the sun gear. The misalignment would cause oscillations and lead to more wear of the system. Another spatial concern of planetary gearing is the number of planets. If a single stage has too many planet gears, they will begin meshing with each other, thus binding or being physically impossible to manufacture. Combining both methods of spatial checking restricts the bands of acceptable gear ratios for planetary gears. Physically, they are also restricted by the maximum gear ratio, becoming over sized or impossible if the gear ratio is too large. Thus, the stages are 4.3:1, with 3 planet gears, and 2.5:1, with 5 planet gears. The 2.5:1 stage is first to connect to the motor because the input torque to the second stage is lower than if reversed. If the larger gear ratio was connected to the motor, then greater forces would be transmitted into the second stage, increasing size and subsequently weight compared to the chosen design.

Factors of safety for each stage are based on the smallest gear by comparing allowable stresses to calculated stresses. Factors such as overloading, dynamic and quality of gear are included such that an expected factor of safety of 5.2 for the 4.3:1 stage and 5.8 for the 2.5:1 stage are considered safe for operation. The operational envelope includes RPM variations to assist with flight control, requiring a higher factor of safety than normal to account for the changing conditions. Detailed information of the gear stages can be found in Table 9.4.

The gear stages are constructed of AISI 9310 carburized steel while the housing is cast RZ5 Magnesium-Zirconium alloy. The gears undergo heat treatment to increase surface hardness while retaining flexibility of the inner metal. Magnesium is chosen over aluminum or steel for the lightweight capability and easy casting. Lubrication of the gears is accomplished with synthetic thixotropic grease based on an aluminum complex. Oils are not needed for the short duration flight, but could be adapted quickly to work with the housing.

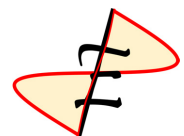


TABLE 9.4: Gear Geometry and Information

Parameter	Stage 1			Stage 2		
	Sun	Planet	Ring	Sun	Planet	Ring
Number of Teeth	120	30	180	60	69	198
Face Width (in)	0.375	0.375	0.375	0.45	0.45	0.45
Pitch Diameter (in)	3	0.75	4.5	1.5	1.725	4.95
Diametral Pitch (teeth/in)	40	40	40	40	40	40
Total Gear Ratio	2.5:1			4.3:1		

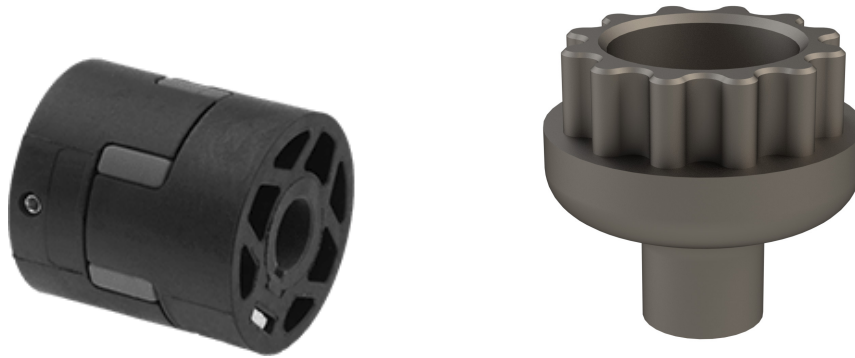


FIGURE 9.8: Flex coupling used to correct potential misalignments in shaft and rotor coupling used to connect flex coupling to rotor shaft

9.5.2 Flex Coupling and Rotor Coupling

The flex coupling and rotor coupling in Figure 9.8 allow for potential misalignment of the gearbox and rotor while transferring power to the rotor in a safe manner. The flex coupling used is a vibration damping spider coupling rated for safe operation at 7,000 RPM and 319 N-m (2,830 in-lb) of torque. A custom fitting is inserted into the flex coupling which meshes with a spline on the inside of the rotor shaft to transmit torque. The custom part is made of 4340 steel and has an overload torque factor of safety of 2.

10 Avionics

10.1 Overview

There are three main areas considered in the avionics design: the nacelle, the pilot interface, and the main flight computer. Requirements for these three key areas will be described in the next several sections. Figure 10.1 shows these three areas located on *Elico*.

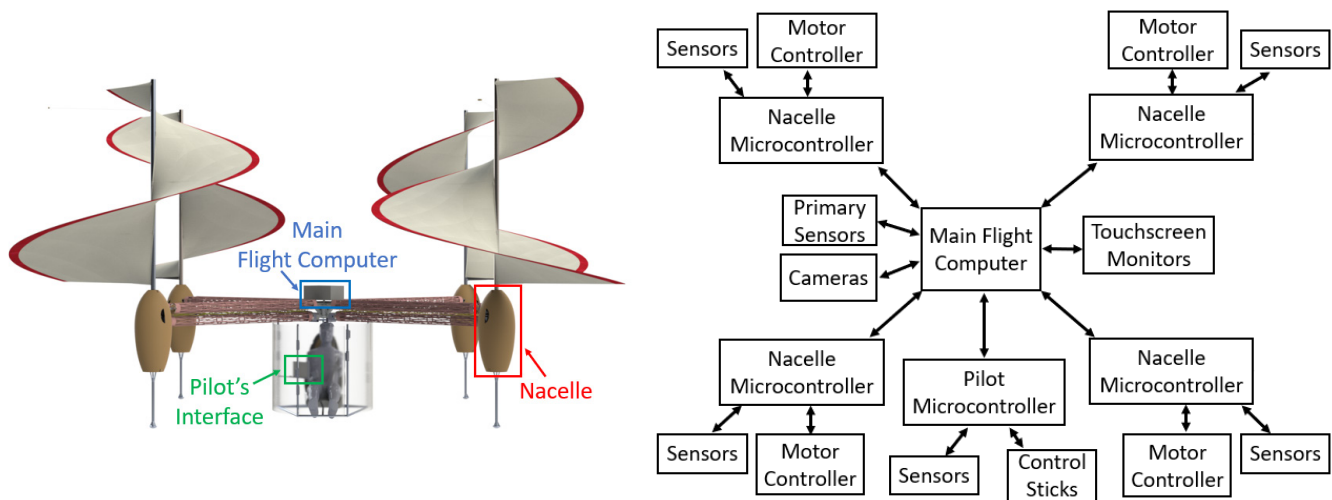


FIGURE 10.1: *Elico*'s avionics development areas and hub and spoke overview

The three areas of development are:

- Nacelle - contains the battery, motor controller, and motor. Main design concern is monitoring the performance of the propulsion and drivetrain systems.
- Pilot's interface - displays *Elico* status to the pilot and records pilot's inputs.
- Main Flight Computer - ensures safe operation of the *Elico* by reading in sensor data, fusing state estimate, computing control laws, and distributing tasks to other subsystems.

A hub and spoke design was selected as the network connection scheme over a daisy chain approach as the nacelles were located 7.8 ft (2.3 m) from the center of the vehicle. This large physical distance necessitated having compact avionics for the nacelles, in order to keep the number of wires to a minimum.

10.2 Nacelle Avionics

The design of the electronic management system started with the nacelle requirements, as this had already identified a battery, motor, and motor controller. In preparation for the avionics design, the types of sensors used on commercial quadcopters (such as GPS, IMUs, LIDARs) were examined to see how *Elico* could incorporate these sensors into the design. The primary purpose of the nacelle's avionics are to monitor the performance of the motor, motor controller, and battery. To accomplish this, DC voltage, DC current, RPM of the aerial screw, and motor temperature are monitored.

Due to the unique design of the aerial screw, safety was of paramount importance when designing the avionics for all components of the vehicle. To accommodate potential structural failures in testing, an IMU is placed at the center of the nacelle to monitor the vibration levels of the nacelle. If a component of the aerial screw suffers damage that degrades the performance of *Elico*, this problem will manifest as excessive vibrations. These excessive vibrations will be recorded by the IMU mounted on the nacelle, and if levels exceed safe operating limits, the nacelle's microcontroller will send a high priority message to the main flight computer.

TABLE 10.1: Modules used to monitor the nacelle's performance.

Module	Communication Type	Description
Hercules Microcontroller	UART, I2C, SPI, USB, Serial	Monitors and control's nacelle's avionics
IMU	I2C	Monitors nacelle's vibration levels
Battery DC Voltage	Analog	Infers battery's state of charge
Battery DC Current	Analog	Infers battery's workload
Motor Temperature	Analog	Monitors motor's working state
LIDAR	I2C	Record's nacelle's height above the ground

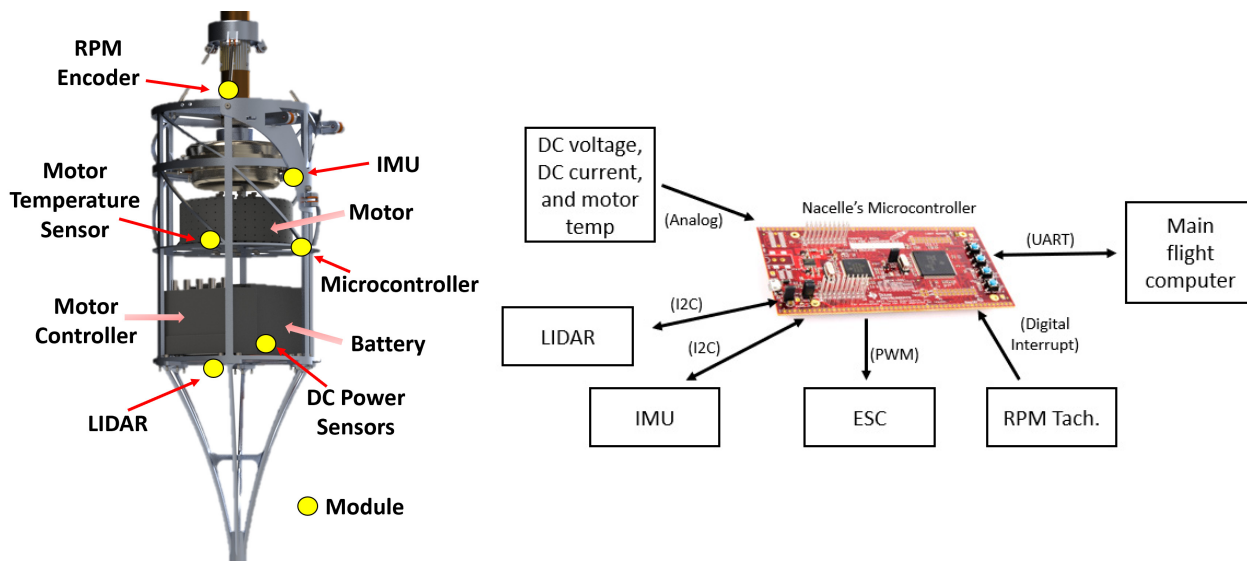


FIGURE 10.2: Nacelle module placement and connection scheme

The microcontroller for the nacelle is responsible for recording the state of the different sensors, contains a closed loop controller to regulate aerial screw RPM, and communicates messages with the main flight computer. Microcontroller selection will be discussed in section 10.2.1.

10.2.1 Selection of *Elico's* Microcontrollers

Based on the predicted workload of the nacelle and pilot's avionics, it was clear that the microcontroller would serve as a safety critical device on *Elico*. As such, once the notional requirements for the microcontroller were identified, a market survey of existing microcontrollers began to determine which module would be used. In addition to satisfying the avionics duties, important features in a microcontroller were ease of development, space weight and power, number and type of input/output channels, cost, and amount of product support. As *Elico* will be developed by university students, it was important to select a microcontroller that had low code development costs. One such type of microcontroller, Arduino, stood out as it is frequently the microcontroller of choice among university research groups. However, it was decided that such a device did not meet the safety requirements for manned aircraft operations, and a suitable, safety-critical replacement for the Arduino was sought after.

Two such microcontrollers were identified as potential replacements: the PLC Arduino ARDBOX and the Texas Instruments Hercules.



Texas Instruments RM46L852 Hercules	
Remarks	Launchpoint Series
Safety Specs	Dual Lockstep
Clock Speed, Flash Memory	220 MHz, 64 kB
I2C, UART, SPI Ports	2, 2, 2
IO Pins	40
Mass	35 grams

FIGURE 10.3: Texas Instruments Hercules and list of specifications

After comparing the two boards against one another, the Hercules microcontroller was selected for use on board *Elicio*. Although the PLC Arduino ARDBOX offered the ability to develop code in the Arduino integrated developer environment (IDE), it was found to be inferior to the Hercules due to the dramatic weight differences between the boards; 350 grams vs 35 grams. Additionally, for manned operations safety is of paramount importance. The Texas Instrument's Hercules excels in this department as it has a dual lockstep redundancy feature to ensure error free operation. The Hercules featured a lower mass, higher number of input/output (IO) pins, and UART connections. Furthermore, the lack of Universal Asynchronous Receiver/Transmitter (UART) connections for the PLC Arduino ARDBOX disqualifies it from consideration. UART is required for the *Elicio*, as the quadcopter's arms are 2.3 m (7.8 ft) and the other communication protocols considered, an Inter-Integrated Circuit (I2C) and a Serial Peripheral Interface (SPI), are intended for use below 2 m (6 ft), whereas UART can be used at lengths of up to 10 m.

10.3 Pilot Interface Avionics

Before designing the pilot's avionics, a review of existing helicopter cockpits was undertaken to identify common design features of modern aircraft. From this research, it was determined that the pilot's interface must be able to record the pilot's inputs and pass these to the main flight computer so that corresponding action can be taken. Additionally, the pilot's interface must display relevant information to the pilot, using screens, indicators, and lights. Actions from the pilot are passed to the main flight computer via a touchscreen monitor that is mounted in the cockpit. This touchscreen monitor will be used to plan autonomous missions for *Elicio* and to abort the missions if the pilot or safety staff deem it necessary.

TABLE 10.2: Pilot interface modules.

Module	Communication Type	Description
Hercules Microcontroller	UART, I2C, SPI	Monitors pilot's inputs
Touchscreen monitors	USB, HDMI	Displays <i>Elico's</i> state to pilot
Pedal Angle	Analog	Records state of auxiliary control sticks
Buttons, knobs, switches	Digital Interrupt	Cockpit switches that the pilot interacts with
Cockpit Lights	Digital	Health and warning indicators

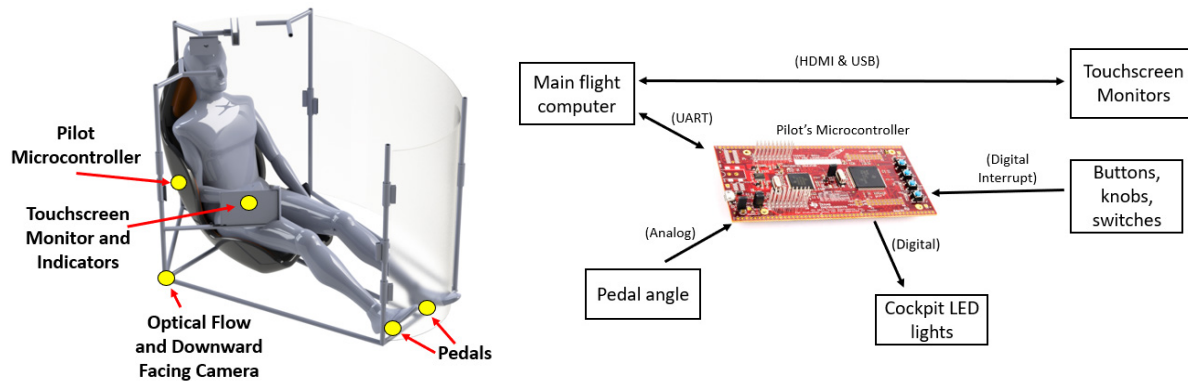


FIGURE 10.4: Pilot interface module placement and connection scheme

Just like the nacelle avionics, the pilot's avionics use a microcontroller to monitor the pilot's actions and to relay key information between the main flight computer and the pilot's indicators.

Unique to the pilot's avionics is the usage of touchscreen displays to show critical information to the pilot. A graphical user interface (GUI) allows information on *Elico* to be displayed to the pilot in a clear and concise manner. However, it dramatically increases the computational requirements on the main flight computer. Additionally, the use of touchscreen displays in embedded control applications has gained popularity in recent years, as the price of onboard computing has plummeted over the last several years. The outputs of the multi-function display and the pilot interface are discussed in Chapter 13

Due to the significant amount of computational resources that are required to generate and update GUIs for the pilot, the microcontroller will not be able to perform these duties. Instead, the role of managing several GUIs is left to the main flight computer.

10.4 Main Flight Computer

The main flight computer is at the center of the hub and spoke avionics design for *Elico*, shown in Figure 10.1. The discussion on how the main flight computer was selected is the subject of section 10.4.1, this section outlines the roles and responsibilities that such a computer would have.

Primary functions for the main flight computer are guidance, navigation, control, communications, and safety of *Elico*. All microcontrollers in the hub and spoke model report their actions to the main flight computer, where the information is parsed and interpreted. Notionally, the main flight computer reads

in the information from the main sensors of the aircraft (the IMU, GPS, cameras, etc) and fuses a state estimate of the vehicle. All components surrounding the main flight computer are located in a central avionics housing that has vibration absorbing padding. The central avionics housing is mounted at a 45 degree angle, shown in Figure 10.5, as it provides better attachment and accessibility points with the central truss structure.

TABLE 10.3: Modules for the main flight computer

Module	Communication Type	Description
NVIDIA AGX Xavier	UART, I2C, SPI, USB, Serial	Main Flight Computer
Cameras	CSI	Situational awareness
GPS	Serial	Provides positional information
Optical Flow Sensor	I2C	Provides velocity information
Compass	I2C	Provides heading information
Radio	Serial	Communicates with ground station
Main IMU	I2C	Provides attitude information

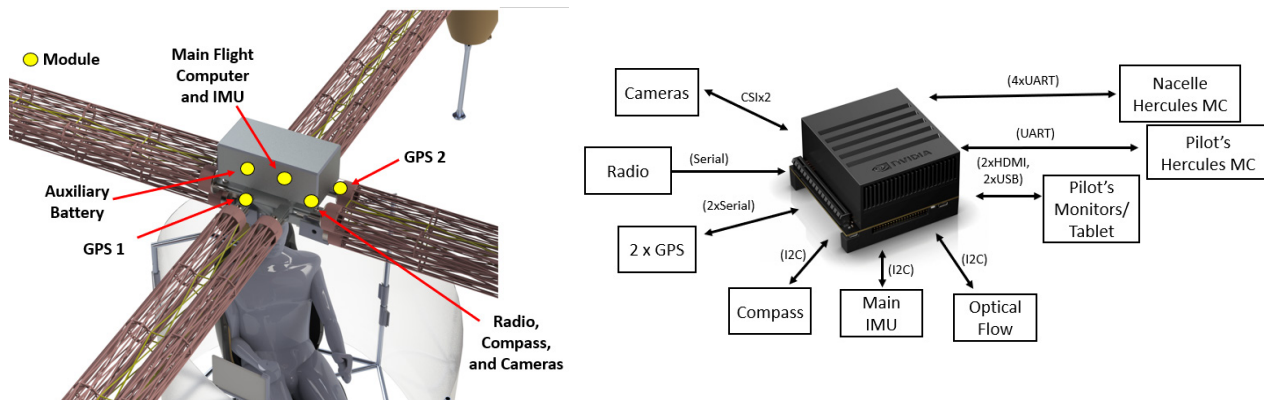


FIGURE 10.5: Main flight computer module placement and connection scheme

10.4.1 Selection of *Elico's* Main Flight Computer

The main flight computer underwent a similar market review of commercially available platforms as the microcontroller. The requirements for the flight computer were outlined in the previous sections, and indicate that driving requirements for the main flight computer are that it must have 5 UART connections and be able to generate a GUI for several touchscreen monitors. For enhanced pilot safety, a real time operating system (RTOS) shall be required to properly ensure that all flight instructions are executed in a time-critical manner. Similar to the microcontroller selection process, the software development with main flight computer needed to user friendly as it is intended for use primarily with University of Maryland students. Two main flight computers were examined: the NVIDIA Xavier AGX and the Qualcomm Flight Pro.

The NVIDIA Xavier was selected over the Qualcomm Flight Pro due to the Xavier's large amount of processing power, which was needed to handle the multiple cameras and generating GUIs for the



NVIDIA AGX Xavier	
Remarks	11 TFLOP/s
Architecture	8-Core ARM 64-Bit, 512 GPU cores
Usage	Computer vision based robotics
RTOS	RedHawk Linux
IO Pins	40+
Mass	670 grams

FIGURE 10.6: NVIDIA AGX Xavier and list of specifications

pilot. Although the Qualcomm Flight Pro was also capable of performing computer vision processing of several cameras, it lacked the functionality to generate the pilot's GUIs, which would have required an additional graphics device. The resulting Qualcomm Flight Pro and graphics card system was deemed unnecessarily complicated, as the NVIDIA AGX Xavier could singlehandedly perform all of these functions. To ensure safe operation, the NVIDIA Xavier will use RedHawk Linux, as this is an RTOS developed specifically for the Xavier. Overall, the distinguishing feature about the NVIDIA Xavier is its extensive use in computer vision applications.

10.5 Computer Vision

To facilitate autonomous forward flight, a down facing camera, GPS module, IMU and altitude sensor are required on the vehicle in addition to an onboard processor.

Individually, GPS information is subject to availability and while accurate and robust against drift, is imprecise at small distances and velocities. An INS (inertial navigation system) utilizing IMU data is precise and accurate at small distances and velocities, but poor against drift and vibrations. An altimeter informed optic flow method is accurate at large velocities and low altitudes, but suffers from noise and drift. Because *Elicio* operates at low altitude and requires precise position information with no drift for safe landing, none of these options are suitable on their own.

However, by implementing an extended Kalman filter on the output of GPS, INS, and optic flow systems, the strengths of one system compensate for the weaknesses of another. At *Elicio's* flight conditions a system utilizing a combination of optic flow, INS, and GPS can achieve a root-means-squared position estimate accuracy of less than 0.1 m [14].

To facilitate an accurate autonomous landing an AprilTag tracking system is used via the down facing camera. An example of an AprilTag can be seen in Figure 10.7. By implementing a computer vision AprilTag detection algorithm and utilizing the Perspective-n-Point (PnP) algorithm the precise location and orientation of the AprilTag can be found relative to the camera with an accuracy of 0.01 m (0.033 ft) depending on visual conditions. By placing a known AprilTag as the landing marker and utilizing knowledge on the camera orientation from the vehicle IMU, the position of the vehicle relative to the landing marker is determined. This information is used to inform the positional controller described in Chapter 12 to execute a landing sequence. This allows *Elicio* to land autonomously and precisely on a designated point, improving ease of use and broadening applications.



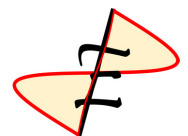
FIGURE 10.7: Example of an AprilTag

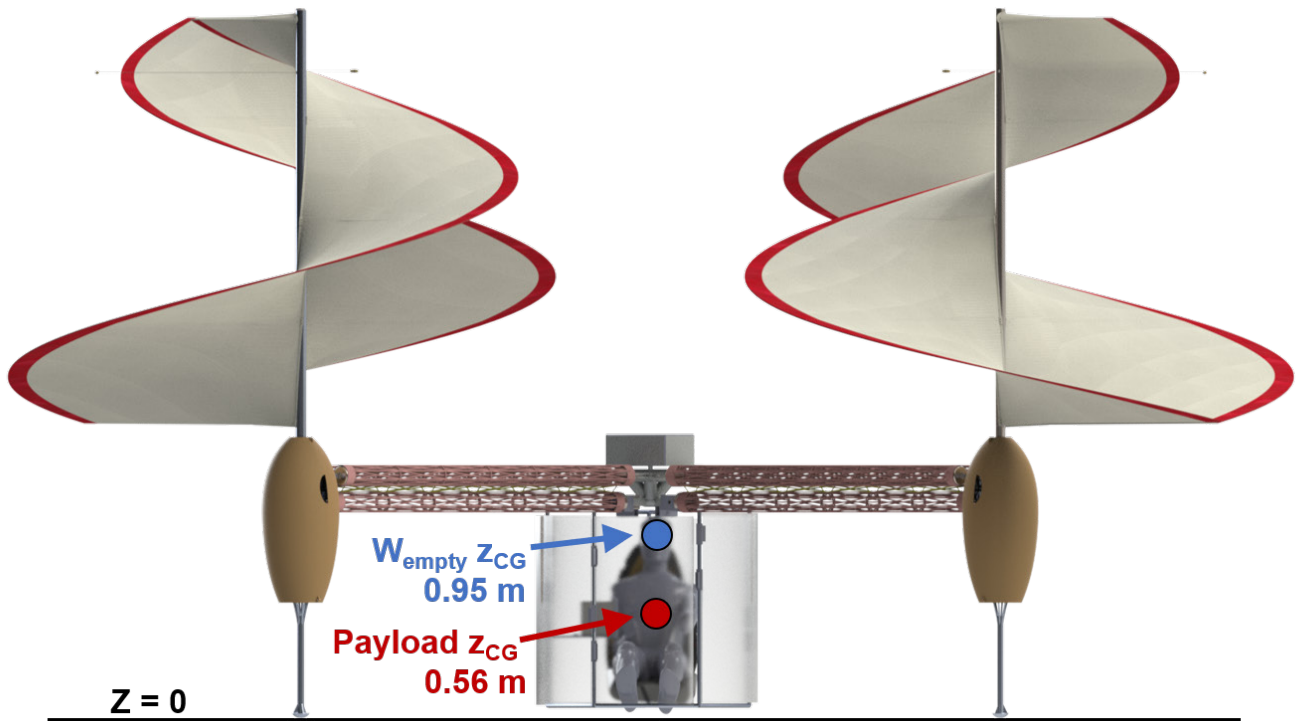
11 Weight Analysis

Table 11.1 details the weights and center of gravity (CG) location for each component of the aircraft. The CG in the x and y directions are symmetrical so are not shown. The origin of the z -axis ($z = 0$) is set to be the ground, with the z -axis positive up. Figure 11.1 shows the z_{CG} locations of the empty weight and the payload on *Elico*.

TABLE 11.1: Weight breakdown and CG analysis for components of *Elico*

Component	Weight			z_{cg}	
	kg	lb	$\%_{empty}$	m	ft
Rotor Group (all rotors)	11.2	24.6	6.49	1.91	6.26
Shaft	4.89	10.8	2.84	1.96	6.43
Spars	1.49	3.28	0.87	1.59	5.21
Skin	1.41	3.10	0.82	1.89	6.21
Attachments	2.93	6.45	1.70	1.86	6.10
Counter-Balance	0.45	0.99	0.26	2.78	9.11
Airframe Group	84.9	187.3	49.4	0.88	2.89
Fuselage	19.6	43.2	11.4	0.56	1.83
Arms	27.2	60.0	15.8	1.03	3.38
Nacelle	29.0	63.9	5.3	0.91	2.98
Attachments	9.12	20.1	16.9	1.03	3.38
Landing Gear Group	2.35	5.18	1.37	0.51	1.66
Propulsion Group	66.7	147	38.8	0.91	3.00
Motors	28.0	61.7	10.9	1.00	3.29
Batteries	18.8	41.4	16.3	0.78	2.58
ESCs	3.80	8.34	2.2	0.78	2.58
Gearboxes	16.1	35.5	9.4	1.07	3.54
Avionics Group	6.88	15.2	4.0	0.56	1.83
Empty Weight	172.03	379.3	100	0.95	3.12
Payload	60	132.3		0.56	1.83
Gross Weight	232.03	511.6		0.76	2.48

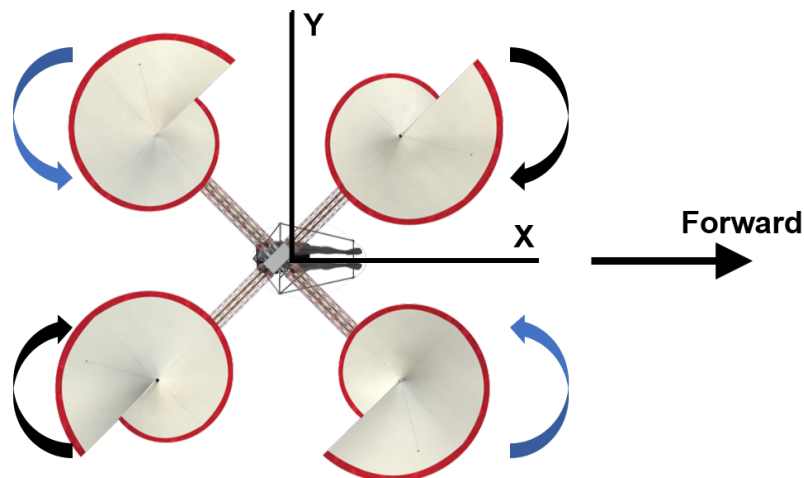


FIGURE 11.1: *Elicó's* empty weight and payload z_{CG} locations

12 Flight Mechanics

12.1 Control System Design

The rotor configuration is designed not only to produce thrust but also to provide anti-torque and control moments. As seen in Figure 12.1, two rotors rotate clockwise (black arrows) while two rotors rotate counter-clockwise (blue arrows), providing the necessary anti-torque.

FIGURE 12.1: Rotation directions of *Elicó's* motors

Elico has a unique design that can be controlled by a conventional quadcopter control system, due to the thrust sensitivity to RPM discussed in Chapter 3. Variable RPM is used to change the vehicle's thrust and torque and therefore changing the trajectory. Using data inputs from the instruments and sensors described in Chapter 10, *Elico* is able to be controlled autonomously, therefore significantly decreasing the pilot's workload. The control system architecture for autonomous flight can be seen in Figure 12.2. The inner feedback loop dictates attitude control, while the outer feedback loop controls the aircraft position and trajectory. The rotors' RPM is controlled through electronic speed controllers that vary individual rotor RPM to change the attitude and position of the aircraft.

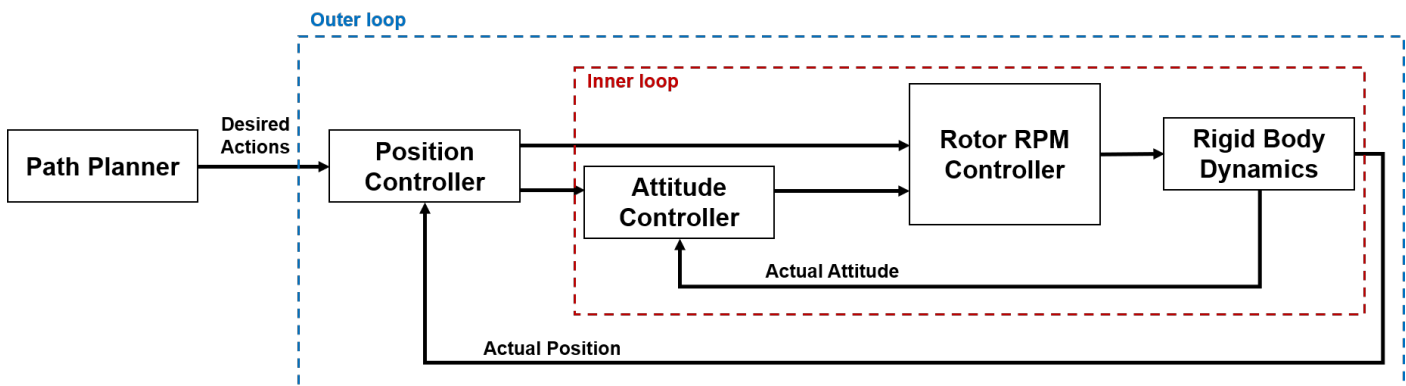


FIGURE 12.2: Control system block diagram

12.2 Maneuverability & Pilot Workload

The control system is designed such that given certain waypoints (inputted by the pilot), the aircraft is able to follow a flight path by connecting these waypoints from takeoff to landing. By setting waypoints corresponding to the RFP mission, shown again in Figure 12.3, the flight path for *Elico* can be determined.

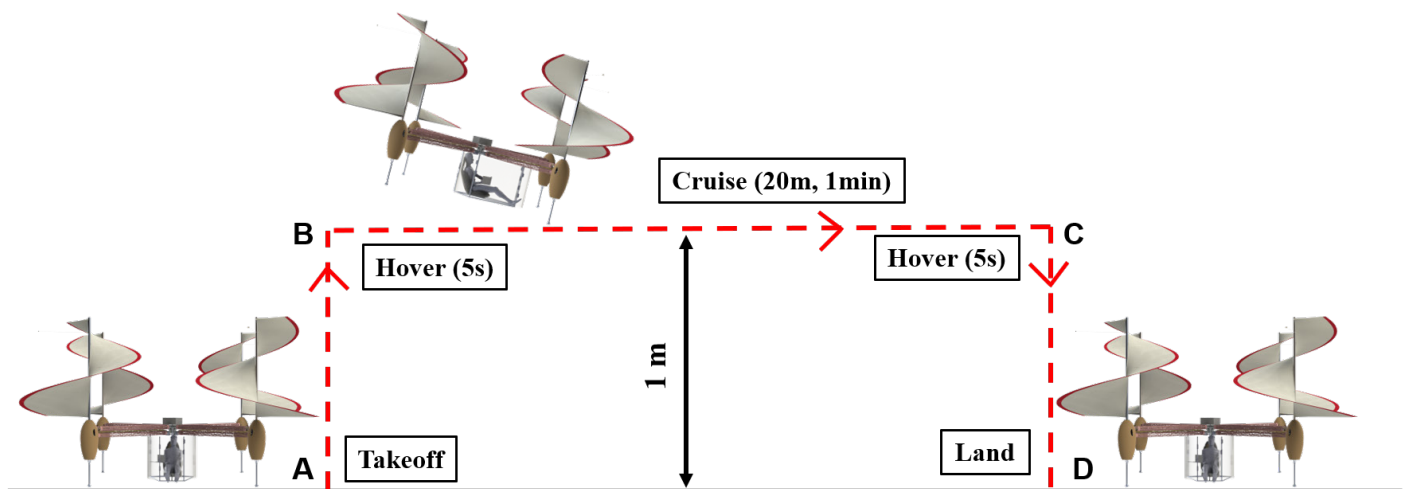
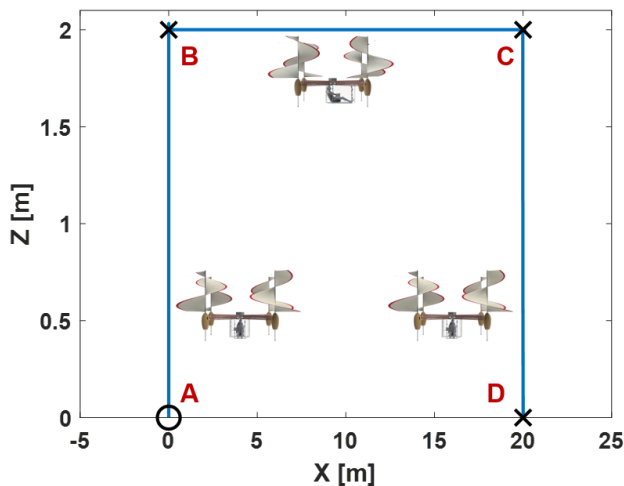
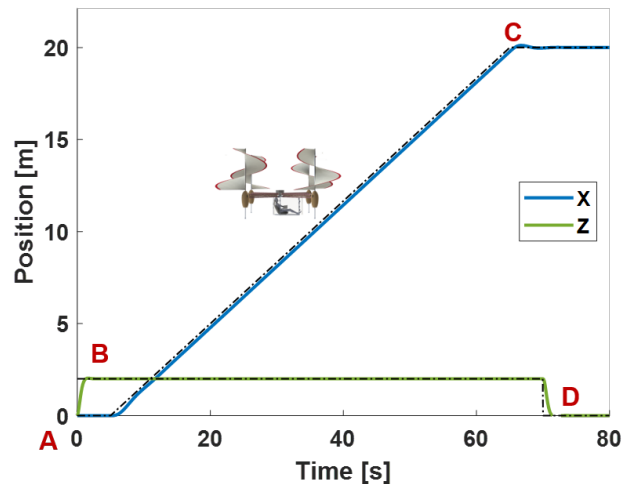


FIGURE 12.3: Mission specified by the RFP, with flight path (A → B → C → D)

Figure 12.4 shows the waypoints ('X') and resulting flight path (solid line), with the aircraft beginning at point A (0,0), performing a vertical takeoff to 2.0 m (point B), flying forward 20 m (point C), and then landing (point D). These points correspond with the required mission waypoints shown in Figure 12.3. The actual altitude of 2.0 m is greater than the RFP requirement, as this altitude ensures the aircraft is out of ground effect while in hover and forward flight. Figure 12.4 shows that *Elico* is able to use the designed variable RPM control strategy to autonomously fly the desired flight path.

The aircraft control system recognizes waypoints based on GPS coordinates, and an AprilTag tracking system is implemented to aid in landing, as described in Section section:compvis. Figure 12.5 shows the response time, or how quickly the aircraft reaches the set waypoints. The desired positions are shown as dotted lines, and the X and Z positions are the solid blue and green lines, respectively. The waypoints shown correspond with those shown in Figure 12.4. The aircraft does overshoot the target of 20 m by approximately 0.5 m (1.6 ft) yet corrects itself within 3.0 seconds. This overshoot is within the maximum radius of 10 m from the landing spot, as specified by the RFP.

FIGURE 12.4: Path of *Elico*FIGURE 12.5: X and Z Position of *Elico* vs time elapsed

Elico is designed for minimal pilot workload, with a fully autonomous flight control system. The pilot must set the waypoints using the provided tablet, and then the control system flies on the designated flight path. The autonomy requires little effort from the pilot.

13 Pilot Accommodations and Interface

Elico's cockpit is designed for the flight experience as Leonardo dreamed of it. The sleek, simple design seen in Figure 13.1 is built around an intuitive interface for minimal pilot workload. The aircraft will be off the ground with the touch of a button! The multi-function display(MFD) is retrofitted for a left or right handed person. There are five Plexiglas panels that completely surround the pilot, providing protection from wind and debris, as well as allowing a virtually unobstructed view during flight. The cockpit frame is composed of round aluminum tubing that is welded together with five main support beams. The frame is connected to the arms and central structure of the vehicle utilizing a threaded bracket connecting to the titanium alloy pins of the central structure. The frame is securely fastened to

the central structure by steel bolts that pass through the bracket, arms of the vehicle and the titanium alloy pins.

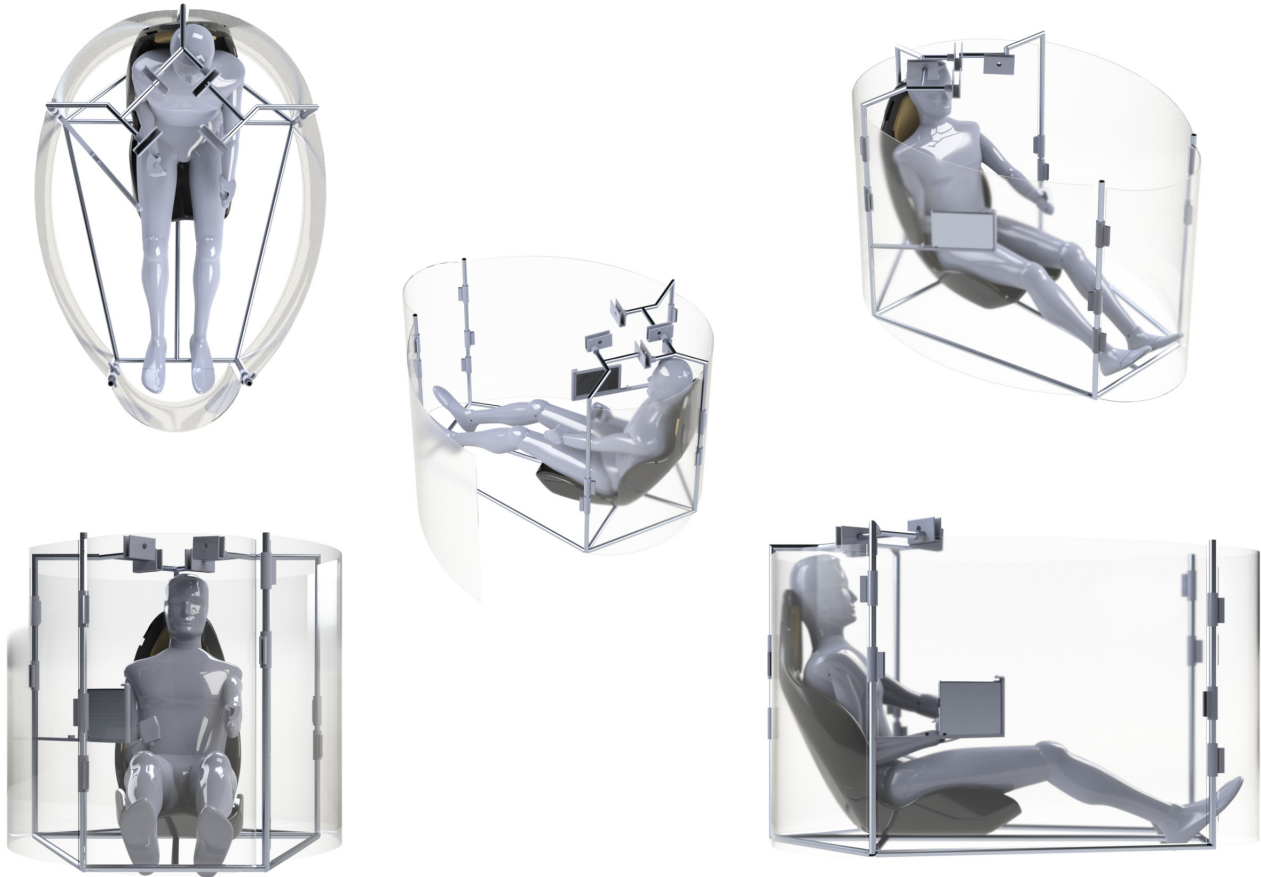


FIGURE 13.1: Pilot cockpit arrangement

13.1 Multi-Function Display

The MFD features two displays, shown in Figures 13.2 and Figure 13.3, for the pilot to input commands and monitor vehicle state. The first display is the start up window where the pilot interacts and sets destination waypoints, which then appear on the map. The second display contains digital readings of typical aircraft indicators as well as pertinent in-flight information. The display will show the information for all four rotors including: RPM, battery voltage and current, and temperature at the bottom of the screen. A compass, vehicle attitude and GPS information are shown on the left-hand side of the screen, while the map is on the right-hand side. There is also an emergency “Abort” button which immediately lands the vehicle at the nearest safe landing spot as an added pilot safety measure.

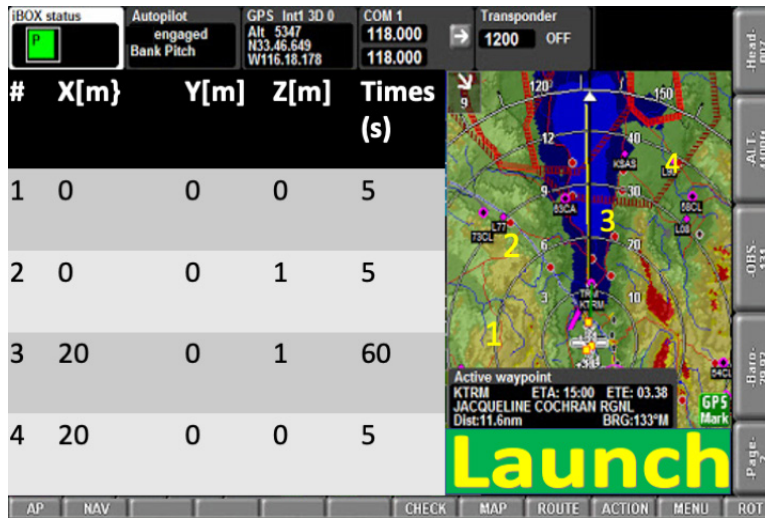


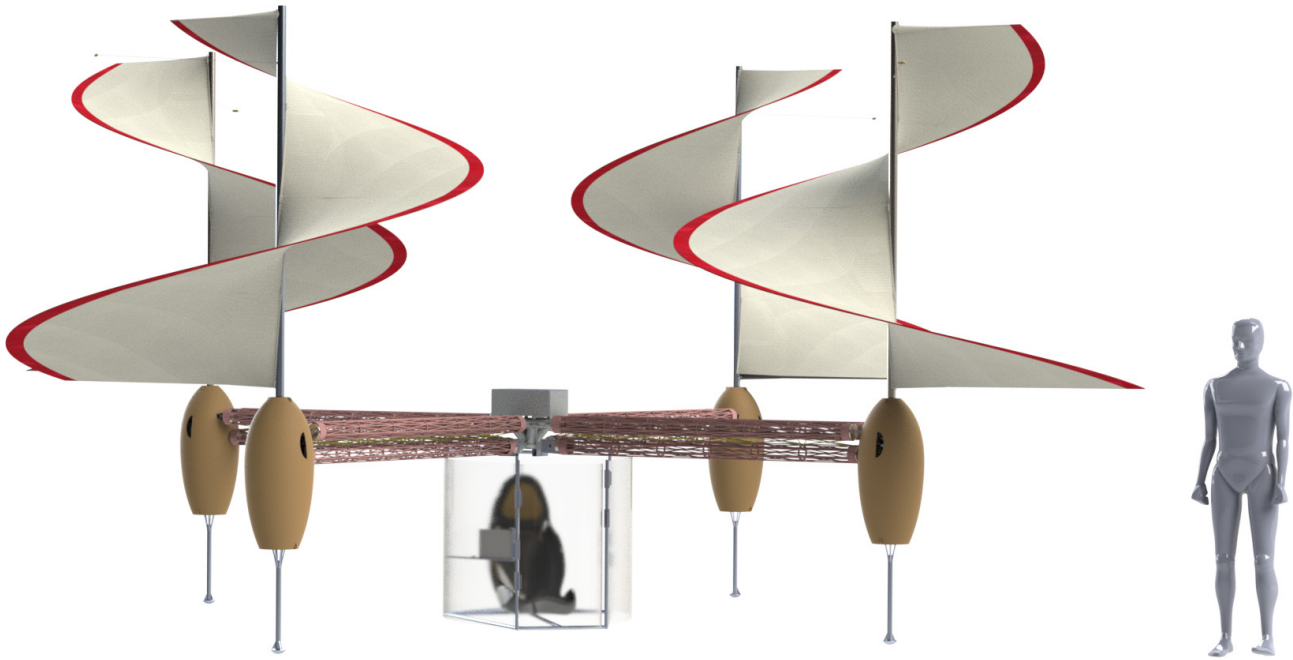
FIGURE 13.2: Multi-function tablet display for initial start up



FIGURE 13.3: Multi-function tablet display for in flight vehicle information

13.2 *Elico* Flight Experience

As seen in Figure 13.4, the pilot will enter on the left side of the vehicle using the plexiglas door. The pilot climbs in and sits comfortably in the bucket seat, puts on their seat belt, and rests their legs on the foot rest. The pilot then interacts with the MFD inputting waypoints of desired destinations, which appear on the map. Once the pilot is satisfied with their selection, they push the bright green launch button. The vehicle starts up and begins to travel to the waypoints that were programmed before takeoff. While in flight, pilot responsibilities are at a minimum as *Elico's* flight computer guides the rotorcraft to its destination. After a successful flight *Elico* lands safely on the ground for the pilot to exit the vehicle. Should an emergency landing be required, the pilot can abort flight at any time. *Elico* immediately identifies the nearest safe landing spot for the pilot and lands itself for safe pilot exit.

FIGURE 13.4: Pilot and *Elicopter*

14 Interactional Aerodynamics and Acoustics

While the Computational Fluid Dynamics (CFD) simulations of the aerial screws estimate the air loads and flow fields, these quantities are ideal in the sense that the testing is performed on an isolated rotor. *Elicopter* has a quadrotor configuration where the rotors operate close to each other and close to the ground, and thereby the actual flow fields of each rotor are influenced by the other rotors and ground. The effect of this aerodynamic interaction was studied for *Elicopter's* rotors using CFD.

14.1 Interaction Between the Rotors

Performing a CFD analysis for the interactions of the quadrotor configuration requires modeling all four rotors, and requires more computational effort compared to an isolated rotor. Furthermore, since the RPM of the rotors is a control variable, the rotors may operate asynchronously. An accurate model to study these interactions should ensure provisions for taking all these variables into account. However, to primarily understand the extent of the impact of the interaction between the rotors, an approximate model, as shown in Figure 14.1, was simulated. This model uses the method of images by imposing inviscid wall boundary conditions and assuming the rotors operate synchronously and in a similar environment.

The inflow pattern for the aerial screw can be seen from the streamlines in Figure 14.2. The thrust and power coefficients reduce by about 20% and 5% respectively in Table 14.1 as compared to the isolated aerial screw. This is because the overall inflow to the rotor coming from all directions in the isolated case is now shared partially with the other interacting rotors. Furthermore, due to the tapered geometry, the thrust and torques now have additional harmonic components, since the relative closest separation between the adjacent rotors is oscillatory. These differences from the isolated rotor are accounted for during *Elicopter's* sizing by adjusting the rotor parameters based on these results.

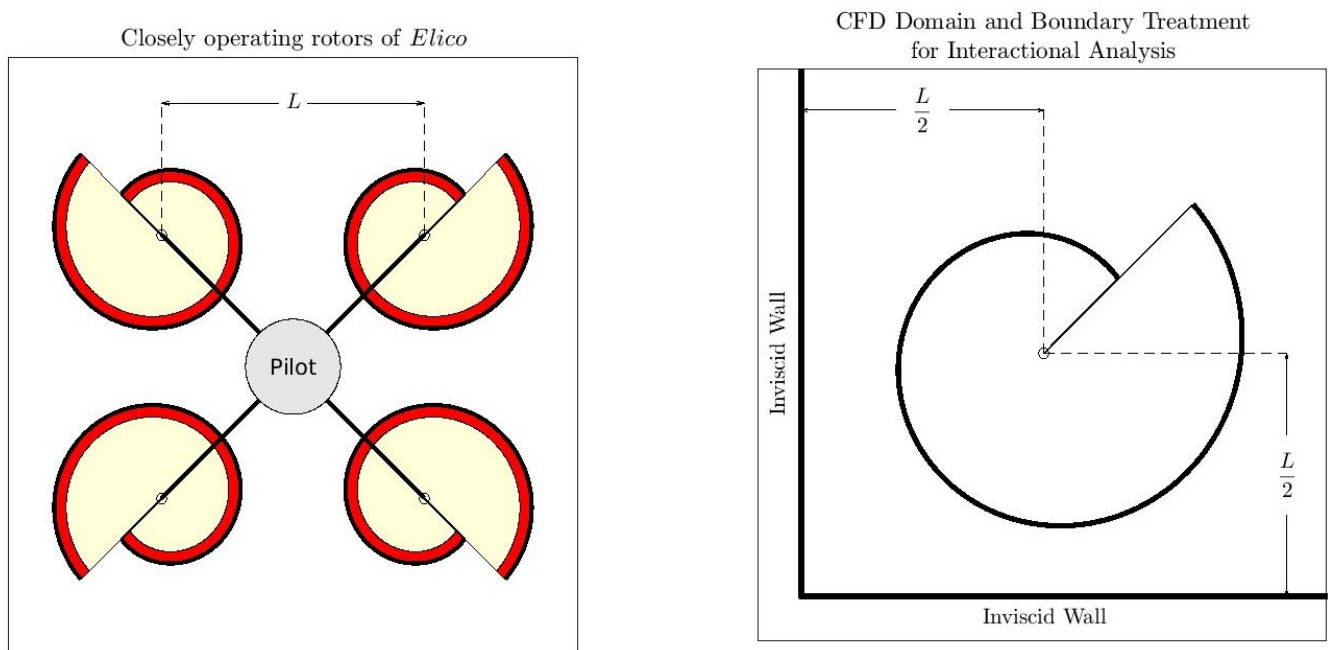


FIGURE 14.1: CFD model for investigating the interaction between the rotors of *Elco*

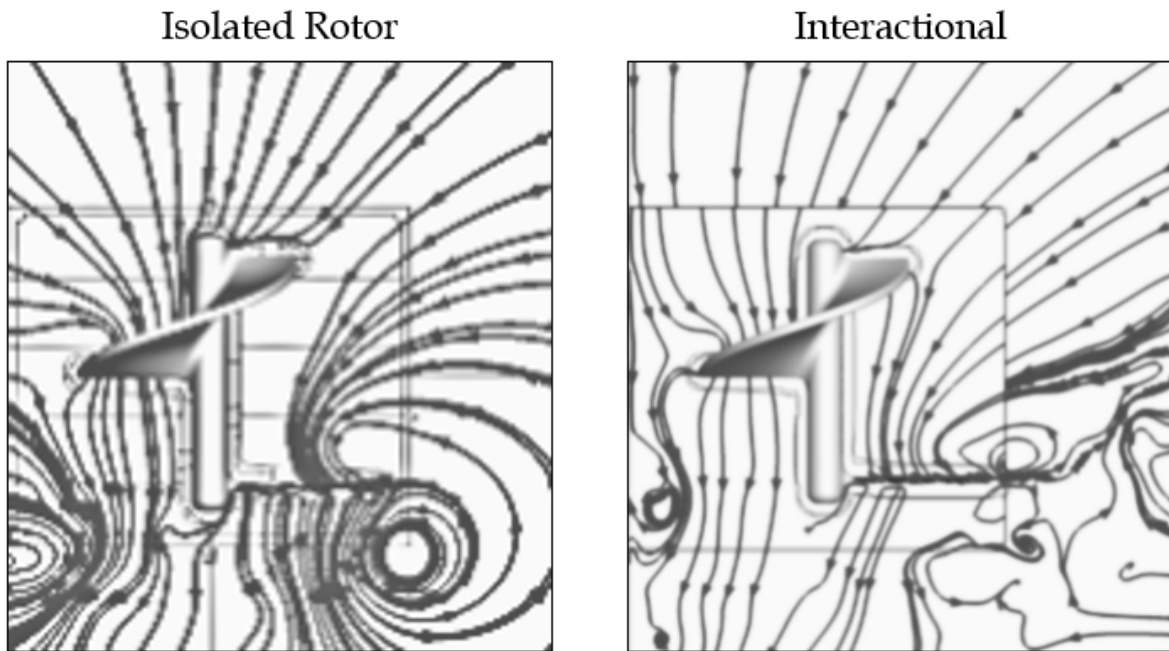


FIGURE 14.2: Streamlines of the flow around the rotors

14.2 Ground Effect

Elicó is designed for an operating mission close to the ground. CFD analysis is used to understand the effect of the ground plane on the performance and aerodynamics of *Elicó*. Similar to the testing of interaction between the rotors, this analysis assumes synchronous rotors operating in a similar environment. Additionally, the effect of ground plane is simulated using an inviscid wall boundary. Contrary to a typical helicopter rotor, the aerial screw performance is barely affected by the presence of the ground plane. Table 14.1 shows the *Elicó*'s estimates of rotor aerodynamic parameters for each interactional model.

TABLE 14.1: Performance estimates of the aerial screw with interactional aerodynamic models

Aerodynamic Coefficient	Isolated Rotor	<i>Elicó</i> (out of ground effect)	<i>Elicó</i> (in ground effect)
Thrust Coefficient (C_T)	0.027	0.023	0.024
Power Coefficient (C_P)	0.0075	0.0072	0.0071
Figure of Merit (FM)	0.416	0.343	0.365

14.3 Acoustics

The interactional aerodynamics results obtained were used to analyze the noise levels of the rotors of *Elicó*. For this, the University of Maryland's in-house acoustic analysis solver ACUM, based on Ffowcs-Williams-Hawkins equations and using Farassat formulation 1A [15, 16], was modified to incorporate the interactional models developed for *Elicó*. The thickness noise (resulting due to the displacement of air by aerial screw rotation) and the loading noise (due to aerodynamic loadings on the aerial screw) are estimated using the solver.

The noise level on a hemisphere at a distance of $6R$ from the center of the vehicle was estimated. Figure 14.3 shows the noise level estimates due to a single aerial screw located on the top right. The maximum sound pressure level assuming a constructive interference and synchronous rotors is found to be less than 90 dB.

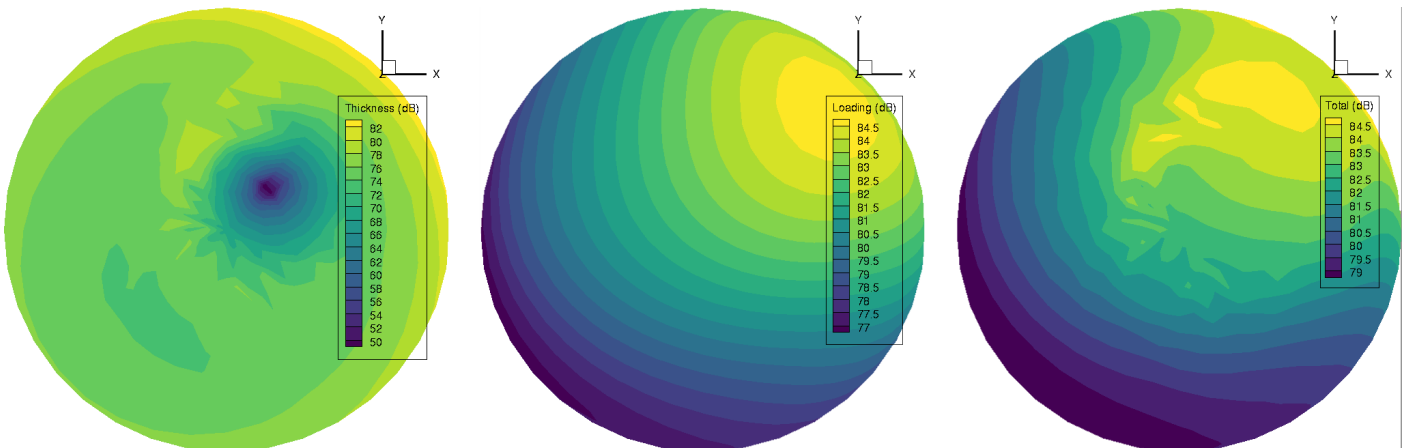


FIGURE 14.3: Sound pressure level split up at $6R$ from the vehicle

15 Cost

As a technology demonstrator, *Elico* is one of a kind. As such, providing a cost estimate must begin at the component level in a bottom up approach. Development of *Elico* will start with the construction of an experimental demonstrator. The majority of *Elico*'s structure can be fabricated using low-skill labor and commercial off-the-shelf (COTS) products. The cost is broken down by component group based on existing products and uses a conservative estimate of man hours required for fabrication. In anticipation of potential issues in first-time manufacturing, initial cost estimates include an assumption of 25% spares for all structural components.

Construction of the rotor requires interior machining of the rotor shaft, fabrication of 5 individual carbon fiber spars and helical supports, machining of spar attachments, and sewing and attaching the skin to the rotor. At a rate of \$100/hr for machining and \$60/hr for assembly, the cost is estimated to be \$13,500 per rotor plus an additional \$6500 in one time costs for molds and tooling.

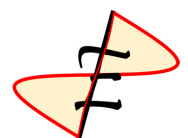
The nacelle structure manufacturing includes the landing leg and main body, both made of aluminum and the fiberglass fairing. The estimated cost is \$920 per nacelle. Each arm requires at least 200 man hours for fabrication, and this cost is added to the material requirements.

Battery cost is based on the rubberized battery used in Section 9.1.

In all, the cost of materials and manufacturing labor for *Elico* is **\$ 200,374**.

TABLE 15.1: Cost breakdown for *Elico*

Component	Cost (per quantity)	Quantity (including spares)
Rotor Group	\$13,500	5
Airframe Group		
Cockpit	\$1,393	1
Arms	\$12,625	5
Nacelle	\$920	5
Propulsion Group		
Motor	\$1,464	4
Batteries	\$8,200	4
ESC	\$450	4
Gearboxes	\$2,200	4
Avionics Group	\$14,500	1
Fabrication Cost	\$200,374	



16 Performance and Capabilities

Elicó is designed to exceed the RFP requirements, with preliminary sizing for more than double the specified flight time. To evaluate the vehicle performance, the drag in forward flight is estimated, the effect of center of gravity (CG) variation on rotor speed is analyzed, the effect of altitude on hover performance is determined, and the maximum range and payload are shown for *Elicó*.

16.1 Drag Estimation

A vehicle drag estimate must be determined for an accurate calculation of *Elicó*'s forward flight performance. Using the wetted area S of the vehicle and the drag coefficient, calculated to be $C_{d0} = 0.036$, the flat plate area F can be estimated. This is a conservative estimate as the true flat plate area typically is between the vehicle's frontal area and the wetted area. Furthermore, an additional 20% was added to the calculated flat plate area to account for parasitic drag that is difficult to estimate, such as drag from installed cameras and sensors.

Additionally, the flat plate factor k can be estimated from Harris's formula found in [17], where $GTOW$ is the gross takeoff weight in pounds:

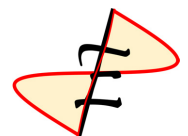
$$F = S \cdot C_{d0} = k \left(\frac{GTOW}{1000} \right)^{2/3}$$

This results in a flat plate factor $k = 8.18$. For conventional helicopters this factor is approximately 2.5, and for quadcopters it is approximately 4.95. The flat plate factor for *Elicó* is larger than conventional values as the rotors are 1.9 m (6.3 ft) tall, and is a conservative estimate using the entire wetted area of the vehicle.

16.2 Effect of Center of Gravity on Rotor Speed

A CG shift on a quadcopter requires the rotors to vary the rotor speed to accommodate the new CG moment. When the CG moves towards the front rotors, there is a nose-down moment and the front rotors must rotate at a higher speed to generate the same amount of power, while the opposite is true of the back rotors. Figure 16.1 shows how the CG shifting towards the front rotors by varying radius (R) percentage requires an increase in front rotors' speed, shown by 'o', and a decrease in the back rotors' speed, shown by '◇'. Note that the back rotors with a 1.0R CG shift (yellow points) lie under the point for the 1.1R CG shift (purple points), both at zero power.

When the CG moves towards the back rotors, there is a nose-up moment and the back rotors must rotate at a higher speed to generate the same amount of power, while the opposite is true of the front rotors. Figure 16.2 shows how the CG shifting towards the back rotors by varying radius (R) percentage requires an increase in back rotors' speed, shown by 'o', and a decrease in the front rotors' speed, shown by '◇'. Note that the front rotors with a 1.0R CG shift (yellow points) lie under the point for the 1.1R CG shift (purple points), both at zero power. The maximum CG shift in either direction is 1.1R, or 1.6 m (5.3 ft).



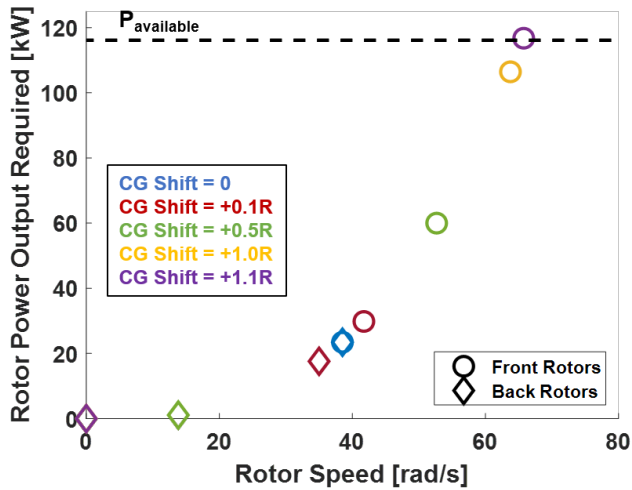


FIGURE 16.1: Effect of forward CG shift on front and back rotor speeds and power outputs

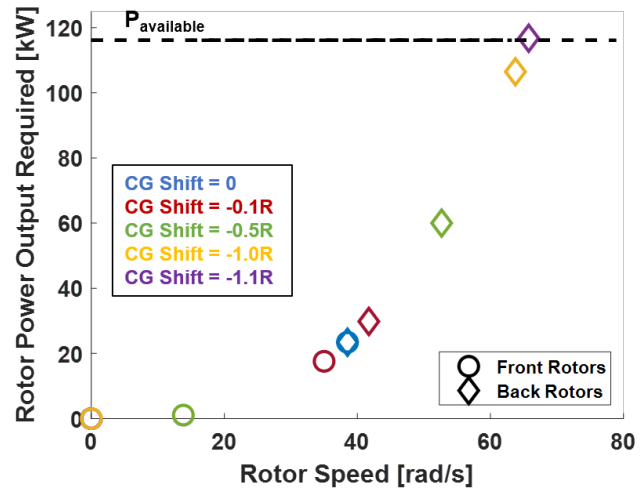


FIGURE 16.2: Effect of backwards CG shift on front and back rotor speeds and power outputs

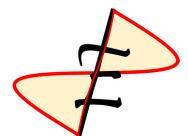
16.3 Performance at Various Altitudes

The mission specified by the RFP requires a flight altitude of at least 1.0 m (3.3 ft). For *Elico* a height of 2.0 m (6.6 ft) was set to ensure that flight occurs out of ground effect. However, *Elico*'s flight may occur at a higher elevation and consequently require more power. To show that *Elico* has the required installed power to fly at extreme elevations, the hover power required out of ground effect (HOGE) was calculated for *Elico* flying in 15°C (59°F) at College Park, Maryland and at Denver, Colorado. Since the available power is 101 kW (135 hp), Table 16.1 shows that there is sufficient power available and *Elico* is able to fly at these altitudes.

TABLE 16.1: Power required for *Elico* to hover out of ground effect in College Park, MD and in Denver, CO

	College Park, MD		Denver, CO	
	Metric	Imperial	Metric	Imperial
Elevation above MSL	2.0 m	6.6 ft	1,609 m	5,280 ft
ρ_{air}	1.224 kg/m ³	0.0024 slugs/ft ³	1.047 kg/m ³	0.00203 slugs/ft ³
P_{req}, HOGE	38.3 kW	51.4 hp	41.4 kW	55.6 hp

Any excess hover power can be used to climb vertically. The variation of steady rate of climb in hover with pressure altitude is shown in Figure 16.3, at standard ISA temperature of 15°C (59°F) and in hot conditions of 35°C (95°F). A rate of climb of zero gives the absolute ceiling altitude and would result in *Elico* unable to fly in specified conditions. Figure 16.3 does not show this zero point as the pressure altitude was capped to 8,000 ft (2,438 m) for pilot or passenger safety.



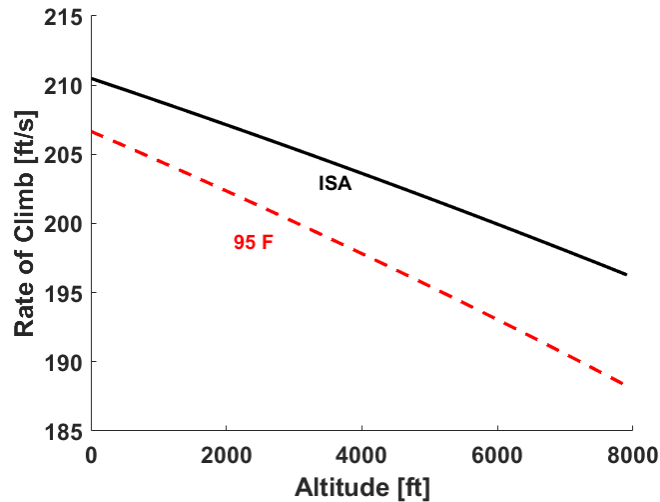


FIGURE 16.3: Rate of climb at various pressure altitudes

16.4 Autorotation

While not a required aspect of *Elico's* design, it is interesting to quantify the autorotation index (AI) for this novel configuration. This will prove useful for the extended missions *Elico* is capable of. For missions taking *Elico* high above the ground, and beyond the dead man zone, it must be able to safely autorotate in case of emergency. To safely autorotate, *Elico's* batteries must supply a small amount of current to overcome drivetrain friction and place the motor into a nominally zero torque state. This allows the aerial screws to rotate freely without drawing any power. The ability for an aircraft to autorotate depends on several factors such as rotor disk loading, stored kinetic energy in the rotor system, and weight of the aircraft. This capability can be quantified using the Autorotation Index, *AI*, which is a measure of its stored kinetic energy. Sikorsky *AI* is defined as:

$$AI = \frac{I_R \Omega^2}{2W \cdot DL}$$

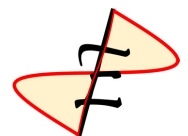
where I_R is the rotational inertia of the rotor, Ω is the rotor speed, W is the weight of the aircraft per rotor, and DL is the rotor disk loading. The relative value of *AI* provides a means for comparing new designs to those of existing aircraft. For single engine helicopters, a value of 20 is considered acceptable while multi-engine helicopters may have a lower index and still operate safely. Taking $W = \frac{1}{4}GTOW = 69$ kg (152 lb), *Elico* has an *AI* of 27 at sea level due to its large rotor inertia and low disk loading. This indicates that in an emergency where autorotation is needed, *Elico* can land and keep the pilot safe.

16.5 Performance Limits

The maximum range in cruise and maximum payload in hover of *Elico* demonstrate how *Elico* has exceeded the RFP requirements.

16.5.1 Maximum Range

With the vehicle *GTOW* and battery specifications, the range of *Elico* can be determined using the battery C-Rate. C-Rate is in units of $[\text{hr}^{-1}]$, so a battery discharging with a certain C-Rate would have a time of flight (TOF) = $1/C\text{-Rate}$. With the designed forward flight speed V of 0.33 m/s (1.08 ft/s),



the following equation can determine the maximum range of *Elicó*.

$$\text{Range} = \text{TOF} \cdot V$$

With a variable battery C-Rate, the time of flight and therefore the range can exceed the required 20 m. Furthermore, if the payload weight is exchanged for a larger battery, the range extends even further as seen in Figure 16.4. Note that the combined payload and battery weight stays constant. At the design point with a 60 kg (132 lb) payload, the maximum range is 74.3 m (244 ft). If the payload was replaced with an additional 60 kg of batteries, the range extends to 311 m (1,020 ft).

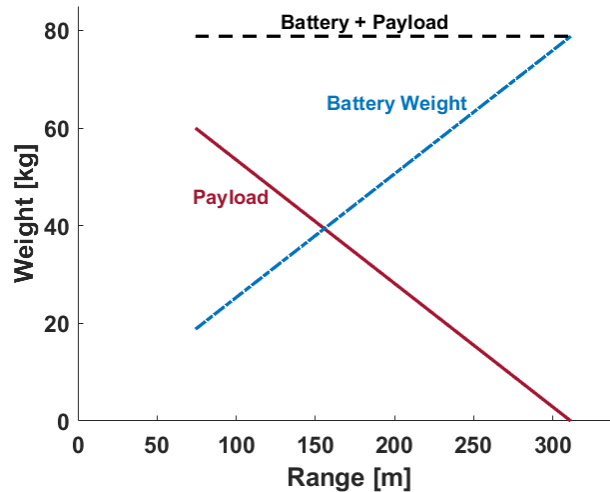


FIGURE 16.4: Effect of decreasing payload and increasing battery weight on maximum range

16.5.2 Maximum Payload in Hover

The power available to *Elicó* exceeds the required hover power of 38 kW (51 hp) by 63 kW (84 hp). This excess available power could potentially be used to carry more payload. With *Elicó*'s empty weight of 172 kg (379 lb), the maximum payload possible for the RFP mission was determined to be 134 kg (295 lb). This is more than double the required payload specified by the RFP and allows *Elicó* to carry cargo or accommodate a wider range of pilots or passengers.

16.5.3 Turbo-Electric Option for Greater Range

For a typical, multi-hour mission, a turbo-electric design offers increased range and endurance compared to an all electric approach, as aircraft fuel is more energy dense than currently available batteries. Since *Elicó* was sized for only 3 minutes of hover, the turbogenerator's ability to use energy dense fuel was not applied. The design study discussed here compares a state-of-the-art turbogenerator and compares it to the MaxAmps battery used on *Elicó* to determine the optimal powerplant design for longer missions. Both technologies were sized to provide DC power and the turbo-electric and battery powered designs were compared.

Turbogenerator Specifications

In late 2019, Honeywell Aerospace unveiled its new, HTS900 turboshaft engine paired with a 200 kW DENSO generator, seen in Figure 16.5, to create a turbogenerator specifically designed for the urban air mobility and electric aviation markets.

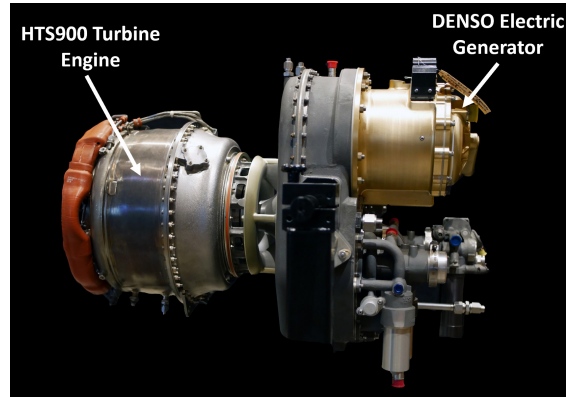


FIGURE 16.5: Honeywell's HTS900 turbogenerator

The Honeywell turbogenerator has a rated max power up to 610 kW, exceeding the required *Elicó* hover power of 38 kW by an order of magnitude. As a result, the Honeywell turbogenerator was rubberized in order to come up with a realistic powerplant mass for the aircraft; the turbogenerator's turbine engine and generator are scaled to the appropriate power setting.

The HTS900 turbogenerator uses a DENSO generator to convert the turboshaft's rotational power into electrical power, which is then used to power the main electrical bus of the aircraft. Included in this DENSO generator is a rectifier system that ensures the generator's AC power is regulated into a constant DC power. The technical specifications of the Honeywell turbogenerator are shown in Table 16.2, which is used to rubberize the turbogenerator to the appropriate power and weight for *Elicó*'s requirements.

TABLE 16.2: Honeywell HTS900 turbogenerator specifications

HTS900 Turboshaft Engine		
Take-off power	610 kW	820 hp
Continuous power	563 kW	757 hp
Weight	153 kg	338 lb
Take-off Power Density	3.99 kW/kg	2.42 hp/lb
Specific Fuel Consumption	0.328 kg/(kW·hr)	0.54 lb/(hp·hr)
DENSO Generator		
Electric Power Output	200 kW	268 hp
Mass	22.7 kg	50 lb
Power Density	8.81 kW/kg	5.36 hp/lb

For a required DC power, P_{req} , the rubberized generator and turboshaft are both sized using the power densities (power available per unit weight) of the DENSO generator and the HTS900 turboshaft, respectively. The fuel consumed over the course of the mission depends on the specific fuel consumption (SFC) rate, the mission TOF, and the power setting. The estimated final weight of the turbogenerator powerplant W_{TG} is the sum of the rubberized generator W_{GEN} , the rubberized turboshaft engine W_{TS} , and the required fuel W_f :

$$W_{TG} = W_{GEN} + W_{TS} + W_f = \frac{P_{req}}{P_{avail,GEN}/W_{GEN}} + \frac{P_{req}}{P_{avail,TS}/W_{TS}} + SFC \cdot P_{req} \cdot TOF$$

The expression for the turbogenerator mass is compared to a similar expression for overall battery mass to study how the mission TOF is critical when choosing between batteries and turbogenerators.

Comparison of Battery and Turbo-Electric Designs

The MaxAmps Li-ion battery used on *Elicoo* was discussed in depth in Section 9.1. To compare the turbogenerator weight to a battery weight, the same P_{req} was used to size the two powerplants. As was stated previously, the turbogenerator topology excels at longer TOFs, whereas batteries result in a lower powerplant weights for shorter TOFs. To determine the TOF at which the weight of the MaxAmps batteries and of the rubberized turbogenerator are equal, called the “crossover TOF,” the masses of each system were set equal to one another.

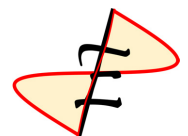
$$m_{TG} = m_{BAT}$$

Using the powerplant characteristics from Table 16.2 and the battery specifications discussed in Figure 9.2, the crossover TOF was found to happen after 4 minutes of flight. The RFP requires a 1.2 minute flight, whereas *Elicoo* was sized for a 3 minute flight. Future iterations of the *Elicoo* with longer missions may use a turbo-electric powerplant.

16.6 Potential Applications for *Elicoo*

Although *Elicoo* was designed for a 70 second flight that was specified in the RPF, this report has identified several areas where *Elicoo* could act as a disruptive technology that has a range of applications. Chapter 14 identified that *Elicoo*'s novel method of producing lift allows the aircraft to fly with a low tip speed and generate lower noise levels than conventional aircraft, which are key traits for an aircraft to successfully operate in an urban environment. Urban air mobility aircraft are designed to operate in short, inter-city commutes in highly populated areas and *Elicoo* could serve as a safe entry level training platform for civilian pilots. *Elicoo* could also be used as a delivery drone in an urban environment.

As a low noise multi-rotor, *Elicoo* could be modified to operate as a quiet, tethered system. New companies are beginning to develop quadcopters equipped with cellular communications hardware to hover above a populated area to provide additional cell coverage during a sporting event or concert. These aircraft are designed to operate above dense population zones at low altitude, where noise produced from the rotors is a driving design constraint. A tethered *Elicoo* could be powered by a ground station so that it can be used as a mobile tethered cell phone tower during high demand events or natural disasters with reduced noise pollution. If *Elicoo* was further upgraded with a turbo-electric generator for increased range, it could be configured as a low-noise autonomous resupply aircraft. *Elicoo*'s quiet aerial screws would enable a VTOL logistics aircraft to physically land in close proximity to the



units without compromising their locations due to excessive aircraft noise.

In its current configuration, *Elico* is best equipped to operate as an educational demonstration and interactive exhibits in museums around the world. The mission specified in the RFP is well suited for this application. With its expanded payload capability and endurance, *Elico* enables anyone the opportunity to experience flight as Leonardo da Vinci envisioned 500 years ago.

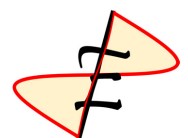


FIGURE 16.6: *Elico* landed in the gardens at the *Museo Nazionale Scienza e Tecnologia Leonardo da Vinci* in Milan, Italy

17 Summary

The University of Maryland Graduate Team has designed *Elico*, an experimental demonstrator, to meet all of the vehicle and operational requirements specified in the Request for Proposal for the 2020 VFS Student Design Competition. *Elico* is a quadrotor vehicle that is designed to highlight the ingenuity of Leonardo da Vinci's concept from over 500 years ago. *Elico* is capable of carrying a 60 kg (132 lb) pilot or passenger over 74 m, or a 134 kg payload for the RFP specified mission of 20 m. *Elico* is able to accomplish this with a maximum gross takeoff weight of 276 kg (609 lb), requires 38 kW (51hp) to hover, and has an overall footprint of 39.5 m² (425 ft²). Autonomous flight ability allows anyone to experience flight in a recreation of history. Through rigorous experimental testing in conjunction with high-fidelity CFD analysis, a physical understanding of how an aerial screw can generate thrust efficiently was developed. Using this knowledge, the designed tapered geometry takes advantage of the initial vortex to generate lift along the entire surface of the screw. The rotor structure is based on Leonardo's original design, with changes to modern materials. In order to balance the large rotor

moments, a light counterbalance greatly reduces the 1/rev loads on the structure. The main vehicle structure is comprised of an ultralight, cellular truss design that maximizes strength to weight ratio. The state of the art avionics and flight control system allows for autonomous takeoff, landing, and path following. Accessibility was a principal design consideration for the pilot, allowing for easy cockpit access, safety, and high visibility. A modular design comprised of easily purchased or manufactured components makes the vehicle attractive to build for commercial enterprises and universities. *Elico* utilizes modern technology to bring a piece of history to life.



Effect of COVID-19

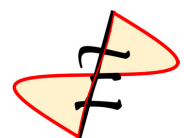
At the time of the submission of this report, the effects of the novel coronavirus, COVID-19, are still being felt around the world. The University of Maryland, College Park campus has been under “severe research restrictions,” meaning no research on campus, since March 21, 2020. Since the Graduate team starts work on the first day of the spring semester, January 27, this allowed for only 7 weeks of on-campus research. It was during this time that all experimental test and analysis of the aerial screw was performed. Once restrictions were put in place, further testing could not be completed. While the work that was able to be completed did show promising results, there is always more research to be done on such a unique model. Had restrictions not been put in place, additional time would have been spent:

- Refining the rotor test stand to reduce signal noise
- Performing larger parameter sweeps of screw pitch and taper
- Speeding up the 3D printing, rapid prototyping of new screw geometries
- Testing new screw geometries including hedral angle and ducted rotors
- Developing physical means to reduce 1/rev vibrations of the rotor for centrifugal and aerodynamic imbalance
- Performing 1/4 scale tests on the final rotor geometry for validation

These tests would have had incredible impact on the rest of the vehicle, most especially the Computational Fluid Dynamics (CFD) simulations run on the aerial screw. Owing to the huge computational requirements for the CFD simulations on the complex airscrew geometries, the test case matrix is designed based on the results of the experimental tests.

Beyond the inability to test, the physical distance of the team forced all communication to be through online sources and meetings held over Zoom. This reduced team efficiency as communication was now more difficult than working in the same space. Additionally, the new format made meeting with professors and advisers and receiving their feedback and mentorship more difficult.

Ultimately, while the UMD Graduate Design Team is proud to present this report in its current state, the restrictions put in place due to COVID-19 prevented a more extensive experimental study of the operation of the aerial screw concept.



Bibliography

- [1] Isaacson, W., *Leonardo da Vinci*, Simon and Schuster, 2017.
- [2] Nicholl, C., *Leonardo Da Vinci: The Flights of the Mind*, Penguin Books Limited, 2005.
- [3] Laurenza, D., *Leonardo's Machines*, Studioddm S.n.c, 8th ed., 2017.
- [4] Leonardo da Vinci, "Paris Manuscript B," 1489.
- [5] Leishman, G. J., *Principles of Helicopter Aerodynamics*, Cambridge University Press, 2006.
- [6] Jung, Y. S., Govindarajan, B., and Baeder, J., "A Hamiltonian-Strand Approach for Aerodynamic Flows Using Overset and Hybrid Meshes," *Annual Forum Proceedings - AHS International*, May 2016.
- [7] Hrishikeshavan, V., *Experimental Investigation of a Shrouded Rotor Micro Air Vehicle in Hover and in Edgewise Gusts*, Ph.D. thesis, University of Maryland, 2011.
- [8] Leonardo Helicopters, "Request for Information: Design Questions," Online; accessed on 14 May 2019.
- [9] Ng, W. and Datta, A., "Hydrogen Fuel Cells and Batteries for Electric-Vertical Takeoff and Landing Aircraft," *Journal of Aircraft*, Vol. 56, No. 5, 2019, pp. 1765–1782.
- [10] Bowen-Davies, B. B. G., Gluesenkamp, K., Schmaus, J., Staruk, W., Weiner, E., , and Woods, B. K., "Design Optimization of Gamera II: A Human Powered Helicopter," *American Heicopter Society 68th Annual Forum, Forth Worth, TX*, May 2012.
- [11] Phillips, J. K., *Isotruss Bicycle Frame Design Using Beam Theory and Shear Flow Analysis*, Master's thesis, Brigham Young University, Department of Civil and Environmental Engineering, Brigham Young University Utah, 2001.
- [12] Woods, B. K., "Ultra-efficient wound composite truss structures," *Composites Part A: Applied Science and Manufacturing*, Vol. 90, June 2016.
- [13] Budynas, N., *Mechanical Engineering Design*, McGraw Hill Education, 2014.
- [14] Ding, W., Wang, J., Han, S., Almagbile, A., Garratt, M., Lambert, A., and Wang, J., "Adding Optical Flow into the GPS/INS Integration for UAV navigation," 01 2009.
- [15] Ffowcs Williams, J. E., Hawkings, D. L., and James, L. M., "Sound Generation by Turbulence and Surfaces in Arbitrary Motion." *Philosophical Transactions of the Royal Society of London. Series A, Mathematical and Physical Sciences*, Vol. 264, No. 1151, 1969, pp. 321–342.
- [16] Farassat, F., "Linear Acoustic Formulas for Calculation of Rotating Blade Noise." *AIAA Journal*, Vol. 19, No. 9, 1981, pp. 1122–1130.
- [17] Harris, F. D., "Introduction to Autogyros, Helicopters, and Other V/STOL Aircraft," Tech. Rep. NASA SP 2011-215959, National Aeornautics and Space Administration, 2012.

